FUSION REACTIONS IN LASER PRODUCED PLASMA

A Dissertation

by

MATTEO BARBARINO

Submitted to the Office of Graduate and Professional Studies of
Texas A&M University
in partial fulfillment of the requirements for the degree of

DOCTOR OF PHILOSOPHY

Chair of Committee,   Robert E. Tribble
Co-Chair of Committee,   Aldo Bonasera
Committee Members,   Che-Ming Ko
                         Sherry J. Yennello
Head of Department,   George R. Welch

December 2015

Major Subject: Physics

ABSTRACT

The investigation of fusion reactions in laser produced plasma has become of great interest since the development of ultra-short pulse lasers technique, which can enable the measurement of not well known fusion cross sections in plasmas and energy production via nuclear fusion reactions on a larger scale. Also, the direct measurement of fusion cross sections at low plasma temperatures might reveal some role for instance of electron screening. For all these reasons, the investigation of ion energy spectra to better understand the nuclear fusion process in a plasma plays a very important role. For a long period of time, however, only light elements such as Deuterium, Tritium, and ^{3}He have been studied for these applications because of the higher efficiency. In particular, the first generation fusion reactors built on Earth were based on the d-t system, in which the 80% of the fusion energy goes into the neutrons. Nevertheless, recent advances in this particular field of physics and the availability of high intensity laser facilities capable of delivering Petawatts of power into small volumes has opened the possibility to fuels based on neutron-less fusion reactions, like for example p-^{11}B. In this fusion reaction, energy is released mainly in charged alpha particles rather than neutrons, which makes easier the actual conversion and final utilization through various methods (i.e., induction or electrostatic effects). Such methods might be also of guidance for experiments where the plasma is highly compressed and heated such as at the National Ignition Facility (NIF) at the Lawrence Livermore National Laboratory (USA), and at the Omega facility at the Laboratory for Laser Energetics (LLE) of the University of Rochester (USA).

DEDICATION

I would like to dedicate this thesis to Luca and Liborio.

You are the two people in my life that I want to make the most proud of me.

ACKNOWLEDGEMENTS

Most importantly, I want to thank my mother and father for having me and my grandmother and grandfather for having them.

TABLE OF CONTENTS

Page

LIST OF TABLES

1. INTRODUCTION

1.1 Reactions

A nuclear reaction is a process in which the interaction of an ion, b, and a nucleus, A, produces another particle, y, and a resulting nucleus X. This can be expressed as [1, 2]

$$b + A \rightarrow y + X, \tag{1.1}$$

or

$$A(b, y)X. \tag{1.2}$$

There are primarily two categories of nuclear processes: scattering (elastic or inelastic) in which the incident particle and emitted particle are the same, and reactions in which incident and emitted particles are different. In like manner, nuclear reactions can be divided in three subcategories: direct reactions, compound nucleus reactions and resonance reactions. A direct reaction is one in which the incident particle traverses the target nucleus so that it does not combine with the nucleus as a whole but interacts only with some individual constituent. In a compound nucleus reaction, the incident particle becomes bound to the nucleus forming a compound nucleus before the reaction continues. The compound nucleus must live for at least several times the time it would take a nucleon to traverse the nucleus. In resonance reactions, the incident particle can become quasi-bound to the nucleus before the reaction proceeds.

1.2 Coulomb Barrier

Reactions involving charged particles are affected by coulombic interactions. The interaction potential between the charged nucleus (atomic number Z_1) and the charged

particle (atomic number Z_2) forms a Coulomb barrier (Figure 1.1) as [1, 2]

$$V_C(r) = \frac{Z_1 Z_2 e^2}{r}.$$ (1.3)

Where e is the electron elementary charge (i.e., e^2=1.44 MeV fm). This potential barrier is always repulsive. However, the potential is dominated by the strong interaction force that occurs at short distance ($r < r_n$), which binds the nucleons together in a nucleus (i.e., attractive nuclear potential). As a matter of fact, fusion can only occur when the protons or heavier reactant nuclei are close enough to overcome the electrostatic repulsion, so that the attractive short range nuclear potential forces them to fuse by a quantum mechanical tunnelling process at low relative energies, below the Coulomb barrier. This also is possible when the nuclei are heated to very high thermonuclear temperatures, so that the kinetic energy of the particles is high enough to make them overcome the electrostatic repulsion and fuse. Tunneling is a dominant process when the center of mass energy of the colliding nuclei is below the Coulomb barrier, see Figure 1.1.
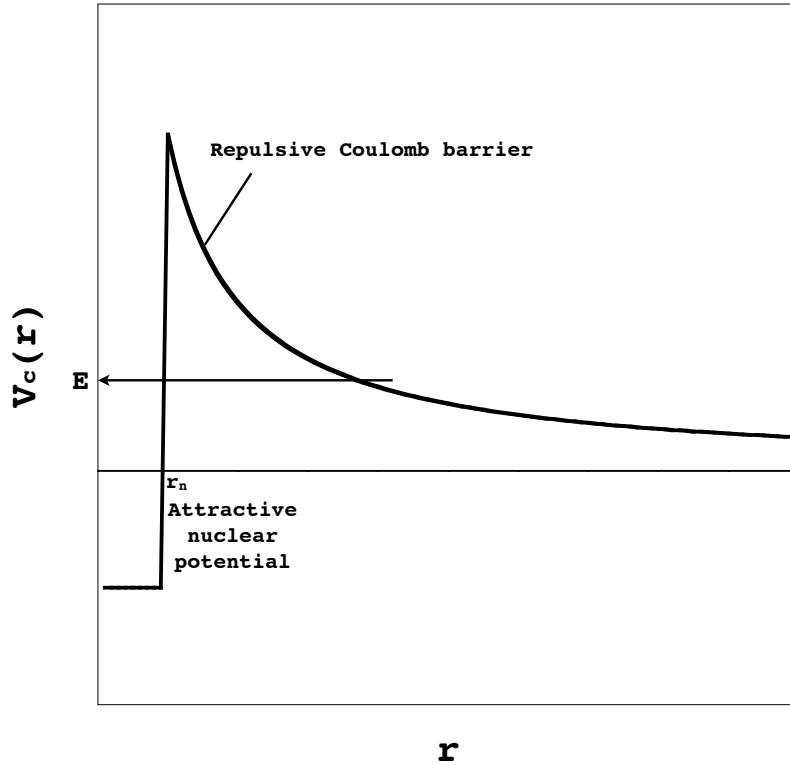
Figure 1.1: Coulomb barrier: the potential is dominated by the attractive short range nuclear potential for $r < r_n$.

1.3 Cross Section and Gamow Peak

As discussed in the previous section, in order for nuclear reaction to occur, particles must overcome the well-known Coulomb potential barrier. The calculation of tunneling probability for charged particles incident upon a nucleus follows the problem of coulombic barrier penetration. The fusion cross section for two interacting particles must therefore be proportional to the probability of tunneling through the potential barrier, and the de Broglie wavelength of the particles. Then, these cross

sections can be written as [2, 3, 4, 5, 6, 7, 8, 9, 10, 11, 12]

$$\sigma(E) = \frac{S(E)}{E} e^{-2\pi\eta(E)}. \tag{1.4}$$

In the above, $S(E)$ is the astrophysical S-factor which takes into account effects of the nuclear force, and the remaining part is the Coulomb barrier penetration probability with $\eta(E) = Z_1 Z_2 \alpha \sqrt{\frac{\mu c^2}{2E_{c.m.}}}$ called the Sommerfeld parameter, Z_1 and Z_2 the atomic numbers of the projectile and the target nucleus, μ is the reduced mass, and $E_{c.m.}$ the center of mass energy; α and c are the fine-structure constant and the speed of light, respectively. Cross section extrapolation is done by introducing the astrophysical S-factor [2, 3, 4, 5, 6, 7, 8, 9, 10, 11, 12]

$$S(E) = \sigma(E) E e^{2\pi\eta(E)}. \tag{1.5}$$

In Figures 1.2-1.3 we plot the S-factors of the nuclear reactions discussed in this work as functions of the center of mass energy [7, 8, 9].

4
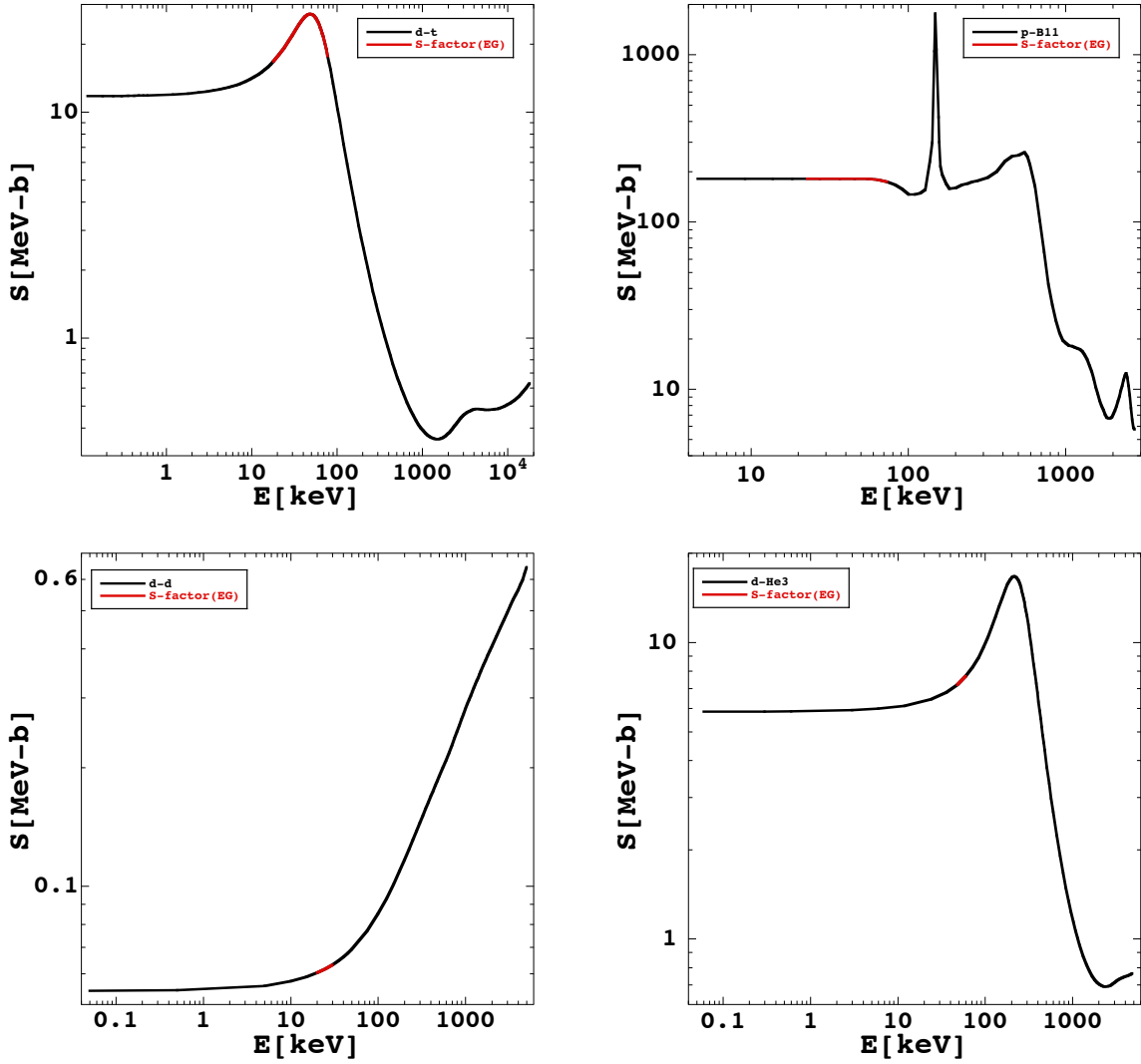
Figure 1.2: S-factors as function of the center of mass energy for nuclear fusion reactions T(d, n)^{4}He (top left), ^{11}B(p,α)^{8}Be (top right), D(d, ^{3}He)n (bottom left), ^{3}He(d, p)^{4}He (bottom right). Data (solid lines) have been retrieved from [7, 8, 9]. The red line represents the S values at the Gamow energies (i.e., the most important fusion reaction energy interval) explored in this work from each fusion reaction experiment analysis.
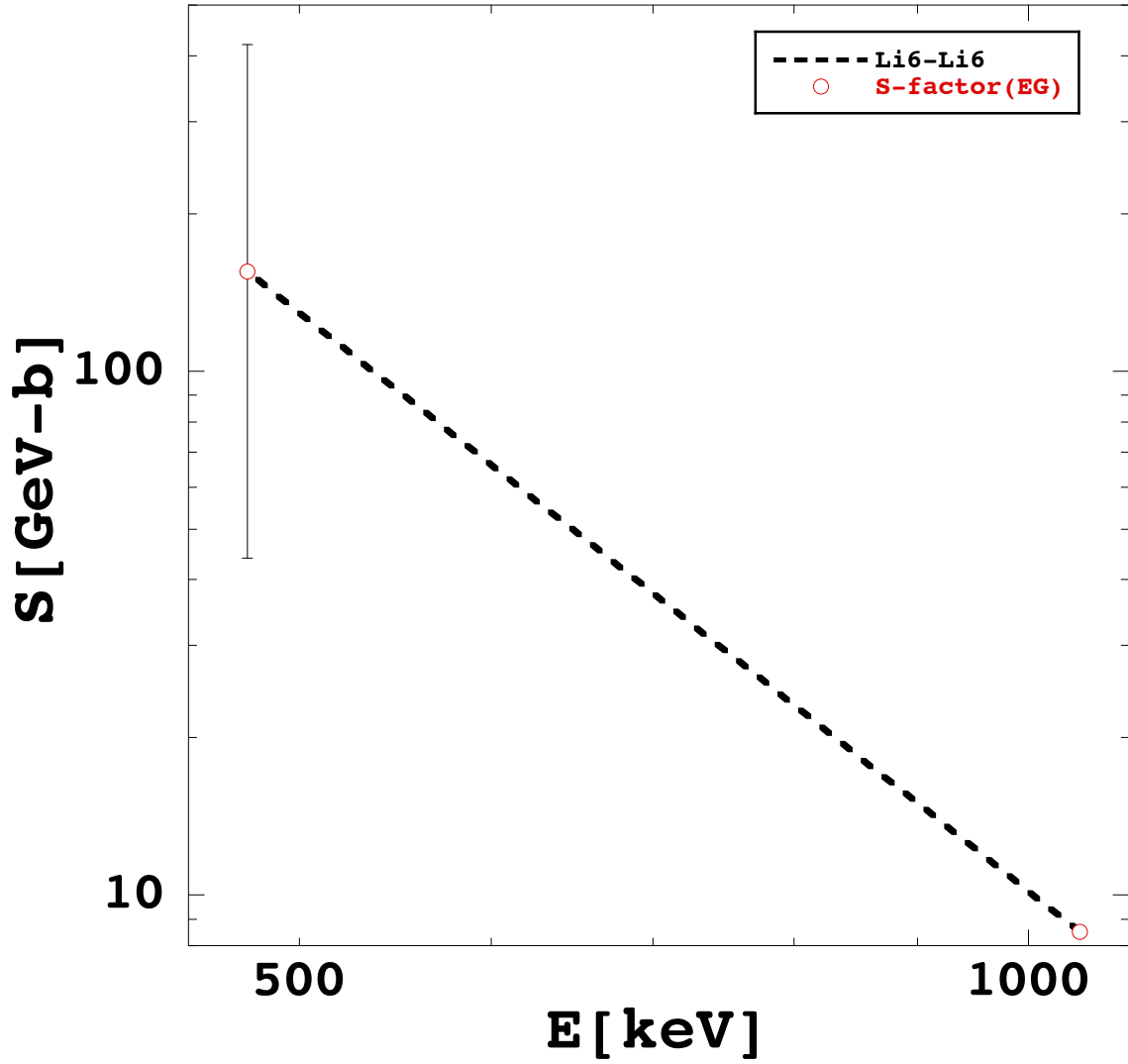
Figure 1.3: *S*-factor for ^{6}Li(^{6}Li,α)^{8}Be nuclear fusion reaction. A value of S=155(-111+266) GeVb has been estimated in our experiments for the ^{6}Li-^{6}Li nuclear reaction at a Gamow energy E_G=476 keV, higher than S=8.5 GeVb obtained in (conventional) beam-targets experiments at 1.05 MeV center of mass energy [7, 8].

In a plasma, the ion kinetic energy distribution is usually described in terms of a Maxwell-Boltzmann distribution at temperature T. Then, given the *S*-factor, one

can write the average cross section as [12]

$$\langle \sigma \rangle = \int_0^\infty \sigma(E) f(E) dE \tag{1.6}$$

Where *f(E)* is the normalized particles distribution function. For a constant *S*-factor and Maxwell-Boltzmann distribution function, the integral can be evaluated with the steepest descent method (see Appendix A) so that one finds [12]

$$\langle \sigma \rangle_T = \frac{4}{\sqrt{3}} \frac{S}{T} e^{-\frac{3E_G}{T}}. \tag{1.7}$$

For non-resonant reactions, E_G is the most effective energy called the Gamow energy peak [13] and corresponds to the maximum of the function integrated in Eq. (1.6) (see Figure 1.4). For Maxwellian distribution function and constant astrophysical *S*-factor one finds $E_G = (\frac{(T\sqrt{b})}{2})^{\frac{2}{3}}$, with $\sqrt{b}=31.42Z_1Z_2 \sqrt{\mu}$ (keV)$^{\frac{1}{2}}$ [12]. These equations show how the chance of tunnelling rapidly increases for small atomic number and mass. As a matter of fact, fusion reactions of interest for energy production on earth only involve the lightest nuclei.
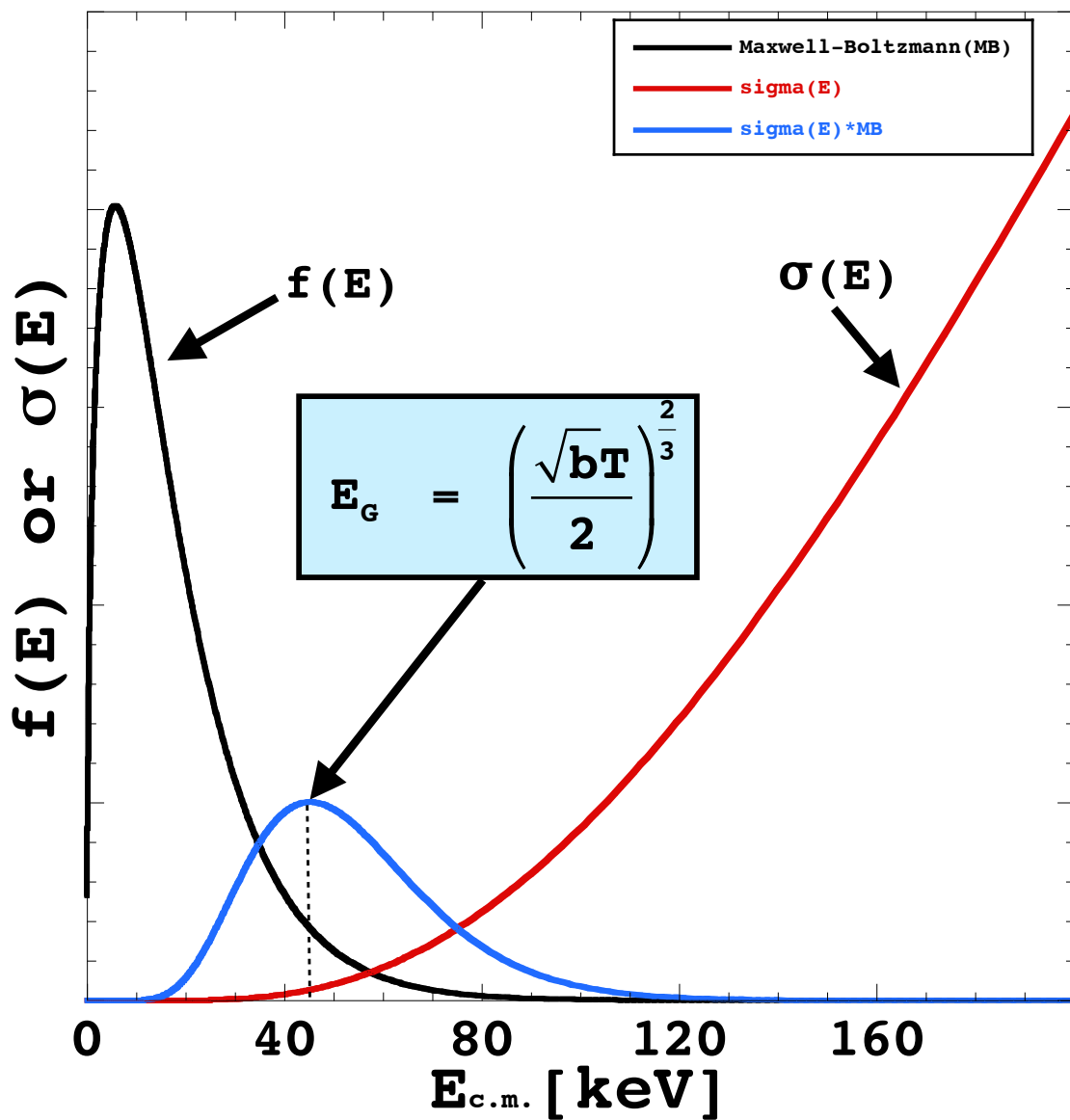
Figure 1.4: The integrand of Eq. (1.6) given by the product of a Maxwell-Boltzmann distribution (black line) with the fusion cross section in Eq. (1.4) (red line). The Gamow peak energy E_G of the reactant contribution is shown (blue line).

1.4   Controlled Fusion

The best example of the fusion reaction process is a burning star. In this gigantic system, the high temperature brings together the light elements by fusing them into heavier compounds with less mass of the fusing elements so that the mass difference Δm is released as energy $E{=}\Delta mc^2$ [14]. Meanwhile, the gravitational energy due to the very large mass of this objects compensates the continuous thermal expansion. In our Sun for example, D and T nuclei fuse to form a helium nucleus and a neutron releasing 17.6 MeV of energy. In order for this process to occur, D+T nuclei must be heated to a temperature of the order of about 100 million °C (i.e., about 10 keV) [15]. The only way to reach such high temperature and density for a sufficiently long time able to produce energy via fusion is to create and to confine a plasma. At the present day on Earth, these conditions can only be achieved through magnetic or inertial confinement. In reactors based on the magnetic confinement fusion approach (ITER project) [16] , plasma is confined in a steady state for long durations, trapping charged plasma particles along a magnetic field and keeping them away from the material wall, so that the hot plasma in the core is separated from the colder plasma near the edge. In the Inertial Confinement Fusion (ICF) approach [17, 18], instead, a spherical hollow shell target containing the fuel is heated by high power lasers at high repetition rate driving the fusion process until temperatures and density required are reached. The largest reactors based on ICF in the world are the National Ignition Facility (NIF) at the Lawrence Livermore National Laboratory, USA, and the Laser Megajoule (LMJ) facility under construction near Bordeaux, France. In this work, we discuss the ICF approach, also called laser-driven fusion reaction.

1.5 Fusion Yield

In laser-driven fusion reactions, the total fusion yield Y produced via laser-plasma reaction can be estimated as [19, 20, 21, 22]

$$Y = \frac{N_1 \rho_2 \langle \sigma v \tau \rangle}{1 + \delta_{12}}. \tag{1.8}$$

Where N_1 is the total number of laser accelerated ions of species 1, ρ_2 is target density of species 2, $\langle \sigma v \rangle$ is the average reactivity, τ is the plasma disassembly time. The value of δ_{12} in the denominator is "0" for the case where the two species of particles are different and "1" for the case where they are the same. In this work, for the experiments discussed here, we will estimate the probability of fusion in the limit where the plasma disassembly time can be estimated as [19, 20, 21]

$$\tau = \frac{p}{v}, \tag{1.9}$$

where p is the plasma length (i.e., average distance traveled by the ions) and v is the speed of the ions. For this reason, the total fusion yield can be rewritten as

$$Y = \frac{N_1 \rho_2 \langle \sigma \rangle p}{1 + \delta_{12}}. \tag{1.10}$$

Of course these set of equations can be used to solve the inverse problem, i.e. given the distribution function from the measurement, one can extract the astrophysical S-factor [23].

For plasmas not in equilibrium, the total fusion yield can also be estimated in two extreme limits of effective temperature and effective energy. In the first extreme limit, assuming that the energy transferred is entirely converted into a temperature $T_{eff} = \frac{2}{3} \frac{\langle E \rangle}{\langle N \rangle} = \frac{2}{3} \langle E_i \rangle$, where $\langle E_i \rangle$ is the average ion kinetic energy. Using Eq. (1.7) we

find that the total fusion yield Y_T is a function of the average cross section of the particles as

$$Y_T = \frac{N_1 \rho_2 \langle \sigma \rangle_T \, p}{1 + \delta_{12}}. \tag{1.11}$$

In the opposite limit, assuming that the energy transferred is entirely converted into collective energy (beam-beam collision) $E_{eff} = \langle E_i \rangle = \frac{3}{2} T_{eff}$, using Eq. (1.4) we find that the cross section corresponds to $\sigma(E_{eff})$ and the total fusion yield Y_C is given by

$$Y_C = \frac{N_1 \rho_2 \sigma(E_{eff}) p}{1 + \delta_{12}}. \tag{1.12}$$

For plasmas not in equilibrium, we expect the number of fusions to be somewhat within these two extreme limits. An alternative route, that we will follow in this thesis is to numerically estimate the average fusion cross section from the experimentally measured ion kinetic energy distribution via Eq. (1.6), rather than making a fit of the data. In fact, the Gamow energy can be identified as well since the measured distribution function rapidly decays to zero for large ion kinetic energies [22, 23]. In such a way, from a good measurement of the ion kinetic energy distribution and of the fusion yield we can derive the S-factor at the Gamow energy assuming that it is constant and without any model assumption by inverting Eq. (1.10), see also Figure 1.3. It is then important to have those measured quantities well under control [23], which is not an easy task as we will show later. However, thanks to the experience acquired here it will be less complicated for future experiments to make measurements with smaller errors.

1.6   Thesis Overview

In this work we discuss fusion reactions experiments via laser-cluster or laser-solid target interaction. The dynamics of nuclear fusion reactions driven by laser are ruled

11

by the Coulomb explosion of laser-heated clusters which have been actively studied both experimentally and theoretically for over a decade [19, 20, 21, 23, 24, 25, 26, 27, 28, 29, 30, 31, 32, 33, 34, 35, 36]. In sections II and III we will discuss, the highly charged clusters of D_2 or CD_4 mixed with ^{3}He gas that promptly explode by Coulomb repulsion under the action of the laser, creating a hot plasma. The resultant deuterium ions are energetic enough to fuse within the cluster jet producing three types of nuclear fusion reactions in the interaction volume: D(d, t)p, D(d, ^{3}He)n and ^{3}He(d, p)^{4}He [20, 21, 22, 30]. We first discuss the possibility that the plasma temperature is directly connected to the cluster sizes. Thus a better control of the sizes can result in a completely controlled plasma temperature which is important for basic science as well as for applications. In fact, one could determine a particular temperature to maximize a given process; for example fusion in d-t clusters near a resonance in the cross section. The plasma density is, however, fixed and it cannot be changed much unless many lasers are used. Besides, since the d-d and d-^{3}He fusion cross sections are very sensible to the temperature accessible in laser-cluster fusion experiments (i.e., 130 keV range) [30, 37], it is very important to determine the plasma temperature accurately. To measure the ion temperature, researchers have often used time of flight (TOF) diagnostics [20, 21, 22, 23, 30, 31, 32], and proved that the temperature measured from the ion TOF data is the same as the plasma temperature at the time of the fusion reactions [20]. In this work, all signals recorded using a Faraday cup detector are transformed and analyzed in energy space [22]. We estimate fusion cross sections at very low energies and estimate the reaction rates for d-d and d-^{3}He nuclear reactions. In sections IV and V, we describe and analyze experiments of laser driven fusion reactions performed at the ABC laser facility in Ente Nazionale Energie Alternative (ENEA) Frascati, at lower intensities (I $\approx 10^{15}$ W/cm^2, 3 ns pulse duration) giving some evidence of the production of fusion α

12

particles [25] in p-^{11}B and ^{6}Li-^{6}Li nuclear reactions. This latter system has never been studied experimentally using lasers. Because of the relatively high Coulomb barrier, the fusion cross section decreases extremely rapidly at low temperatures, and thus it is very sensitive to the highest momentum tail of the plasma distribution. However, thanks to a combination of factors (e.g., Q-value of the reaction, target concentration, non-equilibrium high momentum tail) we will show that the measured number of fusions may be larger than in the p-^{11}B case, opening a different route also to "clean" energy production, i.e. without energetic neutrons produced.

2. LASER-CLUSTERS FUSION EXPERIMENTS

In this section we analyze the process of nuclear fusion reactions driven by laser-cluster interactions in experiments conducted at the Texas Petawatt laser facility using a mixture of $D_2+{}^3He$ and $CD_4+{}^3He$ cluster targets. When clusters explode by Coulomb repulsion, the emission of the energetic ions is "nearly" isotropic. In the framework of cluster Coulomb explosions, in sections 2.1 and 2.2 we describe the experimental setup and particle diagnostic techniques, in section 2.3 we analyze the kinetic energy distributions of the ions using a Maxwell-Boltzmann (MB) distribution, a shifted MB distribution (sMB) and in section 2.4 the energy distribution derived from a log-normal (LN) size distribution of clusters.

2.1   The TPW Facility

The Texas Petawatt laser (TPW) is a 190 J, 170 fs laser based on Optical Parametric Chirped Pulse Amplification followed by power amplification in two types of Neodymium-doped glass [38]. During the experiments, the TPW delivered 90-180 J per pulse with 150-270 fs duration onto a cryo-cooled gas mixture of $D_2+{}^3He$ or $CD_4+{}^3He$ released from the gas jet [39]. The intense laser beam that irradiates the clusters removes the electrons from the atoms and causes the clusters of deuterium ions to explode by Coulomb repulsion [19, 20, 21, 23, 24, 25, 26, 27, 28, 29, 30, 31, 32, 33, 34, 35, 36] creating a hot plasma. Nuclear reaction occurring between the ions within a single cluster is negligible compared with reaction between ions belonging to different clusters. An f/40 focusing mirror (10 m focal length) created a large interaction volume in this experiment with laser intensities sufficiently high to drive laser-cluster fusion reactions. The radius, r, of the cylindrical fusion plasma was estimated from the beam profile measured at the equivalent image plane of the

cluster target. Two cameras imaged the side and bottom of the plasma on each shot. The ratio of the atomic number densities of deuterium and ^{3}He for each shot was calculated from a residual gas analyzer which measured the partial pressures of D_2, CD_4, and ^{3}He in the mixture. The gas mixtures were introduced at a pressure of 52.5 bars into a conical supersonic nozzle with a throat diameter of 790 μm, an exit radius R of 2.5 mm, and a half angle of 5° to generate large clusters (diameter >10 nm) necessary for energetic cluster explosions. D_2+^{3}He and CD_4+^{3}He mixtures were cooled to 86 K and 200-260 K, respectively, to maximize the production of large clusters. Five calibrated plastic scintillation detectors [40] measured the yield of 2.45 MeV neutrons generated from d-d fusion reactions. Three plastic scintillation detectors measured the yield of 14.7 MeV protons from the ^{3}He(d,p)^{4}He fusion reactions. These proton detectors were located in vacuum 1.06-1.20 m from the plasma at 45°, 90°, and 135°. Calibration of the detectors was performed prior to the experiment at the Cyclotron Institute, Texas A&M University, using 14.7 MeV proton beams delivered by the K150 Cyclotron. A 1.10 mm thick aluminum degrader was inserted in front of each detector to block all the other charged particles including the 3 MeV protons originating from d-d fusion reactions, and to slow the 14.7 MeV protons to 4 MeV so that they could transfer all of their remaining kinetic energy to the scintillator disk. When proton detectors operated with 25μm thick aluminum degraders, they also detected the 3 MeV protons from d-d fusion reactions, but the degraders still completely blocked 1.01 MeV tritium and 0.82 MeV ^{3}He ions as well as the deuterium ions coming from the plasma.
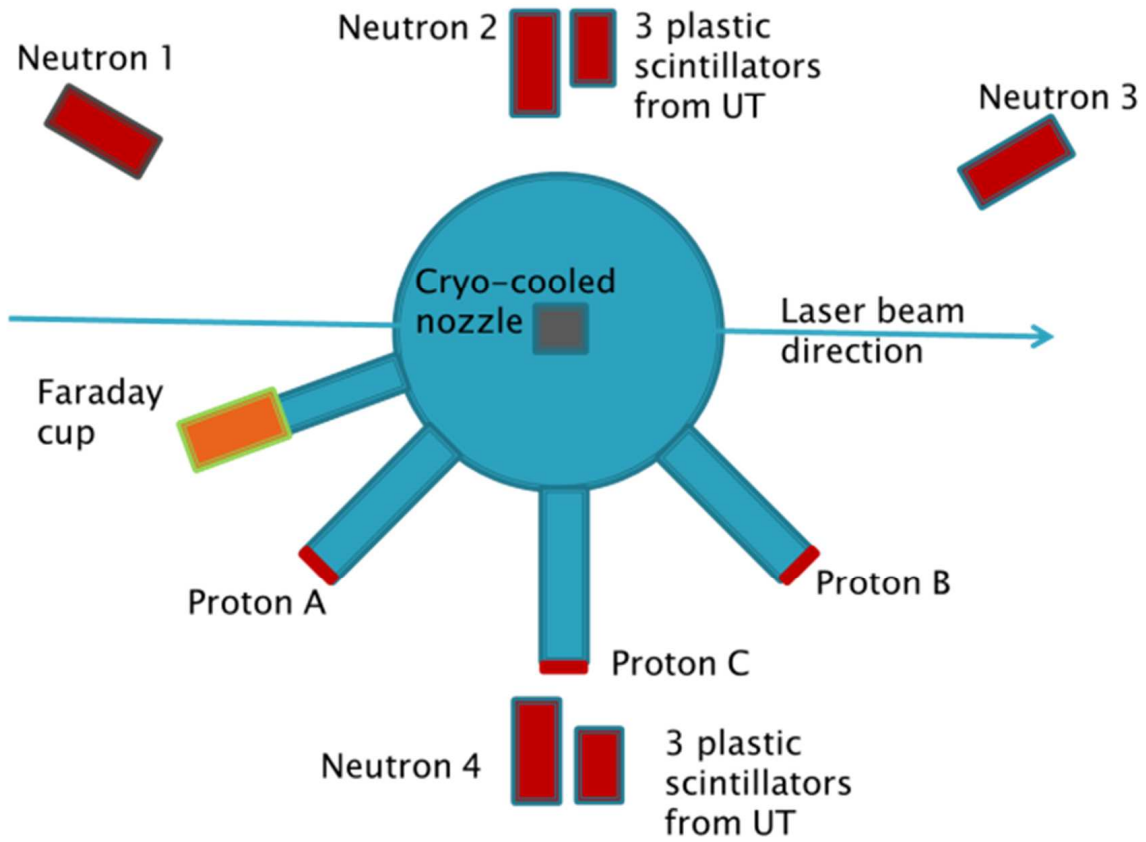
Figure 2.1: Diagram of the experimental setup. A Faraday cup, located 1.07m from the plasma with an opening diameter of 16 mm, provided TOF measurements of the energetic deuterium and carbon ions arriving from the plasma. Neutrons and protons detectors were also used for detecting the residual protons and neutrons produced in the reactions: $D(d, {}^3He)n$, $D(d, t)p$, and ${}^3He(d, p){}^4He$.

Table 2.1: TPW Faraday cup detector specifications.

Angle [deg]	Target distance [mm]	diameter [mm]
157.5°	1070	16

2.2 Particle Diagnostics

Ion kinetic energy distribution signals were measured using a Faraday cup (Table 1) of 16 mm diameter, placed at 157.5° relative to the laser direction at a distance of about 1.07 m from the target, with a -400 V bias [20, 21, 22, 30] . By measuring the Faraday cup signal (ΔV), one can determine the number of ions N hitting the cup as

$$\frac{dN}{dt} = \frac{\Delta V}{qeR_\Omega}.$$ (2.1)

In the above equation, q is the charge state, e=1.6×10^{-19} C is the electron elementary charge, R_Ω= 50 Ω is the Faraday cup impedance and ΔV is the electric potential difference measured. In Figure 2.1, we show a typical spectrum for the electric potential difference ΔV measured as function of time.

Unfortunately, in many experiments involving laser-plasma interaction, an intense emission of microwave electromagnetic field has been observed [25, 41, 42]. It normally affects the time response of all the detectors, often up to hundreds of nanoseconds since the laser pulse [41]. For detection of fast particles, this electromagnetic field can be high enough to hide any possible detectable signal (see Figure 2.1). This kind of situation has been observed at the TPW facility in laser-clusters interaction experiments [19, 20].
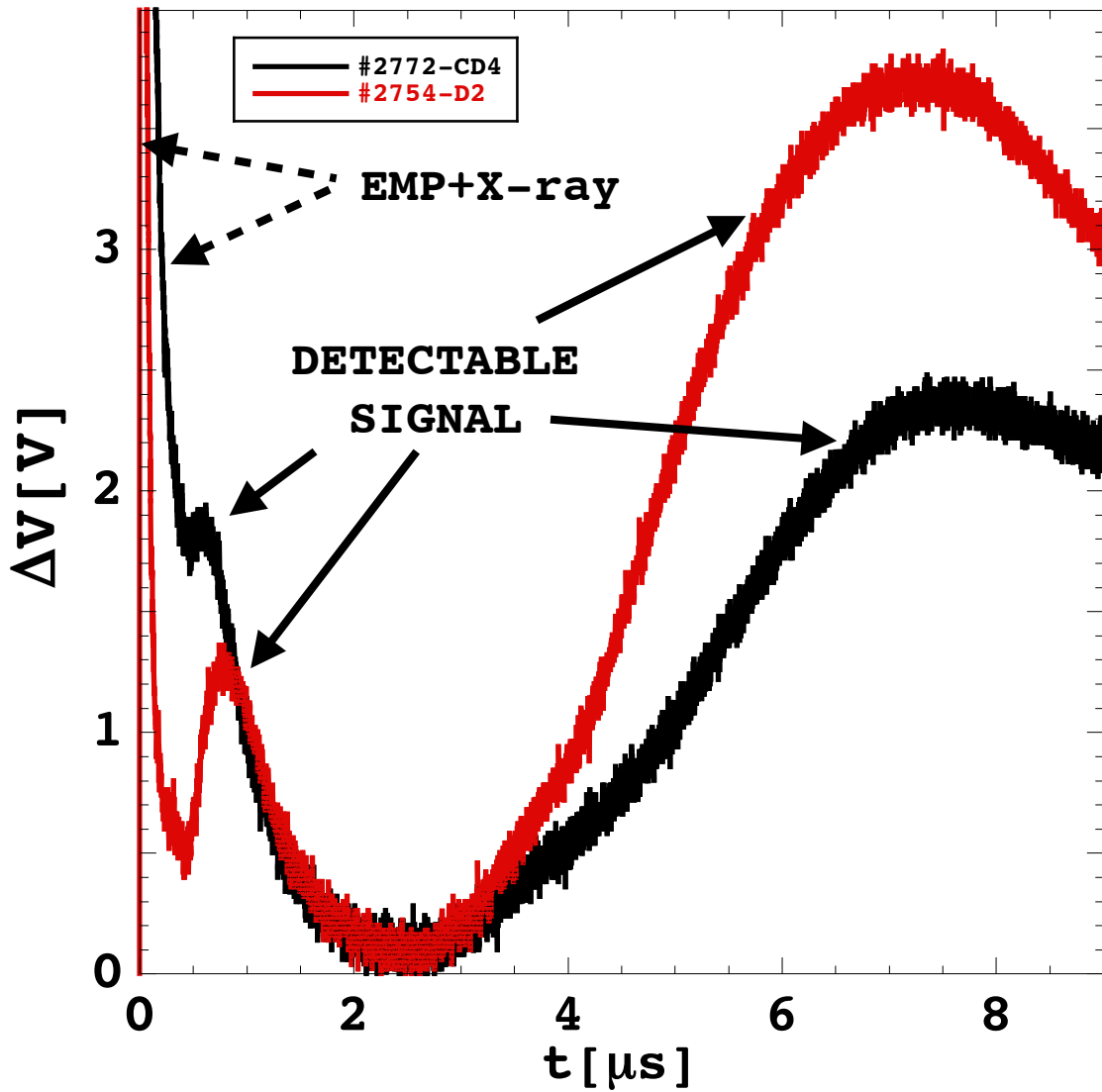
Figure 2.2: Measured ion signal from the Faraday cup detector for shots performed using a mixture of $D_2+{}^3He$ (red) or $CD_4+{}^3He$ (black). The spike in the signal is caused by the electromagnetic pulse and X-ray which affect the time response of the detector. The ions emission follows immediately after.

To better distinguish the detectable signal from the electromagnetic pulse (EMP)

and X-ray and sort of separate the ions regions from the background noise in the signal, we proceed with the analysis of the signals in energy space rather than time. This choice becomes clearer when looking at kinetic energy moments of the measured distribution function, see Figure 2.3. In order to transform the signals in energy space, we can derive the ions velocity v from the measured time t as

$$v = \frac{s}{t},\tag{2.2}$$

where s is the distance of the Faraday cup detector from the target. Then, this relationship follows

$$\frac{dt}{dE} = \frac{s}{mv^3}.\tag{2.3}$$

Therefore, the ion kinetic energy distribution per charge state q can be obtained from

$$\frac{d^2N}{dEd\Omega} = \frac{s^3}{mv^3\pi r_F^2}\frac{\Delta V}{qeR_\Omega}.\tag{2.4}$$

In the above equation, m is the ion mass, $d\Omega = \frac{\pi r_F^2}{s^2}$ is the solid angle and $r_F = 8$ mm is the radius of the Faraday cup detector. We will assume that the ion angular distribution is flat [19]. In order to distinguish the detectable ion signal from the EMP+X-ray and highlight these different structures, the system can be studied by multiplying the energy distribution by E^n (i.e., $n=0,1,2$). In Figure 2.3, we show some typical kinetic energy moments distributions of deuterium ions obtained using a mixture of D_2 and ^{3}He gases.
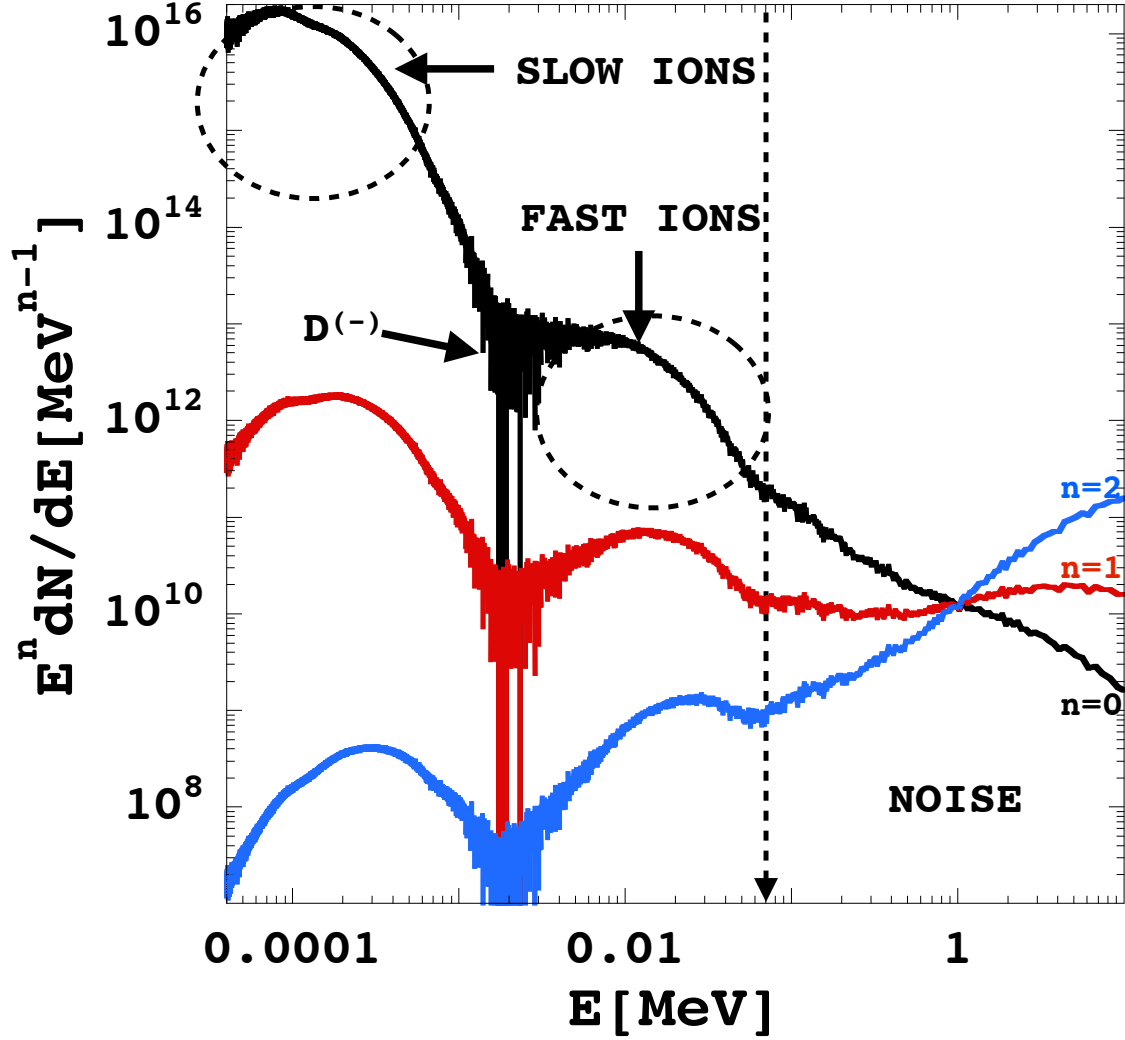
Figure 2.3: Ion kinetic energy moments distribution $n=0$ (black line), $n=1$ (red line) and $n=2$ (blue line) of the signals for a shot performed using a mixture of D_2+^3He. Moments analysis is a powerful tool to separate the electromagnetic noise from detectable signal.

Three regions were identified. In the low energy region below 1 keV, the ion signal belongs to the blast wave of the energetic plasma ions [19]. In the intermediate

region below roughly 70 keV, the ion signal represents the kinetic energy spectrum of deuterium ions coming from the Coulomb explosion of large clusters, these are the ions responsible for fusion reactions, especially d-d. d-^{3}He fusion reactions are mostly generated from ions very close to where the noise becomes dominant. In the high energy region starting from roughly 70 keV, the ion signal overlaps with the EMP and the X-ray "noise". From the energy moments distributions it is relatively easy to separate these three regions and distinguish the electromagnetic noise from the detectable signal. Notice the large oscillations in the distributions around 1 keV. Those oscillations are not due to the initial EMP nor to the X-ray, since they are detected after a relatively long time (>2 μs). We could assume that the energetic ions coming from the laser-cluster interaction region quickly expand into the cold region of the plasma (i.e. the part that was not irradiated by the plasma). In their path, they capture some electrons which are still in the surrounding medium and especially the lower energy ions might become negatively charged. Thus, it is the net sum of positive and negative charges which produces the oscillations. Negative ions of kinetic energies lower than 400 eV are rejected by the repulsive grid in the Faraday cup which terminates the oscillations. However, since such an energy region is irrelevant for the fusion reactions to occur, this feature is not discussed further in this work. Note that the ion signal roughly above > 70 keV, where the fusion cross-sections are large, is obscured by the noise. It is important to stress that, if relevant information is to be determined from these experiments, such as fusion cross sections [21, 23, 37], it is crucial to have a clean signal also above these energies interval. It is the same energy region that, as we will show in this paper, is absolutely needed to be able to distinguish the Maxwell-Boltzmann distribution from the log-normal distribution. Because of the noise shown in Figures 2.2-2.3, we analyzed the number of fusions to determine which energy distribution best reproduces the experimental

yields. We calculated the total number and energy spectrum of deuterium ions in the plasma, with the assumption of nearly isotropic emission [31, 43]. In future experiments, further improvements must be made in the detection of the plasma ion signal and the precision of the fusion particle yields.

In the following sections we will explore three possible ion kinetic energy distributions. First, we propose two similar ways of describing the recorded signals by using either a Maxwell-Boltzmann (MB) or a shifted Maxwell-Boltzmann distribution (sMB). Second, assuming that the motion of the ions within a cluster is chaotic enough to resemble thermalization, the experimental distribution measured is studied from a cluster size distribution point of view described by a log-normal (LN) distribution.

2.3   Plasma Ion Energy Distribution

Assuming that all the electrons are stripped by the laser light, the "naked" clusters will quickly explode because of the Coulomb repulsion [19, 20, 21, 23, 24, 25, 26, 27, 28, 29, 30, 31, 32, 33, 34, 35, 36] among the ions, and the kinetic energy will result in the measured temperature T. We assume that the ion energy distributions can be described by either Maxwell-Boltzmann [20, 21, 35] or shifted Maxwell-Boltzmann distribution (i.e., $E \rightarrow E - E_C$) [44]. In the second scenario, we find that the ions go through a cloud of electrons and experience a positive attraction or energy loss causing a shift in the energy distribution. The kinetic energy moments distributions of the ions can be written as

$$E^n \frac{d^2Q}{dEd\Omega} = \frac{N_0}{\sqrt{\pi T^3}} E^n (E - E_C)^{\frac{1}{2}} e^{-\frac{(E-E_C)}{T}}.$$ (2.5)

The normalizing constants N_0 entering in the equation gives approximately the number of ions produced times the charge state. The kinetic energy moments distribu-

22

tions per charge state can be written as

$$E^n \frac{d^2 N}{dE d\Omega} = \frac{1}{q} E^n \frac{d^2 Q}{dE d\Omega} \tag{2.6}$$

with $q=1$ for D nuclei. The total number of particles per charge state $\langle N \rangle$ can be obtained by integrating the kinetic energy distribution ($n=0$) as

$$\langle N \rangle = \frac{1}{q} \int \frac{d^2 Q}{dE d\Omega} \, dE d\Omega. \tag{2.7}$$

The average energy can be obtained in a similar fashion with $n=1$, then the total energy per charge state $\langle E \rangle$ can be written as

$$\langle E \rangle = \langle N \rangle \left(E_C + \frac{3}{2} T \right). \tag{2.8}$$

Particle features like temperature and collective energy can be obtained from the distributions analysis in energy space. The dynamical evolution of measurable quantities like particle temperature and Coulomb energy can be described via Eq. (2.5). These sets of equations show maxima at

$$E_{max}(\kappa) = \frac{\kappa}{2} \pm \frac{\kappa}{2} \sqrt{1 - \frac{4n}{\kappa^2} T E_C}, \tag{2.9}$$

where

$$\kappa \equiv E_C + \frac{2n+1}{2} T. \tag{2.10}$$

Therefore, the kinetic energy moments distributions for these maxima are

$$E^n \frac{d^2 Q_{max}}{dE d\Omega} = \frac{N_0}{\sqrt{\pi T^3}} E_{max}^n(\kappa)(E_{max}(\kappa) - E_C)^{\frac{1}{2}} e^{-\frac{E_{max}(\kappa) - E_C}{T}}. \tag{2.11}$$

For each ions region (i.e., fast ions and slow ions) or charge state in systems with multiple charge states (e.g., ^{6}Li, ^{11}B, ^{197}Au), we plot the maxima as function of the order n and derive the values T and E_C from Eqs.(2.9) and (2.11) (see Figure 2.4). Both equations indeed offer a clever way of extracting temperature and collective energy for each charge state by studying the energy moments of the corresponding Maxwell-Boltzmann or shifted Maxwell-Boltzmann distribution. The analysis of ion kinetic energy moments measured for D-cluster gas is done considering charge state q=1. The ^{3}He ions do not from clusters at the nozzle temperatures of the experiment, thus they remain "cold' and localized at very small energies close to zero. For each shot we analyzed both energetic regions (i.e., fast ions and slow ions). A distribution is used for each energy region, the low and the intermediate region respectively. Note that for the shots examined, the shifted MB distribution for the intermediate energy region gives an average negative $E_C \sim$-11 keV. This could be consistent with a deceleration due to a cloud of electrons still surrounding the exploding clusters causing a total positive shift in the energy because of the attractive collective energy (i.e., negative potential) experienced by the ions.

In Figure 2.5 we fit the measured data in the low and intermediate energy region using a Maxwell-Boltzmann distribution or a shifted Maxwell-Boltzmann distribution from the extrapolated data via energy moments analysis. On the shots considered, we observed an average deuterium ion kinetic energy of 12.9$\pm$2 keV, or kT=8.6$\pm$2 keV defined as two thirds of the average kinetic energy of deuterium ions, compared to an average deuterium ion kinetic energy of 14.3$\pm$2 keV, or kT=9.5$\pm$2 keV and E_C=-10.9$\pm$0.3 keV if describing the signals with shifted MB distributions. The normalization constant N_0 is about 10^{16} in the first scenario, whereas for a shifted Maxwell-Boltzmann distribution this constant of normalization doubles (i.e., about 2×10^{16}). These small differences could be further resolved with a better precision in

24

the measurements of the ion kinetic energy distributions.

In Figure 2.6 we compare the measured ion kinetic energy distribution with the two distributions obtained using a MB and a shifted MB distribution. It is important to note that the fusion plasmas might not be in thermal equilibrium even though the Maxwell-Boltzmann distribution reproduces the experimentally measured ion energy spectrum rather well. The consistency of this distribution scenario also remains when introducing a collective energy. However, the energetic deuterium ions in the plasma have such high kinetic energies that their mean free paths (>10 mm) are longer than the size of the gas jet, and thermalization from ion-ion collisions or ion-electrons is not expected under our experimental conditions. Previous studies have in fact shown that near-Maxwellian ion energy distribution is observed not because of thermalization of ions, but because of cluster size distribution [31, 36]. In the following section, we consider this possibility that a near-Maxwellian energy distribution results from the log-normal size distribution of clusters in our gas jet.
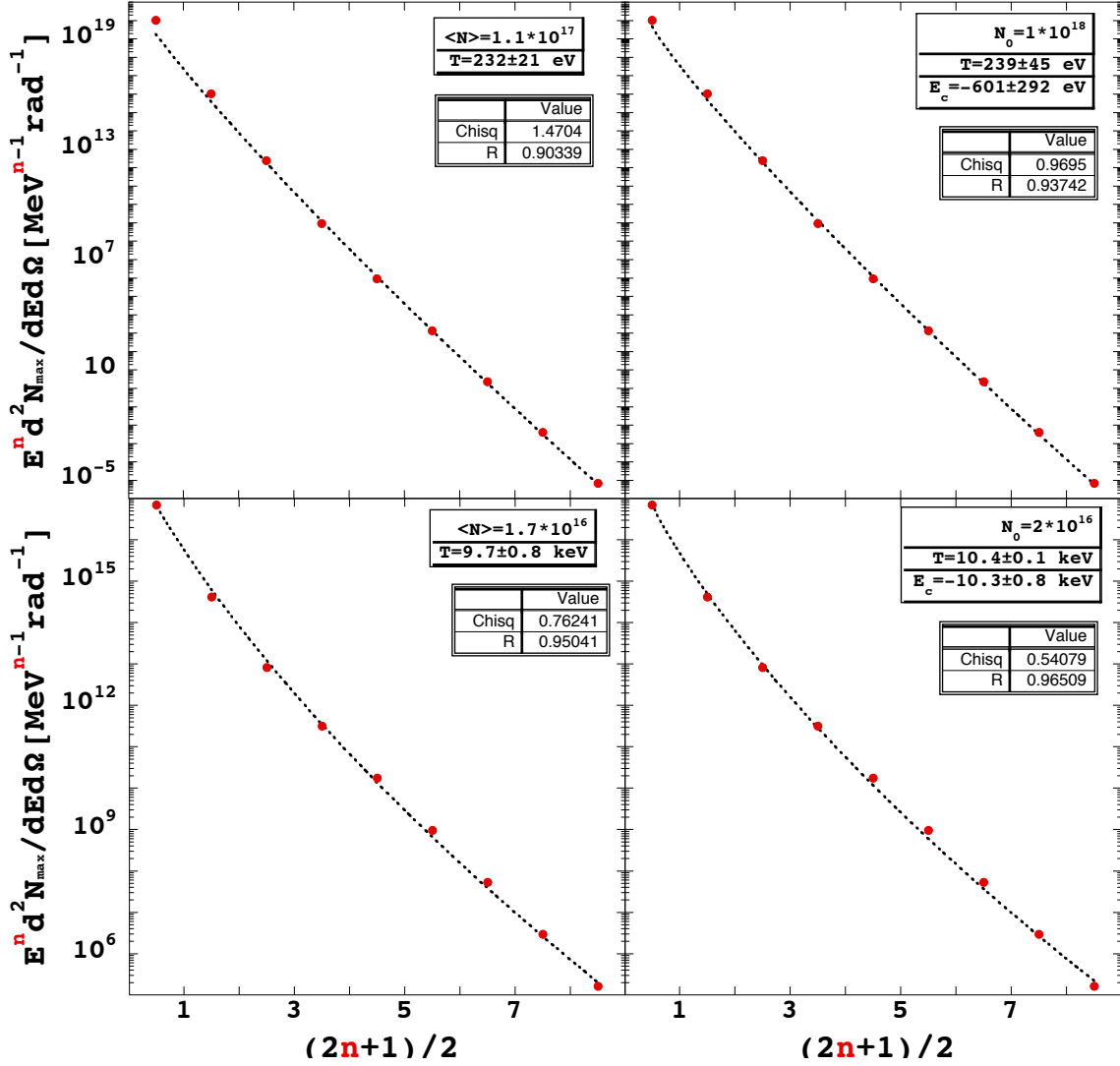
Figure 2.4: Energy moments analysis via Eq. (2.11) performed on the intermediate energy region (bottom panel) and low energy region (top panel) using a Maxwell-Boltzmann distribution $E_C = 0$ (left panel) compared to a shifted Maxwell-Boltzmann distribution $E_C \neq 0$ (right panel). Energy moments analysis can be used to extract temperature and collective energy for each charge state (i.e, $q = 1$ for D).
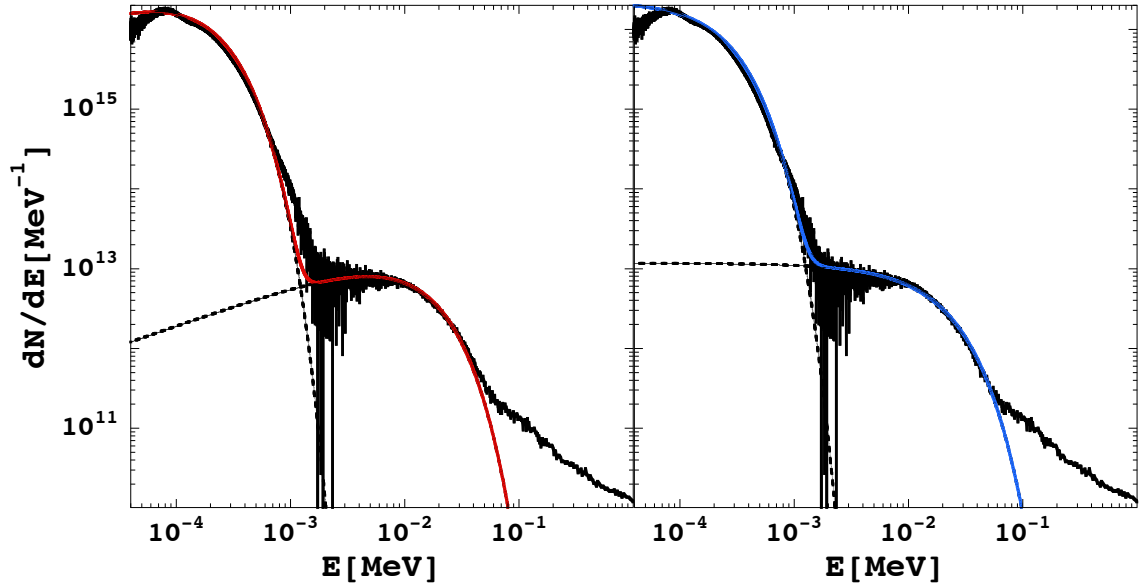
Figure 2.5: Ion kinetic energy distributions obtained using a Maxwell-Boltzmann distribution $E_C{=}0$ (left panel) or a shifted Maxwell-Boltzmann distribution $E_C \neq 0$ (right panel) for a shot performed using a mixture of $D_2{+}^3He$. The dashed lines correspond to a fit of each ion region (i.e., fast ions and slow ions) whose sum gives the total contribution (solid line).
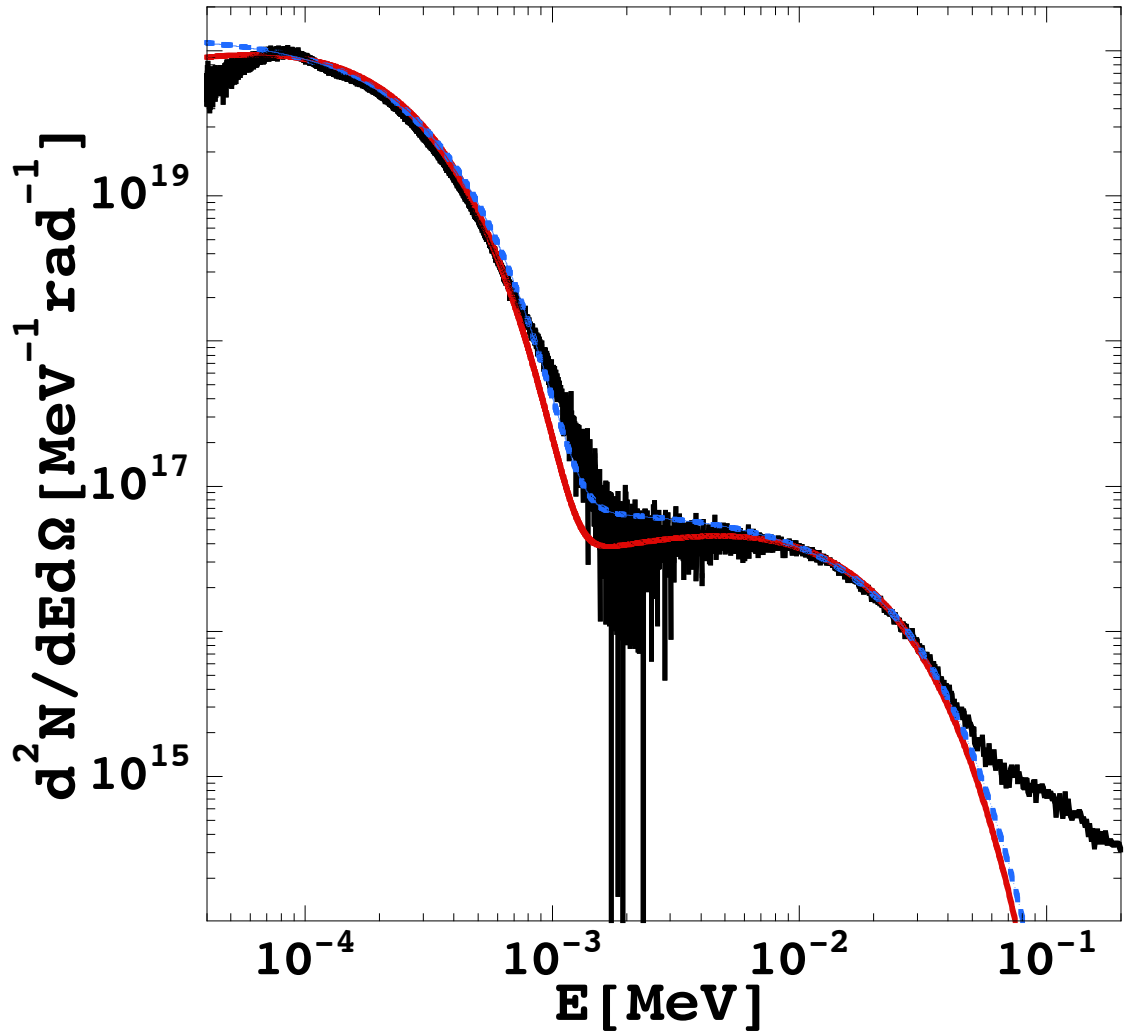
Figure 2.6: Ion kinetic energy distributions obtained using a Maxwell-Boltzmann distribution $E_C = 0$ (red solid line) or a shifted Maxwell-Boltzmann distribution $E_C \neq 0$ (blue dashed line) for a shot performed using a mixture of $D_2 + {}^3He$. Some differences between these models might be noticed near the high momentum tails, which are crucial for fusion reactions.

2.4 Plasma Ion Energy Distribution: Part II

In this section we will explore the possibility that the motion of the ions within a cluster is chaotic enough to resemble thermalization. This is typical of many bodies interacting through long range forces which give rise to chaos already for a 3 particle system [45]. Microscopic simulations of such processes show that fusion might indeed occur even though a collective motion is initially imposed to the system [46]. Here we do not suggest that it is either one mechanism or the other, but simply we want to explore a different scenario and maybe suggest how to assess their relative contributions experimentally. Previous studies of cluster production in gas jets have found that the experimentally measured size distribution is best described by a log-normal distribution [20, 31, 35, 43, 47, 48, 49, 50]. In that case the clusters of size M density moments can be written as [31]

$$M^n \frac{dN}{dM} = \frac{M_0 M^{n-1}}{\sqrt{2\pi\sigma^2}} exp(-\frac{(\ln M - \mu)^2}{2\sigma^2}). \tag{2.12}$$

Where n=0,1,2. In the above equation, M_0 is a normalization constant, μ and σ are the mean and the standard deviation of the distribution of the natural logarithm of the size. Assuming the relation between the radius and the number of ions M in the cluster is

$$R_{cl} = r_s M^{\frac{1}{3}}, \tag{2.13}$$

where $r_s = (\frac{3}{4\pi\rho_{cl}})^{\frac{1}{3}} = 1.7\text{Å}[32]$, then the Coulomb energy V_C per particle for a uniformly charged sphere of radius R_{cl} can be written as [26]

$$\frac{V_C}{M} = 5.1 M^{\frac{2}{3}}(eV) \equiv E_d. \tag{2.14}$$

Then, this relationship follows

$$\frac{dE}{dM} = 3.4M^{-\frac{1}{3}}. \tag{2.15}$$

Thus we are assuming that the kinetic energy of a deuterium ion is due to the Coulomb explosion of a cluster of size M. Different cluster sizes result in different ion energies. The relation between the quantities E_d and M can therefore be estimated from the equation above and the Maxwell-Boltzmann function (i.e., $n=0$) can be rewritten in terms of M as

$$\frac{dN}{dM} = \frac{3.4N_0}{M^{\frac{1}{3}}\sqrt{\pi T^3}}((5.1M^{\frac{2}{3}}) - E_C)^{\frac{1}{2}}e^{-\frac{((5.1M^{\frac{2}{3}})-E_C)}{T}}. \tag{2.16}$$

This allows us to analyze the cluster size distribution in terms of a "pseudo" Maxwell distribution. Alternatively, from the log-normal distribution function, we obtain the ion kinetic energy distribution function (i.e., $n=0$) using the same relationships as

$$M = 0.09E_d^{\frac{3}{2}}, \tag{2.17}$$

and

$$\frac{dM}{dE} = 0.13E_d^{\frac{1}{2}}. \tag{2.18}$$

These kinetic energy ion distributions obtained from the clusters size distributions equations can be compared with the Maxwell-Boltzmann distributions as

$$\frac{dN}{dE} = \frac{1.4M_0}{E\sqrt{2\pi\sigma^2}}e^{-\frac{(\ln(0.09E^{\frac{3}{2}})-\mu)^2}{2\sigma^2}}. \tag{2.19}$$

Notice that an alternative derivation of the above result is discussed in [26]. Even though the two approaches seem to present different functional terms, the logarithm

30

dependence of the energy produce similar results at high energies and therefore we will not discuss further the latter in this paper. These sets of equations can be used to study the plasma ion kinetic energy moments distribution via Eqs. (2.6) and (2.19) or the cluster size moments distribution produced using Eqs. (2.12) and (2.16), see Figures 2.7-2.10. In Eqs. (2.12) and (2.19), the presence of the natural logarithm makes the functions decrease slower at higher energy and larger cluster size (i.e., log-normal distribution goes to zero slower for energy or cluster size approaching infinity). This is shown in Figures 2.7-2.10 where discrepancies among the different distributions are especially visible for relative high energies (> 70 keV) and large cluster sizes. For this reason, the fact that despite all distributions are able to describe the measured distribution quite well, the substantial difference these show in the high momentum tail of the signal will be dominant when calculating the fusion reactions yield. This analysis might give us a hint as to which one is the process that governs the energy distribution of the plasma we measure, and perhaps show us the true nature of the signals recorded.
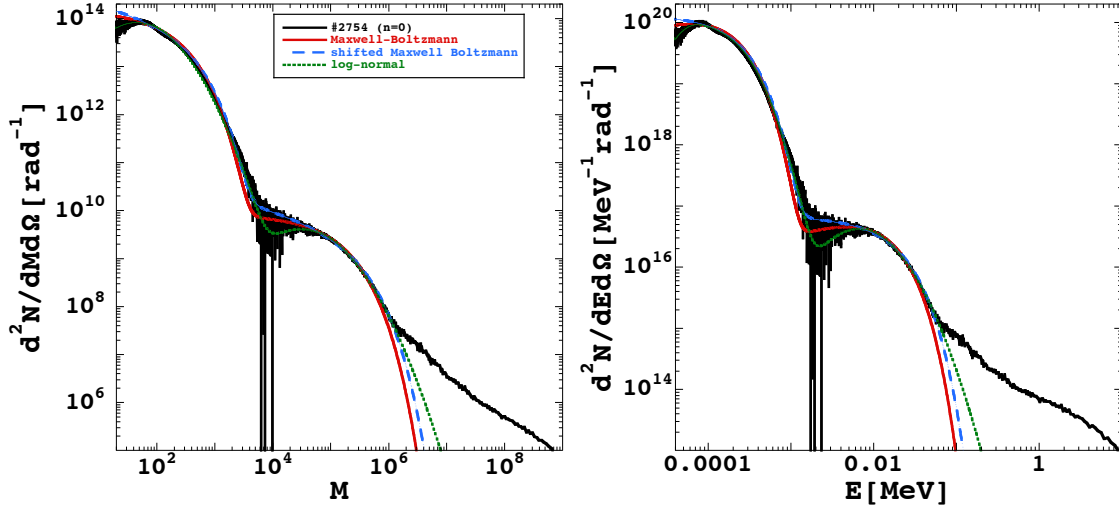
Figure 2.7: Cluster size distributions (left panel) and ion kinetic energy distributions (right panel) for n=0. Maxwell-Boltzmann distribution (solid red), shifted Maxwell-Boltzmann distribution (dashed blue) and log-normal distribution (dotted green) are plotted. Note especially the big differences for large cluster sizes. Thus a precise measurement of the high energy ions is crucial to distinguish the different distribution used. Alternatively a calculation of the fusion reactions yield can exclude some of the hypothesized distributions (or all).
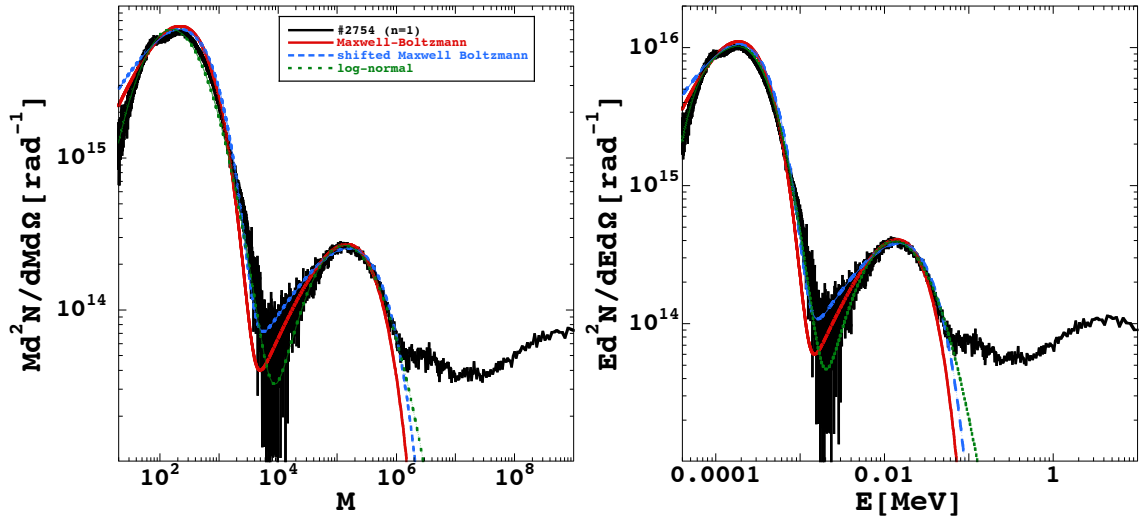
Figure 2.8: Cluster size distributions (left panel) and ion kinetic energy distributions (right panel) for n=1. Maxwell-Boltzmann distribution (solid red), shifted Maxwell-Boltzmann distribution (dashed blue) and log-normal distribution (dotted green) are plotted.

Figure 2.9: Cluster size distributions (left panel) and ion kinetic energy distributions (right panel) for n=2. Maxwell-Boltzmann distribution (solid red), shifted Maxwell-Boltzmann distribution (dashed blue) and log-normal distribution (dotted green) are plotted. The noise is clearly visible, it occurs exactly where the distributions differ.
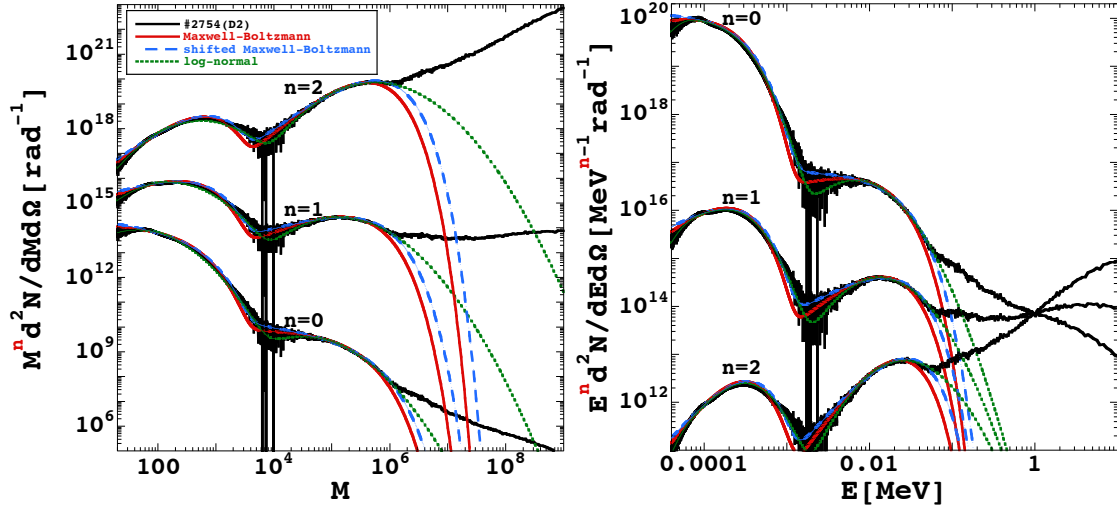
Figure 2.10: Cluster size density moments (left panel) and ion kinetic energy moments distributions (right panel) for n=0,1,2. Maxwell-Boltzmann distribution (solid red), shifted Maxwell-Boltzmann distribution (dashed blue) and log-normal distribution (dotted green) are plotted.

From Figure 2.10, we could conclude that all distributions reproduce the data relatively well up to the region where the noise becomes dominant (high energy region). Thus we need further information to distinguish them. This might be accomplished by comparing the number of fusions obtainable from the fitted distributions with the experimentally measured fusion yields. A closer look at the plasma ion kinetic energy distribution is given in Figure 2.11. Since the fusion cross sections for d-d and d-^{3}He reactions are very sensitive to the high energy tails of the plasma ion distributions, it is very important to determine the true nature of measured distribution signals and perform the data extrapolation precisely. In the next section, we will show that the plasma ion kinetic energy distributions and the fusion yields are consistent with MB and shifted MB. The LN distribution does not reproduce all the experimental data

at the same time. In particular, the LN1 distribution (dotted green line) is able to reproduce the measured ion kinetic energy distribution quite well but not the fusion yield, and vice versa the LN2 (dash-dot orange line). In Tables 2.2-2.3, there is a summary of the parameters entering Eqs. (2.5) and (2.19) used to describe the ion kinetic energy distribution measured in the intermediate energy region.

Table 2.2: List of the parameters entering the Maxwell-Boltzmann (MB) and the shifted Maxwell-Boltzmann (sMB) distribution equation for the intermediate energy region.

#SHOT	T [keV] (MB)	T [keV] (sMB)	$-E_C$ [keV] (sMB)
2742	7.8	9.0	11.0
2743	7.9	9.0	11.0
2744	8.5	9.0	10.0
2745	8.5	10.0	11.0
2746	10.0	11.0	11.0
2748	8.5	9.5	11.0
2750	8.5	9.5	11.0
2753	11.0	12.0	11.0
2754	9.3	10.5	11.0
2755	5.0	5.5	11.0
2763	10.0	10.0	11.0

Table 2.3: List of the parameters entering the log-normal (LN) distribution equation for the intermediate energy region.

#SHOT	μ (LN1)	σ (LN1)	μ (LN2)	σ (LN2)
2742	11.6	1.3	11.5	0.9
2743	11.7	1.1	11.6	0.9
2744	11.9	1.1	11.9	0.8
2745	12.0	1.1	11.9	0.8
2746	12.1	1.3	12.0	0.9
2748	12.0	1.1	11.9	0.8
2750	11.8	1.2	11.7	0.9
2753	12.0	1.4	12.2	0.9
2754	11.8	1.2	11.9	1.0
2755	12.0	1.0	12.1	0.8
2763	11.8	1.1	11.8	1.0
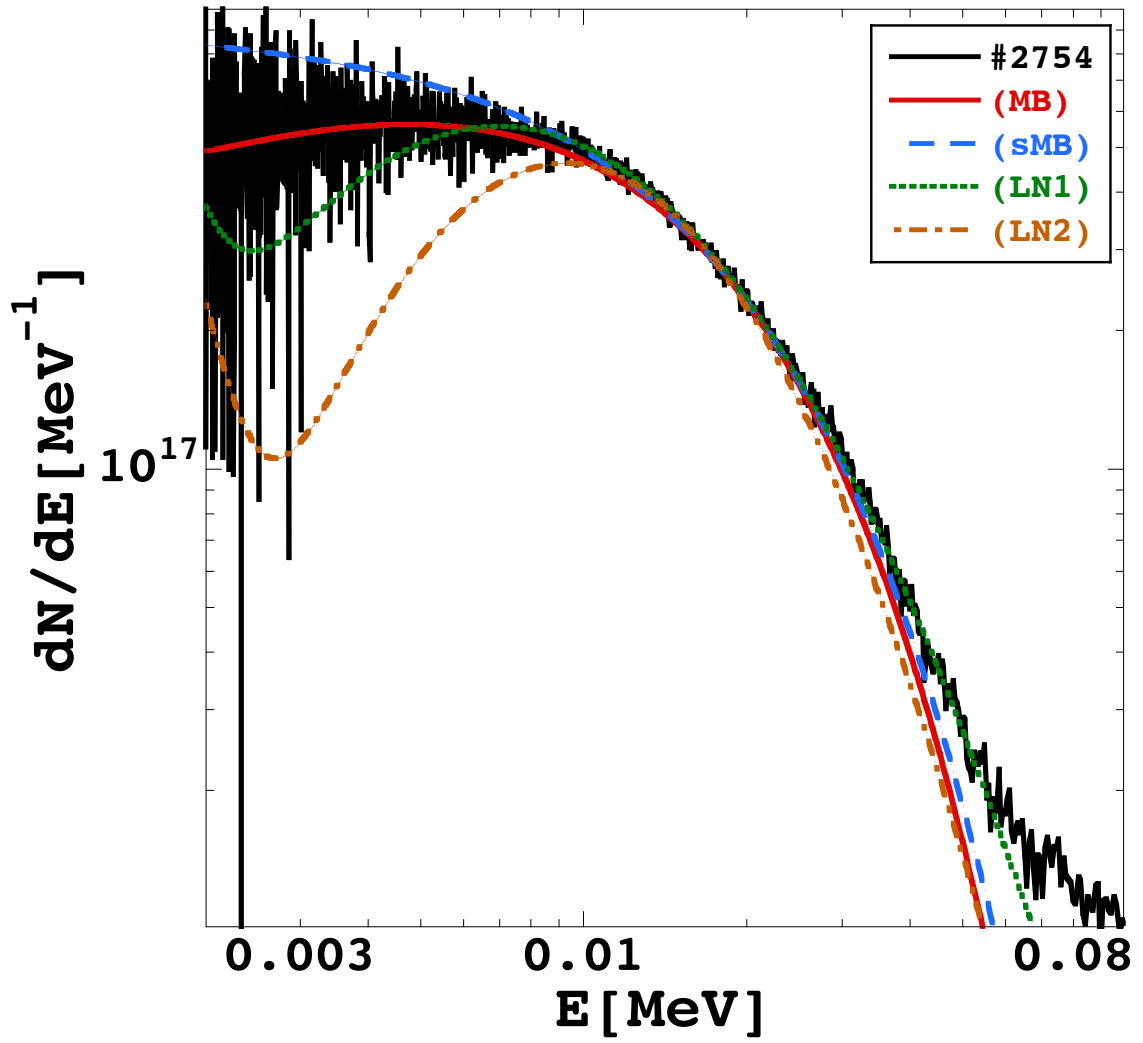
Figure 2.11: Comparison between different plasma ion kinetic energy distributions (n=0) in the intermediate energy region. MB distribution (solid red line), shifted MB distribution (dashed blue line) and log-normal distributions LN1 (dotted green) and LN2 (dash-dot orange line) are plotted.

3. FUSION REACTIONS

During the experiments [20, 21, 30], an intense ultra-short laser pulse irradiates either D_2 or CD_4 clusters mixed with ^{3}He gas, simultaneously producing three types of nuclear fusion reactions in the interaction volume: D(d, t)p, D(d, ^{3}He)n and ^{3}He(d, p)^{4}He (Figure 3.1). In Table 3.1, a detailed summary of the nuclear fusion reactions in question is reported. For d-^{3}He fusion reactions, the ^{3}He ions are regarded as stationary since they remain cold after the intense laser pulse is gone (i.e., ^{3}He atoms do not absorb the laser pulse energy efficiently because they do not form clusters at the nozzle temperature of 86 K [30, 39]). We analyze both fusion yields of neutrons and protons produced in three different scenarios of ion kinetic energy distributions (i.e., Maxwell-Boltzmann (MB), shifted Maxwell-Boltzmann (sMB) and log-normal (LN) distributions). In fact, each one of the ion kinetic energy distribution described will determine a different fusion cross section. In order to test our distributions, we estimate the fusion yield under each different scenario via Eq. (1.8). Similar to [20, 21, 30], we focus on the study of the reactions from which 2.45 MeV neutron (Y_n) and 14.7 MeV proton (Y_p) yields are produced. We show that the fusion yields and the plasma ion kinetic energy distributions are consistent with MB and sMB. The LN distribution does not offer a good representation of the measured ion signal when reproducing the measured fusion yields.
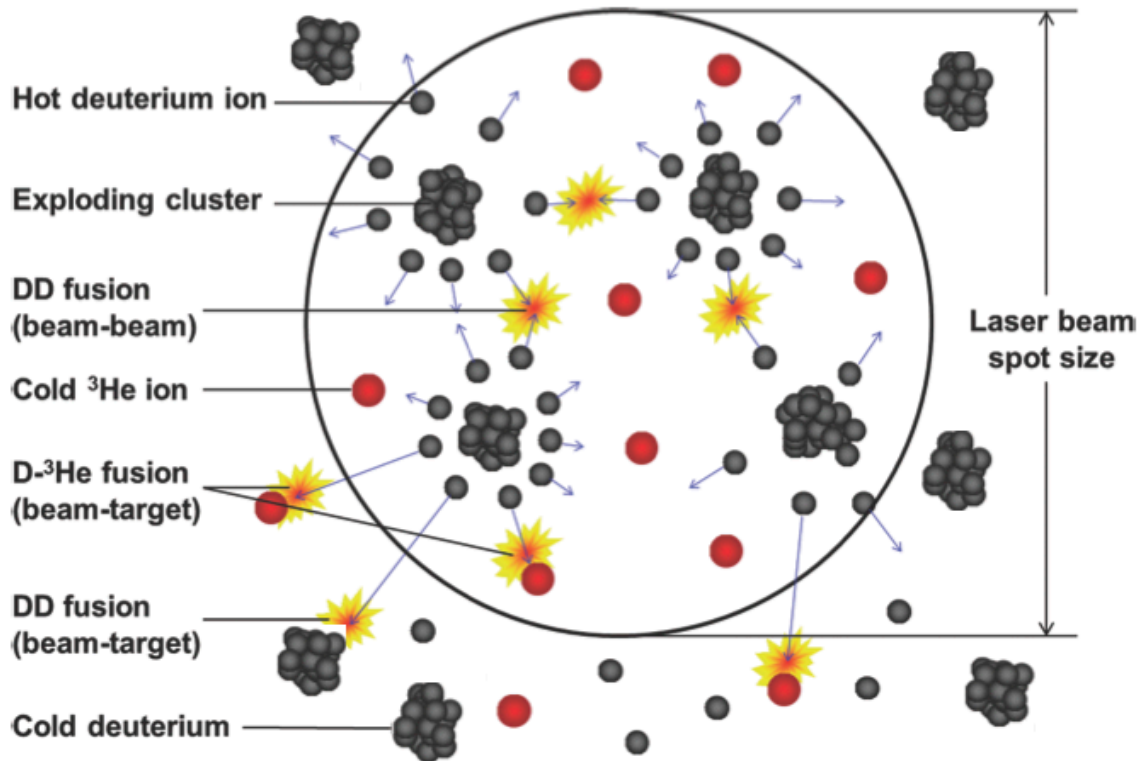
Figure 3.1: Some of the possible fusion reactions inside the plasma plume [30]. The bigger red spheres indicate cold ^{3}He ions or atoms. The smaller black spheres represent energetic deuterium ions or cold deuterium atoms depending if they happen to be inside the laser beam spot size or not. The ^{3}He ions are regarded as stationary since they remain cold before and after the intense laser pulse hits. d-d fusion reactions can be generated when energetic deuterium ions collide with each other or with cold deuterium atoms in the background gas jet outside the focal spot.

Table 3.1: Some of the possible fusion reactions inside the plasma when both D_2 clusters and ^{3}He atoms are present.

Reaction	Q [MeV]	Probability
D+d → T+p	4	50%
D+d→ ^{3}He+n	3.3	50%
^{3}He+d → α + p	18.4	100%

3.1   D(d, ^{3}He)n

As previously discussed, the kinetic energies of the deuterium ions resulting from the Coulomb explosion mechanism reach several keV so that d-d fusion reactions can be generated when energetic deuterium ions collide with each other, called beam-beam fusion ($Y_{n(BB)}$), or with cold deuterium atoms in the background gas jet outside the focal spot, called beam-target fusion ($Y_{n(BT)}$), see also [51]. Similar to [20, 21, 22, 30, 52], we will estimate the probability of d-d fusion in the cluster plume in the limit where the plasma disassembly time for collisions involving hot deuterium ions only (BB) can be approximated as

$$\tau_{BB} = \frac{l}{v}. \tag{3.1}$$

In the above equation, l is the radius of a sphere with volume equal to a cylindrical plasma of radius, r, and height, $2R$, and v is the speed of the hot deuterium ions. On the other hand, for collisions between hot deuterium ions with cold deuterium

atoms (BT), the plasma disassembly time can be estimated as

$$\tau_{BT} = \frac{R - l}{v}. \tag{3.2}$$

Thus, we consider only the region outside the fusion plasma, over a distance *(R-l)*.

Therefore, the 2.45 MeV neutron yield $Y_n = Y_{n(BB)} + Y_{n(BT)}$ is calculated as [20, 21, 22, 30, 52]

$$Y_n = \frac{\rho_D N \langle \sigma \rangle_{dd_{(BB)}} l}{2} + \rho_D N \langle \sigma \rangle_{dd_{(BT)}} (R - l). \tag{3.3}$$

where N is the total number of energetic deuterium ions in the plasma, ρ_D is the average atomic number density of deuterium cluster plume, $\langle \sigma \rangle_{dd_{(BB)}}$ is the average fusion cross section between hot deuterium ions, $\langle \sigma \rangle_{dd_{(BT)}}$ is the average fusion cross section between hot deuterium ions and cold deuterium atoms at $\frac{T}{2}$ since one of the ions is cold (i.e., $E_{c.m.}^{dd_{(BT)}} = \frac{1}{2} E_{c.m.}^{dd_{(BB)}}$) [20, 21, 22, 30].

3.2 ^{3}He(d, p)^{4}He

The probability of d-^{3}He fusions in the cluster plume is estimated in the limit where the plasma disassembly time is determined as

$$\tau_{d^3He} = \frac{R}{v}. \tag{3.4}$$

Therefore, the 14.7 MeV proton yield is calculated as [20, 21, 30]

$$Y_p = \rho_{^3He} N \langle \sigma \rangle_{d^3He} R, \tag{3.5}$$

where $\rho_{^3He}$ is the average atomic number density of ^{3}He and $\langle \sigma \rangle_{d^3He}$ is the average fusion cross section between hot deuterium ions and cold ^{3}He ions at $\frac{3}{5} T$ since ^{3}He is at rest (i.e., $E_{c.m.}^{d^3He} = \frac{3}{5} E_{c.m.}^{dd_{(BB)}}$) [20, 21, 22, 30]. In our calculations, we make use

of the deuterium cluster density and ^{3}He concentration measured during each shot. Then, to determine which plasma ion kinetic energy distribution best reproduces the experimental yields, the average fusion cross section of each reaction is estimated numerically or analytically from each distribution as

$$N \langle \sigma \rangle = \int_0^\infty \sigma(E) \frac{dN}{dE} dE. \tag{3.6}$$

In the above, $\sigma(E)$ is the cross section of the reaction considered (i.e., d-d and d-^{3}He) and $\frac{dN}{dE}$ is the distribution function (i.e., MB, sMB or LN distributions). In Figure 2.11, a typical situation is displayed where both the Maxwell-Boltzmann, the shifted MB and the log-normal distributions reproduce the measured ion signal correctly. The only substantial differences among them are in the high momentum tail of the signal. As mentioned above, these deviations become more dominant when calculating the fusion yield because the average cross section in Eq. (3.6) is the convolution between the cross section, which increases exponentially at higher energies, and the distribution function which decreases for increasing energies. The log-normal distribution function indeed decreases slower at higher energy because of the natural logarithm dependence in the exponent, which results in an overestimate of the fusion yields, see Figure 3.4 (LN1, top panels). Of course this can be corrected by making opportune adjustment to the log-normal distribution, building the distribution (see Figure 2.11, dash-dot orange line) so that we are able to reproduce the measured fusion yields, see Figure 3.4 (LN2, top panels) . In this case though, the adjusted distribution does not reproduce the experimentally measured high energy ion spectrum. The quantities $\frac{dY_{n(BB)}}{dE} = \rho \sigma(E) l \frac{dN}{dE}$ and $\frac{dY_p}{dE} = \rho_{^3He} \sigma(E) l \frac{dN}{dE}$ are plotted in Figures 3.2-3.3 for the different plasma ion kinetic energy distributions. The fusion cross sections $\sigma(E)$ are taken from Ref. [9].

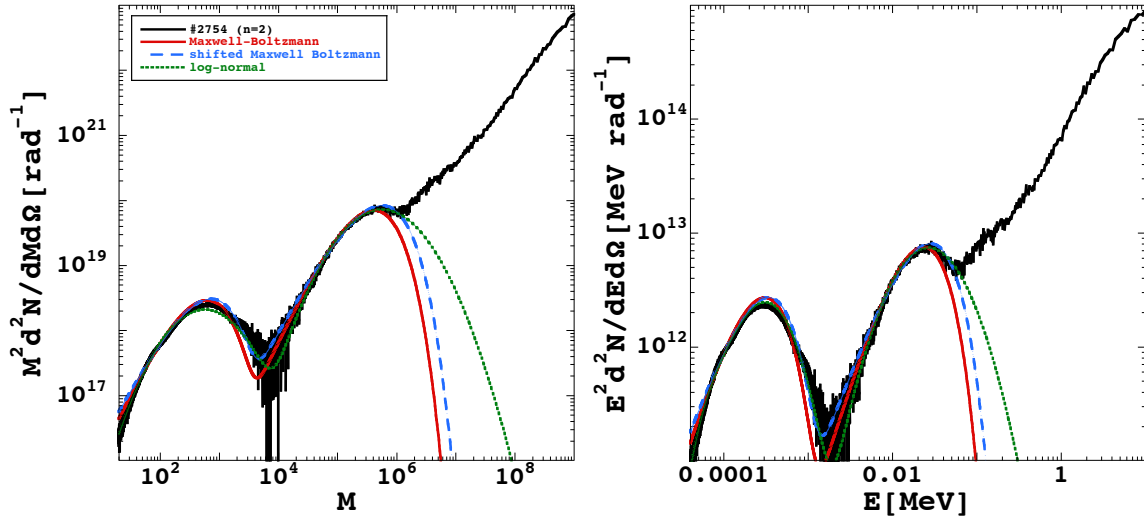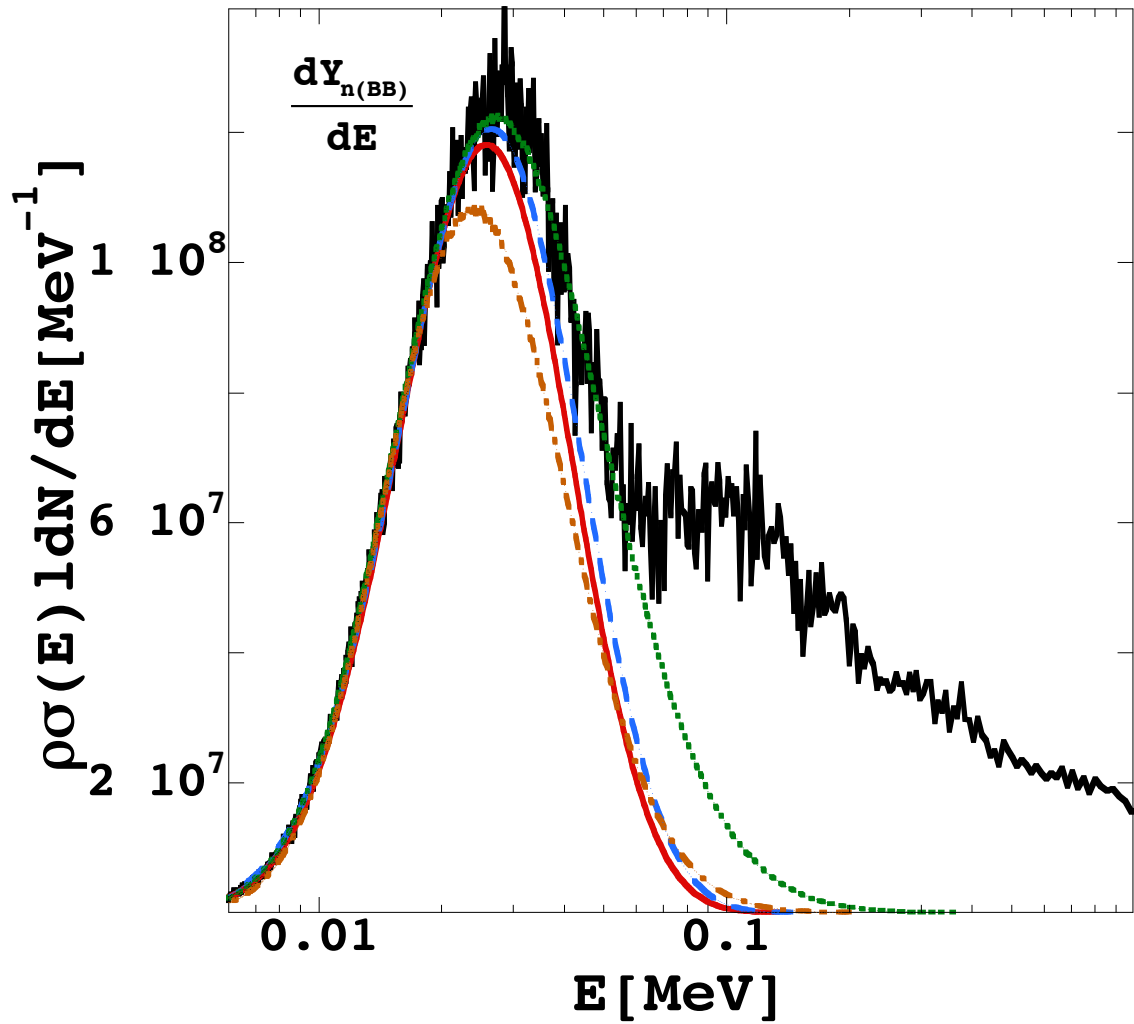Figure 3.2: Maxwell-Boltzmann distribution (MB, solid red line), shifted Maxwell-Boltzmann distribution (sMB, dashed blue line) and log-normal distribution (LN2, dash-dot orange line) all give the correct measured fusion yields within the error bars. The log-normal distribution LN1 (dotted green line), which describes the ion signal correctly, does not reproduce the number of fusions measured, especially d-^{3}He which is more sensitive to the highest energies. A more precise measurement of the fusion yields, i.e. with smaller error bars, might distinguish further among the different distributions.
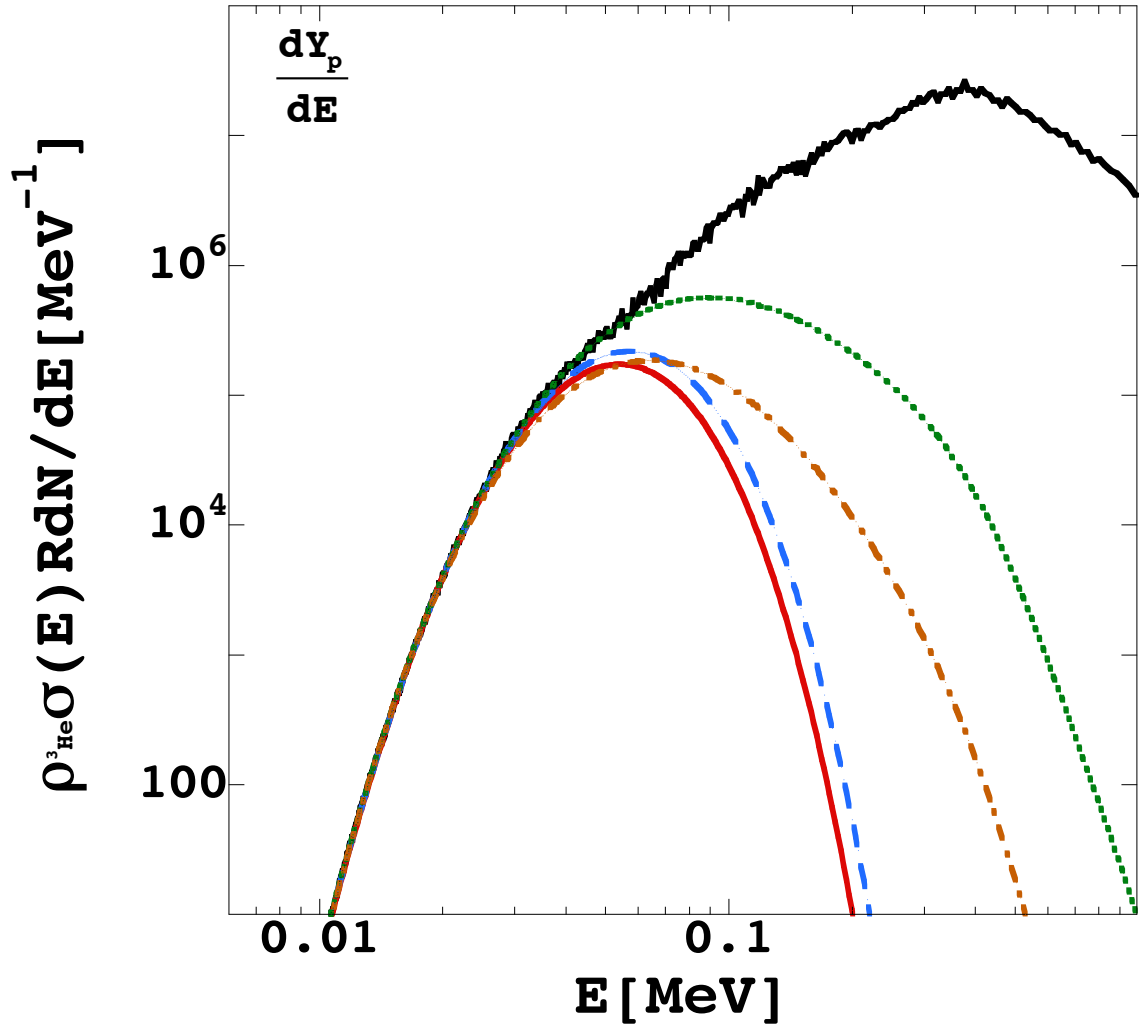
Figure 3.3: Maxwell-Boltzmann distribution (MB, solid red line), shifted Maxwell-Boltzmann distribution (sMB, dashed blue line) and log-normal distribution (LN2, dash-dot orange line) all give the correct measured fusion yields within the error bars. The log-normal distribution LN2 (dotted green line), which describes the ion signal correctly, does not reproduce the number of fusions measured, especially d-^{3}He which is more sensitive to the highest energies. A more precise measurement of the fusion yields, i.e. with smaller error bars, might distinguish further among the different distributions.

The integral of the quantity displayed in the Figure 3.2 gives the fusion yield obtained for d-d from the hot deuterium ions fusion reactions ($Y_{n(BB)}$), while the integral of the quantity displayed in the Figure 3.3 gives the fusion yield obtained for d-^{3}He fusion reactions (Y_p). In Figure 3.4, we plot the number of fusions obtained in different shots and compared to the estimates from the LN distributions (top panels) and the Maxwell-Boltzmann and the shifted MB distributions (bottom panels). The convolution of the distribution function with the fusion cross sections exhibits a maximum which is usually referred as Gamow energy peak E_G [12, 13]. Such a quantity could be directly determined from the data only for the d-d case [23] (see Figure 3.2) because of the noise. We can easily estimate it for each theoretical distribution and for both nuclear reactions. The calculated number of fusions as function of the Gamow energy peak is also given in Figure 3.4 (right panels). Note that the d-^{3}He results in a higher Gamow energy because of the higher Coulomb barrier, thus it is more sensitive than d-d reactions to higher energy plasma ions, which reaffirms the importance of accurate measurement of the high energy ions.
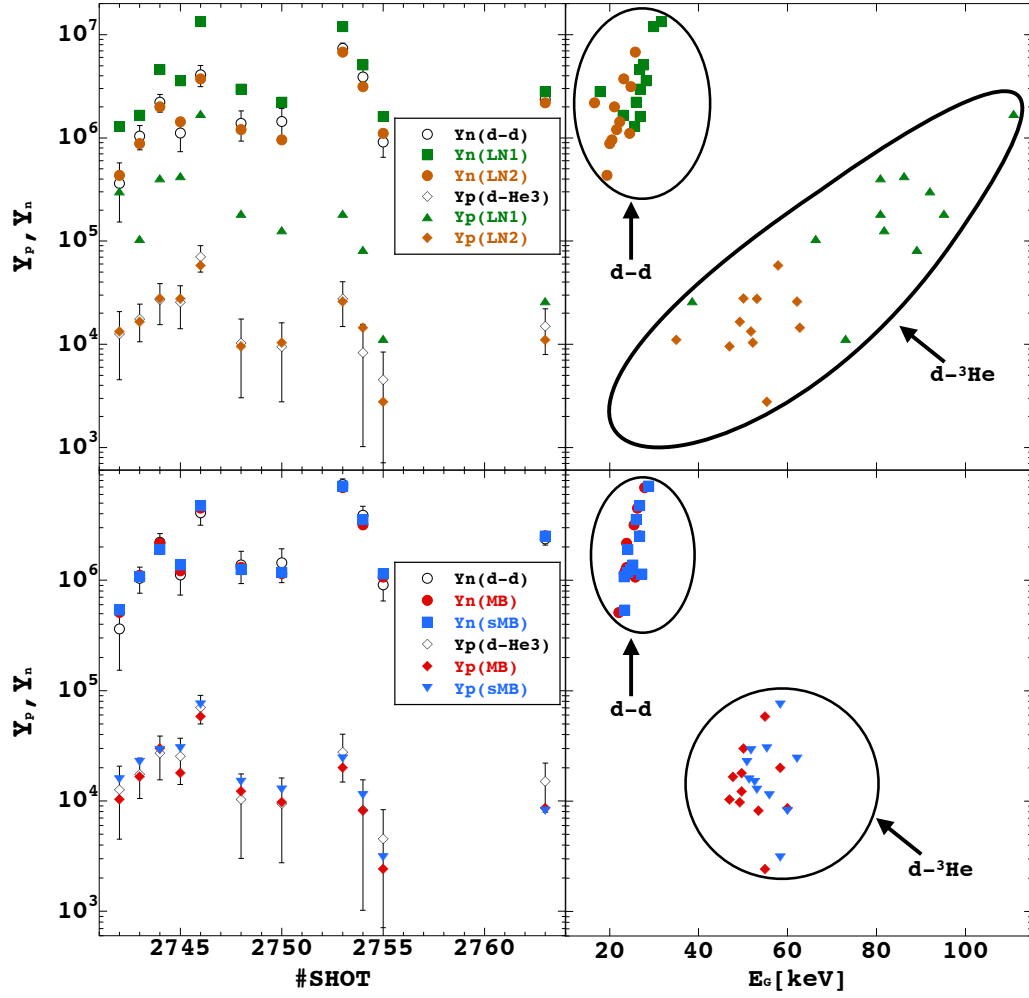
Figure 3.4: Total fusion yield obtained for d-d (Y_n) and d-^{3}He fusion reaction (Y_p). Open symbols refer to the experimentally measured fusion yields. MB and shifted MB distributions (bottom panels) all give the correct measured fusion yields within the errors. Log-normal distribution LN2 (top panels) gives the correct measured fusion yields when the parameters are chosen to reproduce d-d fusions. The log-normal distribution LN1 (top panels), which describes the ion signal correctly, does not reproduce the number of fusions measured, especially d-^{3}He which is more sensitive to the highest energies. The right panels show the estimated fusion yields as function of the Gamow energies E_G obtained for each distribution.

47

Comparing the Gamow energies for the different distributions, we find that the MB distributions give similar values, while the LN distributions give generally higher values because of the slow energy decay of the distribution. In the particular case shown in Figures 2.11 and 3.2-3.3 (i.e., shot #2754), the experimentally measured ion kinetic energy distribution spectrum and d-d fusion reaction yield are well described by the LN1 distribution (green dotted line). On the other hand, the d-^{3}He fusion yield (see Figure 3.3) we obtain with the LN1 distribution largely overestimates the data (see Figure 3.4, top panel). In general for all the other cases in Figure 3.4, the estimated number of fusions for d-d and d-^{3}He nuclear reactions using LN1 distributions are systematically higher than the measured fusion yields, above the experimental error. We can reproduce rather well both fusion yields of neutrons and protons produced with the LN2 distributions if we adjust the parameters, say to reproduce the number of d-d fusions. In such a case we do not reproduce the high momentum tail of the ion kinetic energy distribution, see Figure 2.11.

4. LASER-SOLID TARGET FUSION EXPERIMENTS

In this section we analyze the process of nuclear fusion reactions driven by laser-solid target interactions in experiments conducted at the ABC facility in ENEA, Frascati, Rome (IT) using targets of different compositions and thickness. In the framework of Coulomb explosion, in sections 4.1 and 4.2 we describe the experimental setup and particle diagnostic techniques, in section 4.3 we analyze the plasma ion kinetic energy distributions using a shifted Maxwell-Boltzmann (sMB) distribution. In sections 4.4 and 4.5 we describe the experimental apparatus used to determine the charge-to-mass ratio and the energy spectra of charged ions (i.e., Thomson parabola), and to measure the fusion yields (i.e., CR-39). These experimental tools will prove fundamental for the detection of relatively high-energy ions in the measured ion kinetic energy distributions.

4.1 The ABC Facility

The ABC facility [53, 54, 55] is in operation at ENEA-Centro Ricerche Frascati since 1988. It consists of a two-beam neodymium phosphate glass laser, capable of supplying up to 100 J/beam at the fundamental 1.054 μm wavelength and full width at half maximum (FWHM) pulse duration of about 2 ns. The experimental vacuum chamber within the facility is equipped with different types of diagnostics, see Figure 4.1. The laser-target fusion experiments at the ABC facility in ENEA were performed using the two laser beams producing a total energy $E_{LASER}\sim$100 J at a pulse duration of 3 ns, for a total power of less than 1 TW, therefore at least 3 orders of magnitude smaller than TPW. During the experiments, the two beams were focused on a thin solid target (see Figure 4.2) of different compositions and thickness (e.g., ^{10}B, ^{11}B, a mixture of CH_2+^{11}B, ^{6}LiF, ^{6}LiF+Al, ^{7}LiD and ^{79}Au),

and with a spot size r_s=25 μm which was kept constant while the laser energy might have changed shot by shot. The targets were produced at the Laboratori Nazionali del Sud and Istituto Nazionale di Fisica Nucleare, cut to the desired dimensions and installed in the chamber at the ABC laser facility. Targets thickness d_t varied from as little as 0.043 μm (^{197}Au target) to 500 μm (^{11}B target).
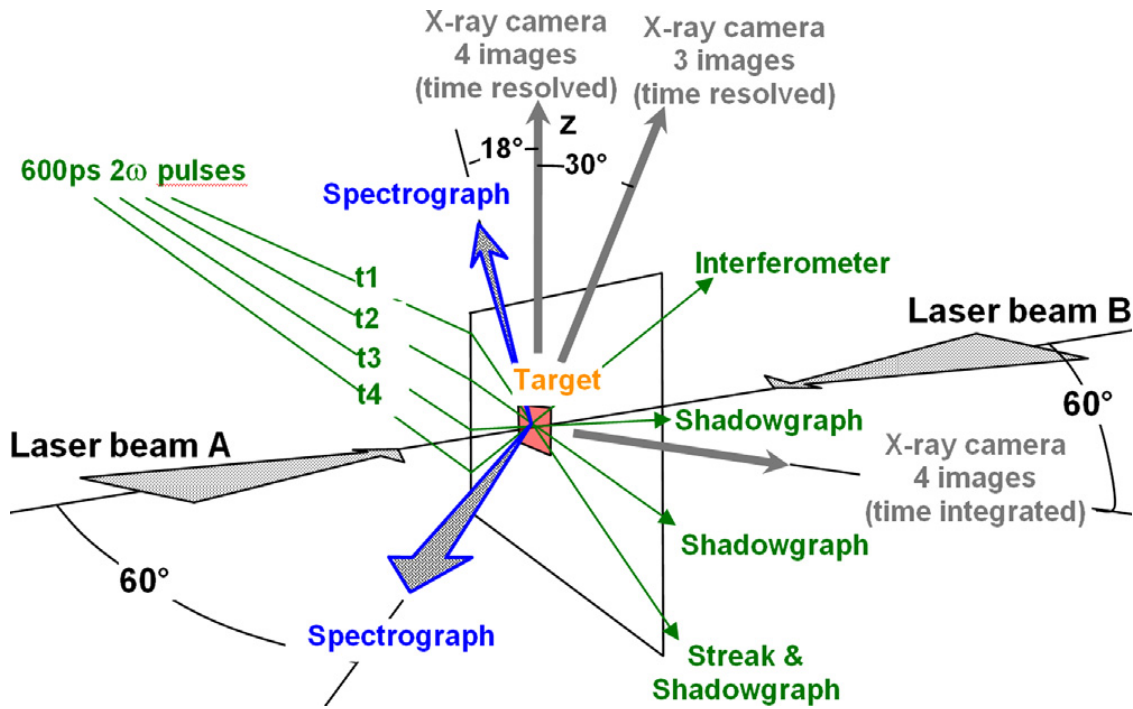
Figure 4.1: Scheme of the target irradiation by the two laser beams and of the related diagnostics in operation at the ABC facility [55].
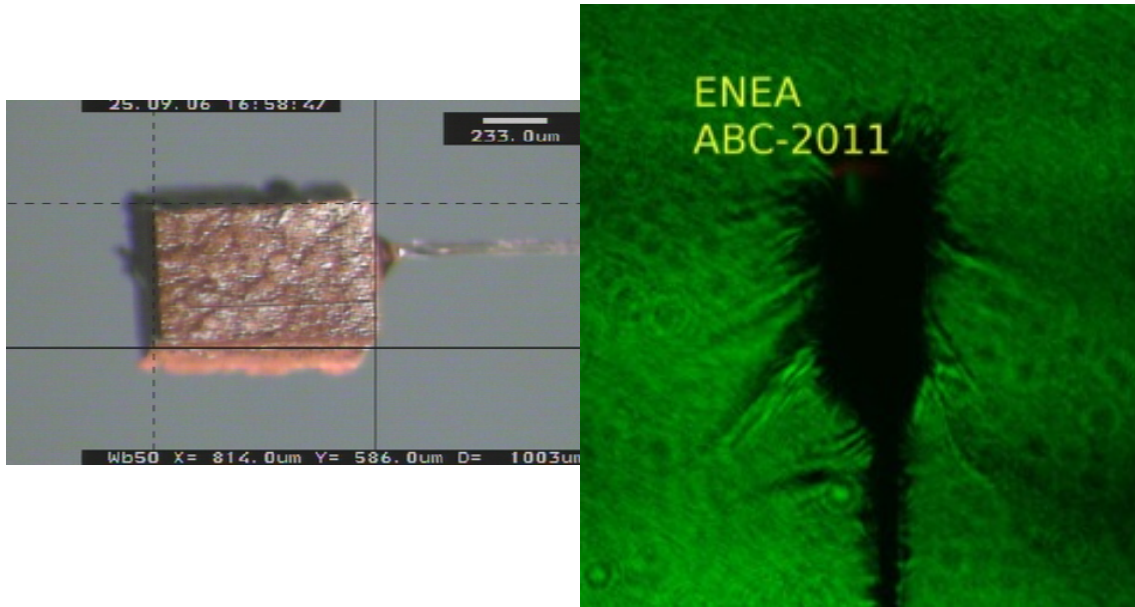
Figure 4.2: Solid target before the experiment (left) and during (right).

The plasma ions were detected using Faraday cup detectors placed at different angles and distance s relative to the target. A Thomson parabola was located at s=17.1 cm from the target as well as diamond detectors. The Thomson parabola was equipped with an image plate in the focal plane to reveal energetic ion ($>$100 keV). CR-39 plastic detectors opportunely covered with thin aluminum foils were located very close to the interaction point. These detectors are sensitive to the energetic fusion products, mainly α in our case, but not to the low energy plasma ions.

In Table 4.1, a summary of the experiments performed with corresponding laser energy measured, target employed and thickness.

Table 4.1: A summary of the experiments total laser energy, type of target and thickness. The maximum laser energy recorded was E_{LASER}=137 J compared to a minimum of E_{LASER}=50.5 J. Target thickness also varied from as big as d_t=500 μm (^{11}B target) to as little as d_t=0.043 μm (^{197}Au target).

#SHOT	E_{LASER} [J]	Target	$d_t[\mu m]$
513	100	^{11}B	500
627	137	^{11}B	300
633	130	^{11}B	300
657	132	^{11}B	350
767	108	CH_2+^{11}B	170
776	115	^{11}B	50
1023	97	^{11}B	0.4
1028	95	^{11}B	0.61
1031	85	^{11}B	0.31
1410	97	^{6}LiF	0.334
1416	84	^{6}LiF	0.334
1421	95	^{6}LiF+Al	0.334
1423	77.7	^{6}LiF+Al	0.334
1428	85	^{6}LiD	52
1433	79.7	^{6}LiD	84
1448	93.8	^{6}LiD	234
1450	82	^{197}Au	0.043
1765	50.5	CH_2+^{11}B	182
1770	55.5	^{6}LiF	0.334
1775	53	^{6}LiD	234
1781	56.7	^{10}B	0.159

4.2 Particle Diagnostics

At the present time, the ions parameters are estimated with application of various diagnostic tools. In particular, TOF spectrometry provides time resolved measurements of ion beam parameters, giving the possibility to distinguish species and charge-states, but also measure kinetic energy and total charge. In like manner, semiconductor detectors [56, 57, 58, 59], and diamond detectors which seem to improve simultaneous detection of energetic photons, electrons, and ions ejected from the reacting plasma both in forward and backward directions. At the ABC facility, Faraday cup detectors with -65 V polarization are used for particles diagnostics. In particular, eight detectors have been operating in all experiments placed at the same distance s=55 cm from the target. Later, a new Faraday cup at a further distance s=190 cm has been added, which shows clear improvements in the detection of the signal compared to the other detectors operating at the ABC facility and the one used at the TPW facility, see Figures 4.4-4.6.

In Figure 4.3, we show the typical setup of the Faraday cup apparatus employed at the ABC facility. In Table 4.2, a summary of the Faraday cup detectors operating at the ABC facility with relative angles θ, distance to the target s and diameter.
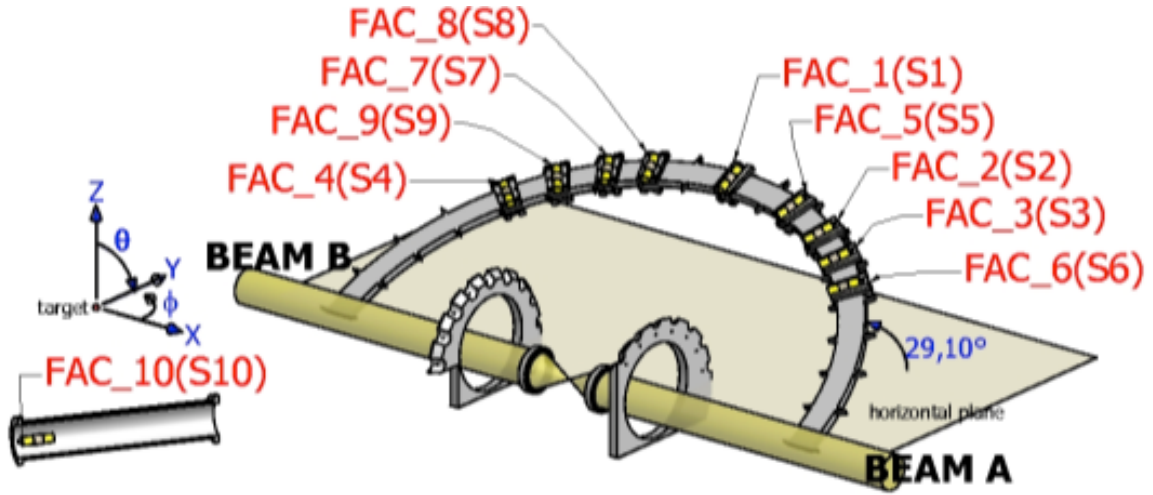
Figure 4.3: Typical setup of the Faraday cup apparatus employed at the ABC facility. The 2 laser beams can deliver up to E_{LASER}=100 J in pulses of 2ns duration. The system is suitable for irradiating planar targets up to 10^{15} W/cm^2.

Table 4.2: Faraday cup detectors operating at the ABC facility.

θ [deg]	s [mm]	diameter [mm]
43.75	551	0.1
52.75	551	0.1
61.75	551	0.1
72.75	551	0.1
108.25	551	0.1
117.25	551	0.1
127.50	551	0.1
137.75	551	0.1
65.01	1920	50

As discussed in section II, laser-plasma interaction experiments are characterized by the EMP+X-ray emission which affects the time response of all the detectors, making difficult the detection of fast particles emission. However, in recent experiments performed at the ABC facility with ^{10}B targets, the electromagnetic noise is less evident when placing the detector further from the target. Figure 4.4 shows the time space spectrum from laser-solid target interaction experiments recorded using the new detector added to the experimental apparatus and placed further from the target (i.e., s=190 cm). The structure of the measured ion signal becomes more clear when we study the ion kinetic energy moments distributions, see Figure 4.5. The improvements in the detection of the signals are more evident in comparison to the ion kinetic energy distribution measured with detectors nearer the target, see Figure 4.6. In particular, this strategy of detectors placement allows us to take a closer look at the very energetic tail of the signals where high energy plasma ions might be hidden by the EMP+X-ray emission. It is fundamental to analyze the high energy tail of the signals, since these ions are indeed the most important in the nuclear fusion process and play a primary role.
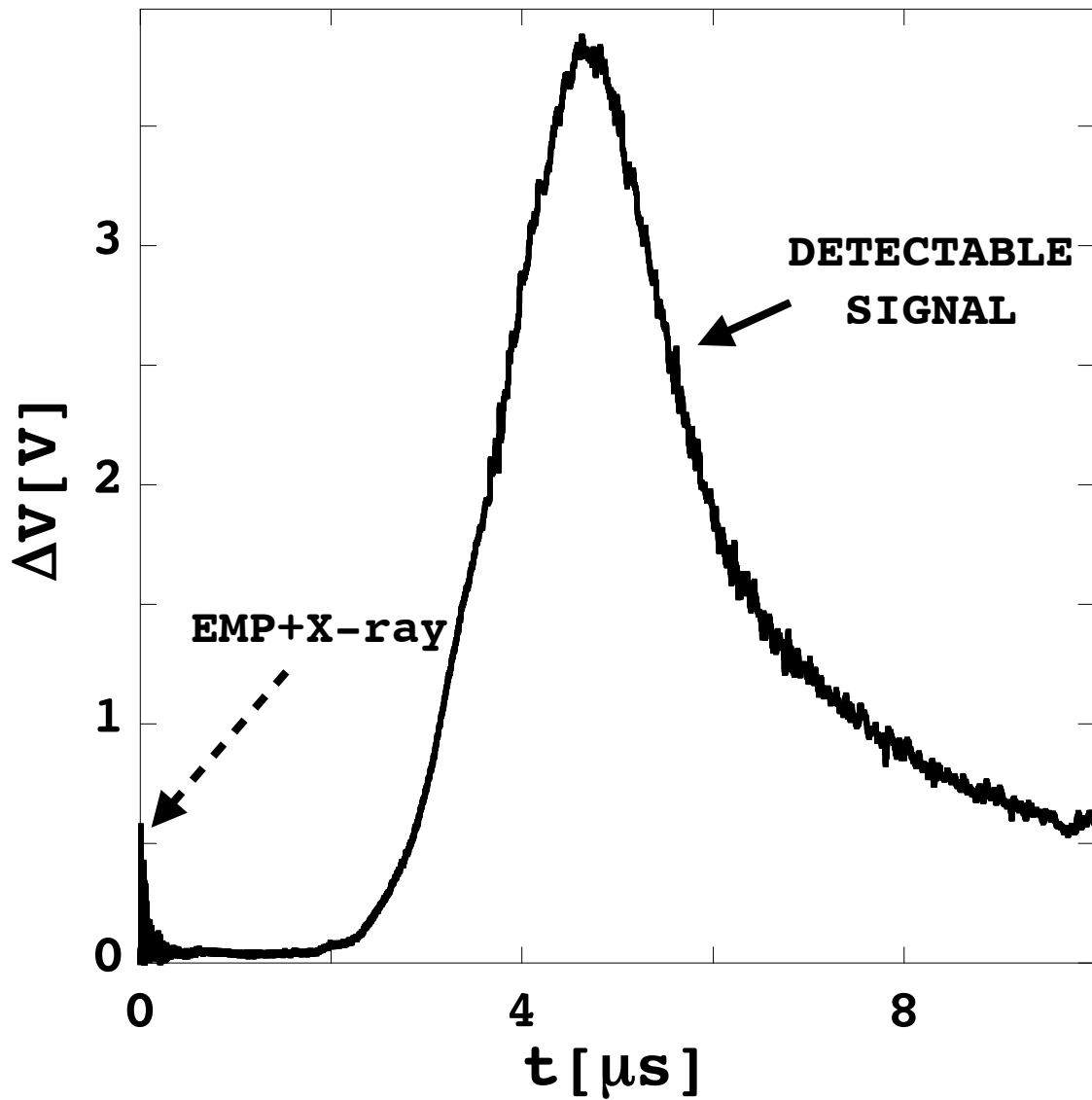
Figure 4.4: Measured ion signal from the new Faraday cup detector at distance s=190 cm from the target (^{10}B solid target). The electromagnetic noise is displaced from the ion signal when placing the detector further from the target.
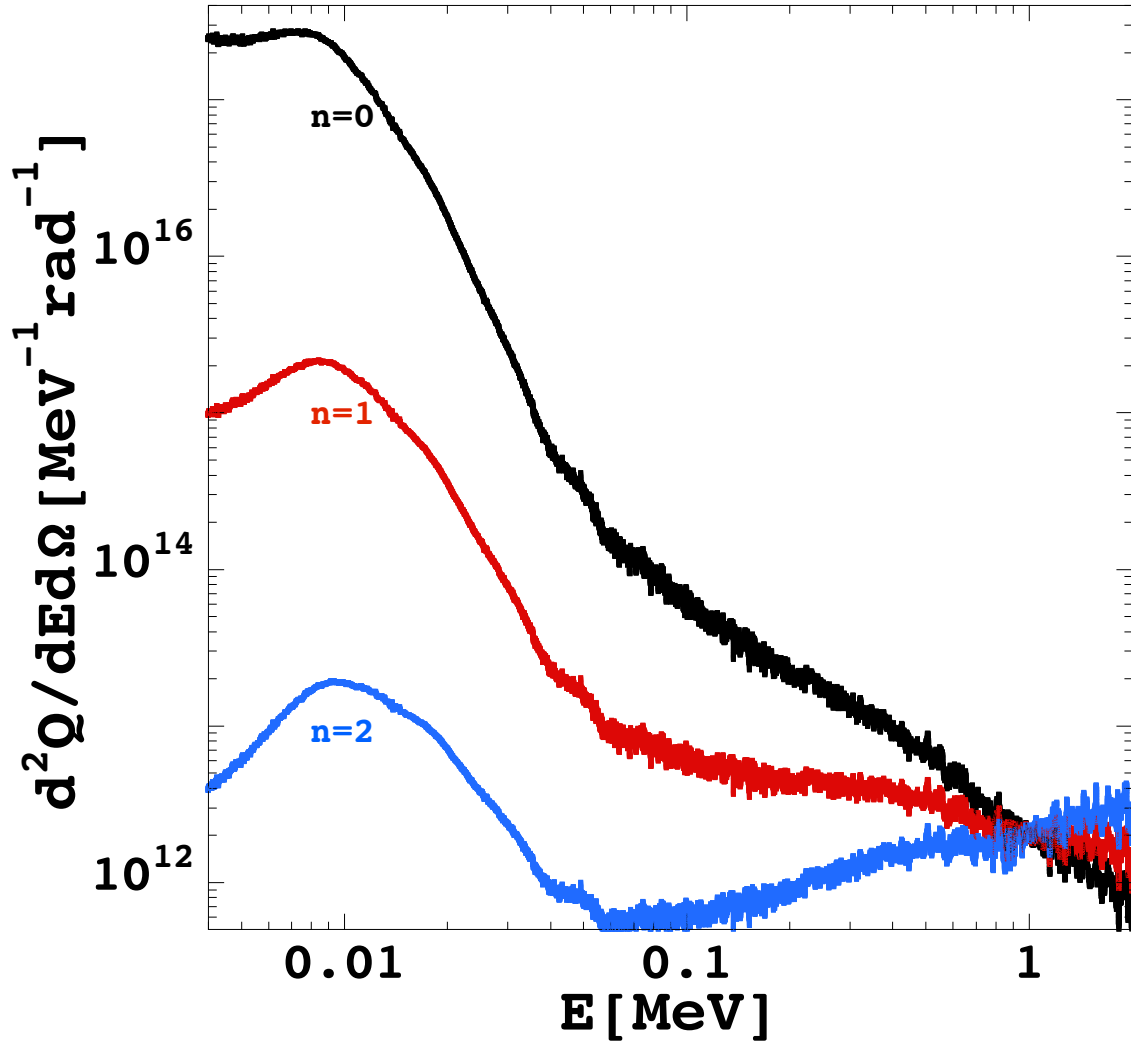
Figure 4.5: Measured ion kinetic energy moments distributions n=0 (black line), n=1 (red line) and n=2 (blue line) using the new Faraday cup detector at distance s=190 cm from the target (^{10}B solid target).
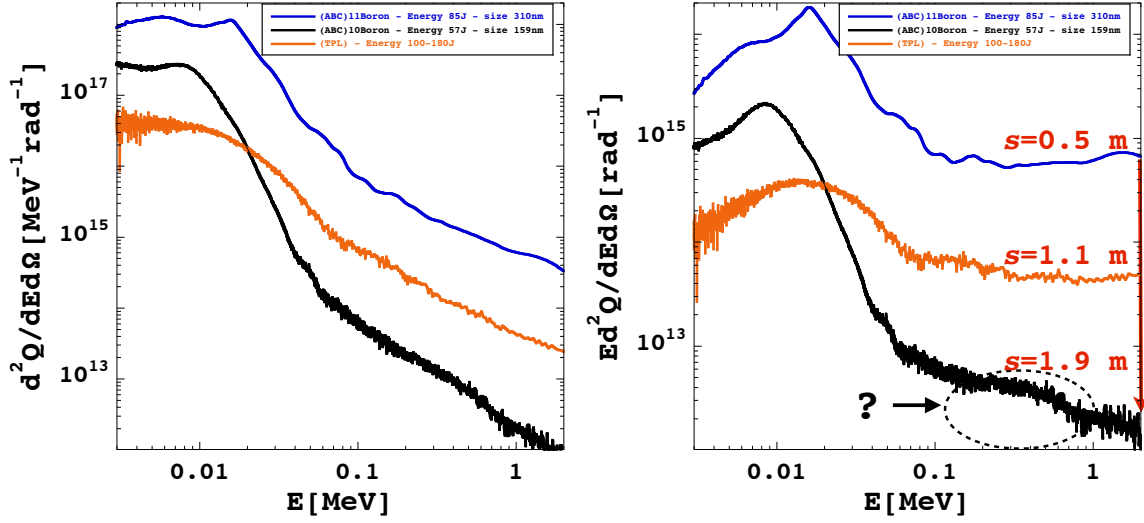
Figure 4.6: Measured ion kinetic energy distributions $n=0$ (left panel) and $n=1$ (right panel) from ^{10}B (black line) and ^{11}B (blue line) targets and D_2+^3He clusters (orange line). Signals belongs to detectors placed at different distance from the targets, $s=55$ cm (blue line), $s=107$ cm (orange line) and $s=190$ cm (black line). When the detector is located further from the target (black line), a bump around 500 keV is more visible. This area is very energetic and therefore needs to be examined very carefully to distinguish electromagnetic noise from possible detectable signal

In the following section, we proceed with the kinetic energy moments analysis of a shifted Maxwell-Boltzmann distribution function per different charge state. The new Faraday cup located at $s=190$ cm was only recently put into operation at the ABC facility. Unfortunately all the experiments that we analyze in the remainder of this thesis were performed without such a detector. It was the difficulty in analyzing the data which we discuss below which prompted us in building a new and more performing Faraday cup detector to be used in future experiments.

4.3   Plasma Ion Energy Distribution

Similarly to section 2.3 we assume ions kinetic energy distributions can be described by shifted Maxwell-Boltzmann distributions for each angle and each charge state. Assuming that all the electrons are stripped by the laser light from a target containing N positively charged ions, we introduce an energy shift $E \to E - E_C$ in the distribution function, due to the Coulomb repulsion [19, 20, 21, 23, 24, 25, 26, 27, 28, 29, 30, 31, 32, 33, 34, 35, 36]. Particles features like temperature and collective energy can be obtained from the kinetic energy moments distributions analysis. We can extract indeed temperature and collective energy for each charge state by studying the energy moments of the corresponding shifted Maxwell-Boltzmann distribution. The width of this distribution can be associated with a local temperature T (T<<E_C). The number of produced ions and their kinetic energies depend on the laser energy and pulse duration. In general, the experimental ion kinetic energy distribution measured displays structures which can be due to different charge states of the ions involved. In this analysis, we will assume that during the laser-target interactions, the most energetic ions are produced first and therefore the higher charge states are first emitted (i.e., high energy tail corresponds to the highest charge state of plasma). The higher energy regions are then assigned to the highest charge state. Eventually the plasma cools down and lower energy ions of lower charge state appear. As discussed in section II, when trying to highlight the ions regions in the signal, the different charge states of the system can be better found by multiplying the ion kinetic energy energy distribution by E^n (i.e., n=0,1,2,3,4,5,6,7,8). This way, we want to highlight those structures belonging to different charge states of the ions. Hence for each charge state that we are able to individuate and assign, we plot the maxima as function of the order n and derive the values T and E_C from Eqs. (2.9)

and (2.11). Thus we can write a shifted Maxwell-Boltzmann distribution $\frac{d^2Q_{MB}}{dEd\Omega}$ for each charge state and build the charge state probability $\Pi(q)$ as

$$\Pi(q) = \frac{\frac{d^2Q_{MB}}{dEd\Omega}(q, E)}{\sum_q \frac{d^2Q_{MB}}{dEd\Omega}(q, E)}. \tag{4.1}$$

Then, the kinetic energy distribution for each charge state q is given by

$$\frac{d^2N}{dEd\Omega}(q) = \frac{1}{q}\frac{d^2Q}{dEd\Omega}\Pi(q), \tag{4.2}$$

and the measured ion kinetic energy distribution can be described by summing all charge states kinetic energy distributions as

$$\frac{d^2N}{dEd\Omega} = \sum_q \frac{d^2N}{dEd\Omega}(q). \tag{4.3}$$

In Figure 4.7, we show an example of kinetic energy moments distributions analysis using a shifted Maxwell-Boltzmann distribution via Eqs. (2.9) and (2.11) for charge states $q=3$ and $q=5$ of ^{6}Li and ^{11}B, respectively.
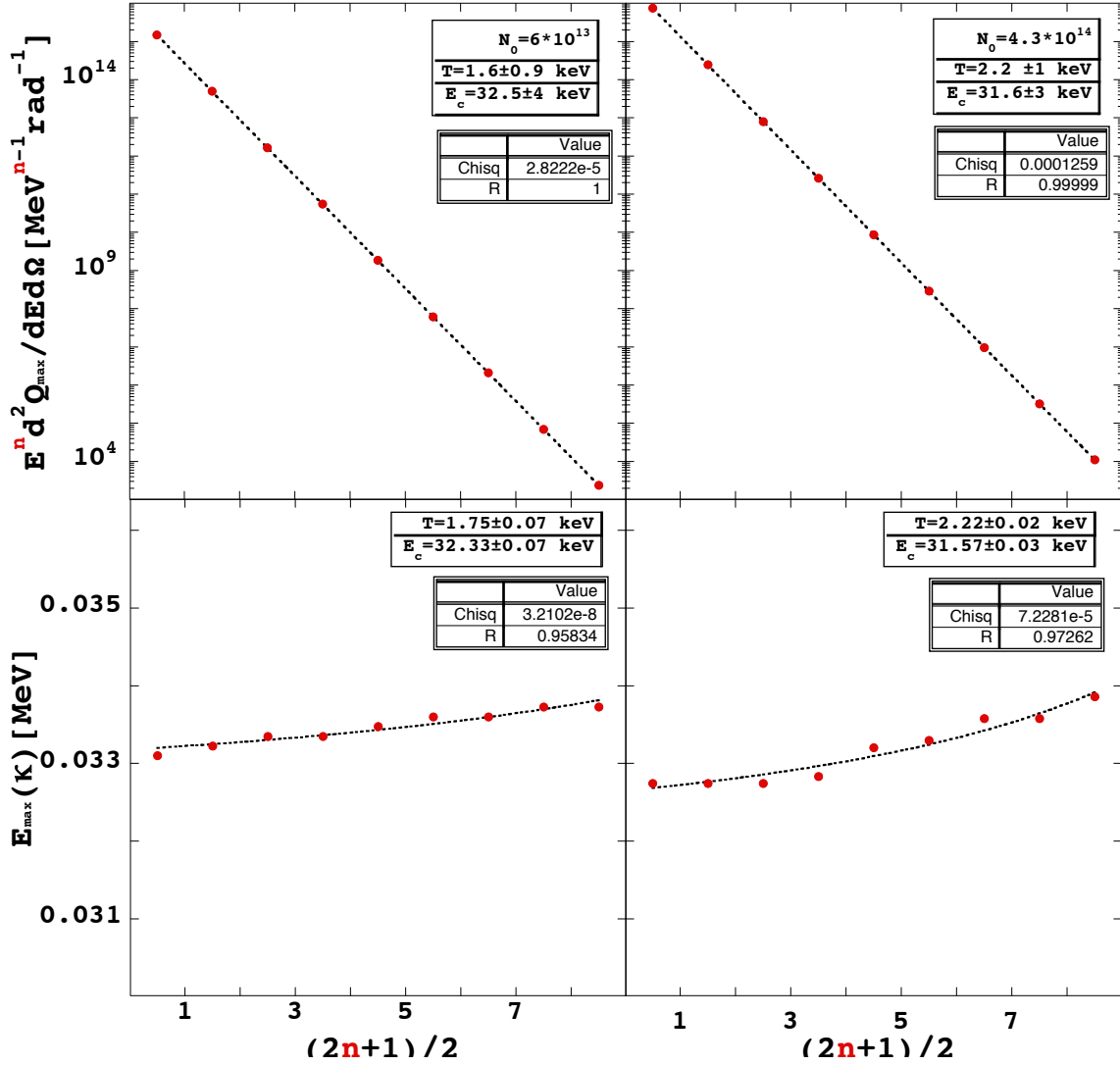
Figure 4.7: Kinetic energy moments distributions analysis from ^{6}Li charge state $q=3$ (left) and ^{11}B charge state $q=5$ (right) for a shifted Maxwell-Boltzmann distribution via Eqs. (2.9) (bottom figures) and (2.11) (top figures). The two extrapolations are well in agreement and the difference can be used to estimate the error. Temperatures and collective energies for the highest charge state of both ^{6}Li and ^{11}B are comparable.

We stress the fact that we have guessed the charge state of the ion assuming that the highest charge states are the most energetic ones. In Figure 4.8, the shifted Maxwell-Boltzmann distribution $\frac{d^2Q_{MB}}{dEd\Omega}$ for each charge state of ^{6}Li and ^{11}B are obtained from the extrapolated data via kinetic energy moments distributions analysis. The kinetic energy distributions (n=0,1) are displayed, and sharper peaks at higher plasma ion kinetic energies can be observed. In Figure 4.9, we compare the measured ion kinetic energy distributions (black line) with the ones estimated via Eq. (4.3) (red line) taking into account the probability of each charge state. We also plot the ion kinetic energy distributions obtained via Eq. (2.6) for n=0 by taking into account only the highest charge state (i.e., q=3 for ^{6}Li and q=5 for ^{11}B). These two overlap in the high energy region, showing indeed that it is the highest charge states which participate most in the fusion reaction process. The measured ion kinetic energy distributions change widely with the detection angle being mostly focused along the laser directions. This suggest a completely out of equilibrium plasma moving along the laser direction. Furthermore, by conveniently decreasing the laser energy on one side, we can easily understand where the ions are originated from. In particular, we detect a larger amount of produced ions in the same direction of the laser with larger energy and when detectors are located closer to the laser beam direction (i.e., θ <60° and θ >130°, see Table 4.2). This confirms the colliding beam-beam scenario. In Figure 4.10, we plot the average number of particles $\langle N \rangle$ obtained via Eq. (2.7) considering charge state q=3 vs each detector's angle θ from three different laser-solid target interaction experiments on ^{6}Li system. Although the target thickness was kept constant (i.e., d_t=334 nm), the total laser energy varied during each shot, having one side always more energetic than the other one. In Figures 4.11-4.13, we consider experiments performed with similar target thickness on two different systems (i.e., d_t=334 nm for ^{6}Li target, d_t=310 nm for ^{11}B target). The averaging has

been performed over different shots and angles. In particular, both collective energy and temperature increase with higher charge states and in general, the collective energies contributions are higher than those of temperatures. In Figure 4.11, we plot $\langle E_C/E_{LASER} \rangle$ vs $(q_{max}\text{-}q)/q$ and $\langle T/E_{LASER} \rangle$ vs $(q_{max}\text{-}q)/q$ for ^{6}Li and ^{11}B targets obtained from the ion kinetic energy moments distributions analysis. In Figures 4.12 we compare average charge state temperature $\langle T \rangle$ vs $\langle E_C \rangle$ average charge state collective energy and $\langle T \rangle$ vs $\langle E_C \rangle /A$ average charge state collective energy per mass number A. In Figure 4.13 we plot the average charge state number of ions $\langle N \rangle$ vs $(q_{max}\text{-}q)/q$. The results show an increase of average charge state temperature and average charge state collective energy with increasingly charge state as expected. Furthermore, the average charge state collective energy is much larger than the average charge state temperature, indicating a quite narrow distribution of the ions for each charge state. We showed that using the values of T and E_C obtained from the kinetic energy moments distributions analysis we could describe the measured ion kinetic energy distributions quite well for each case following Eqs. (2.6) and (4.3). Even though the shifted Maxwellian distributions are unable to completely reproduce the experimental results to the finest detail, they strongly support our scenario. The largest failures of the fits are for very energetic ions where the measured ion signal might overlap with noise. A typical example is also shown in Figure 4.9 where a component is observed at high energies. We did not try to reproduce this part since it is not clear if it is ion signal or noise. However, it is of crucial importance to understand if a very energetic and out of equilibrium component is produced since we know that for instance fusion reactions are very sensitive to those components. One way to test such high momentum tail is to use Thomson Parabola.
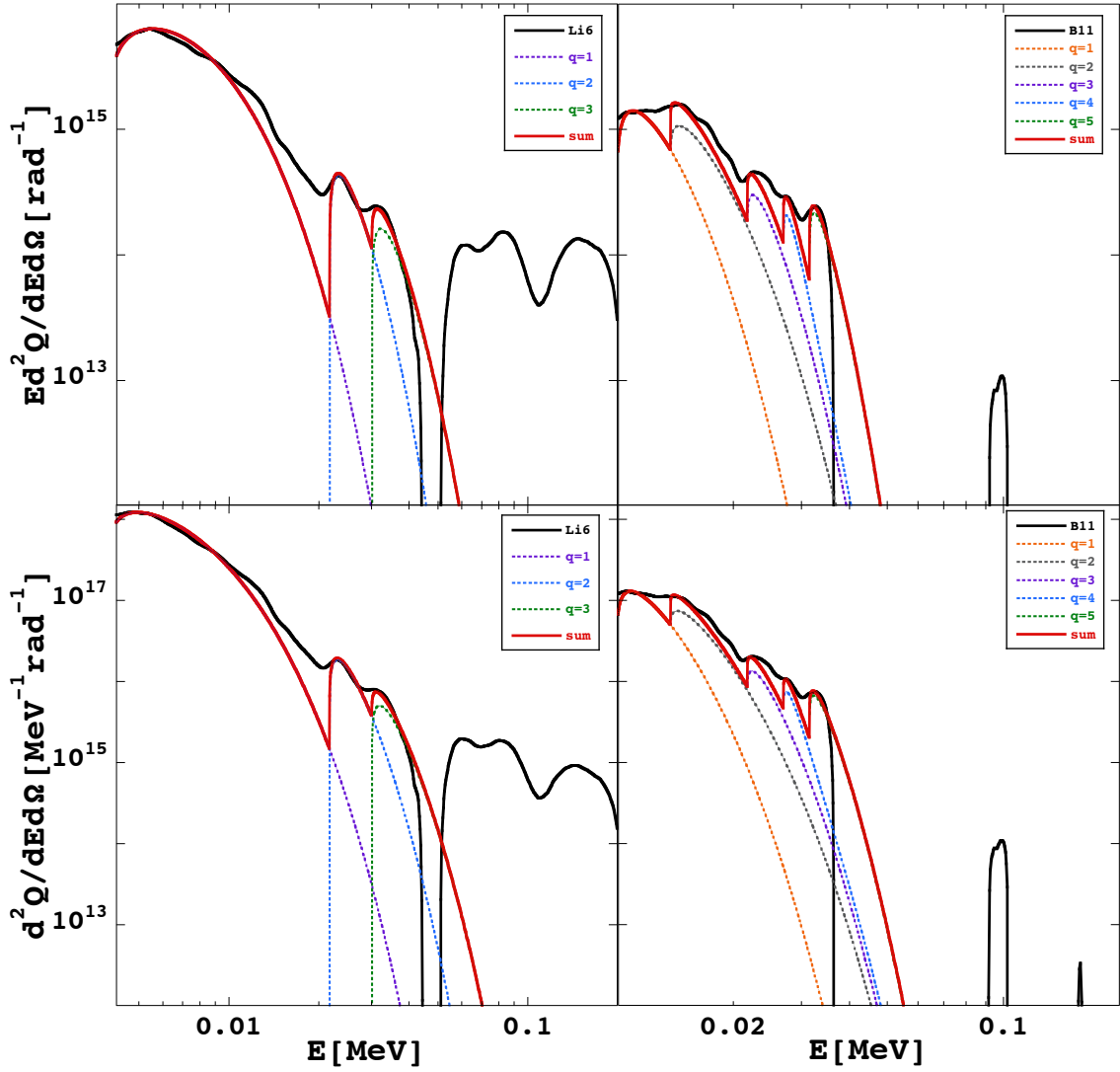
Figure 4.8: Measured ion kinetic energy distributions $n=0,1$ (black lines) for ^{6}Li (left panel) and ^{11}B (right panel). Shifted Maxwell-Boltzmann distributions $\frac{d^2 Q_{MB}}{dEd\Omega}$ (dotted lines) are obtained via energy moments analysis from the temperature and collective energy extracted for each charge state. In red, the sum of all charge state shifted Maxwell-Boltzmann distributions.
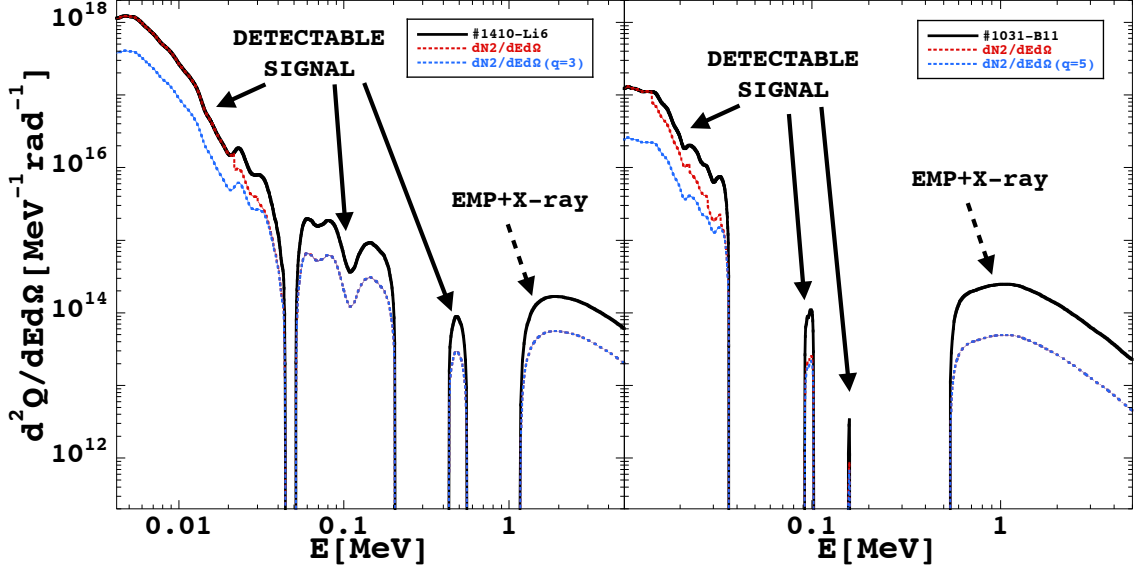
Figure 4.9: Measured ion kinetic energy distributions $n=0$ (black lines) for ^{6}Li (left panel) and ^{11}B (right panel) compared to the estimated ion kinetic energy distributions via Eq. 4.3 (red dotted lines) taking into account all charge states contributions and compared to the ion kinetic energy distributions obtained via Eq. (2.6) for $n=0$ and the highest charge state only (i.e., $q=3$ for ^{6}Li and $q=5$ for ^{11}B, blue dotted lines).
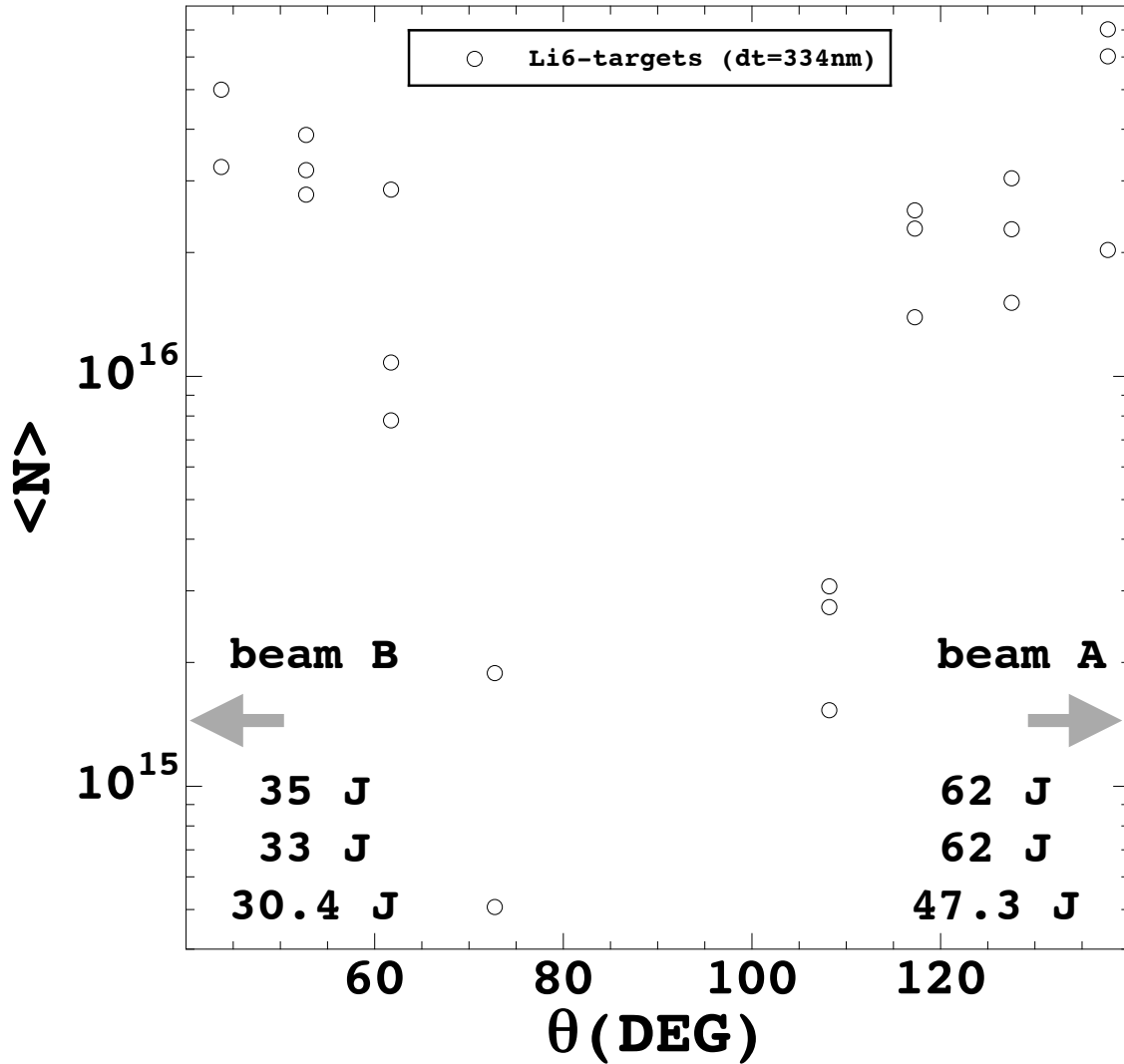
Figure 4.10: Average number of particles $\langle N \rangle$ considering charge state $q{=}3$ estimated via Eq. (2.7) vs detector's angle θ. During the three laser-target interaction experiments on ^{6}Li system, the target thickness was kept constant (i.e., $d_t{=}334$ nm), but the total laser energy varied with one side always more energetic than the other one. A larger amount of ions are detected in the same direction of the laser with larger energy and at angles closer to the laser beam direction (i.e., $\theta <60°$ and $\theta >130°$, see Table 4.2).
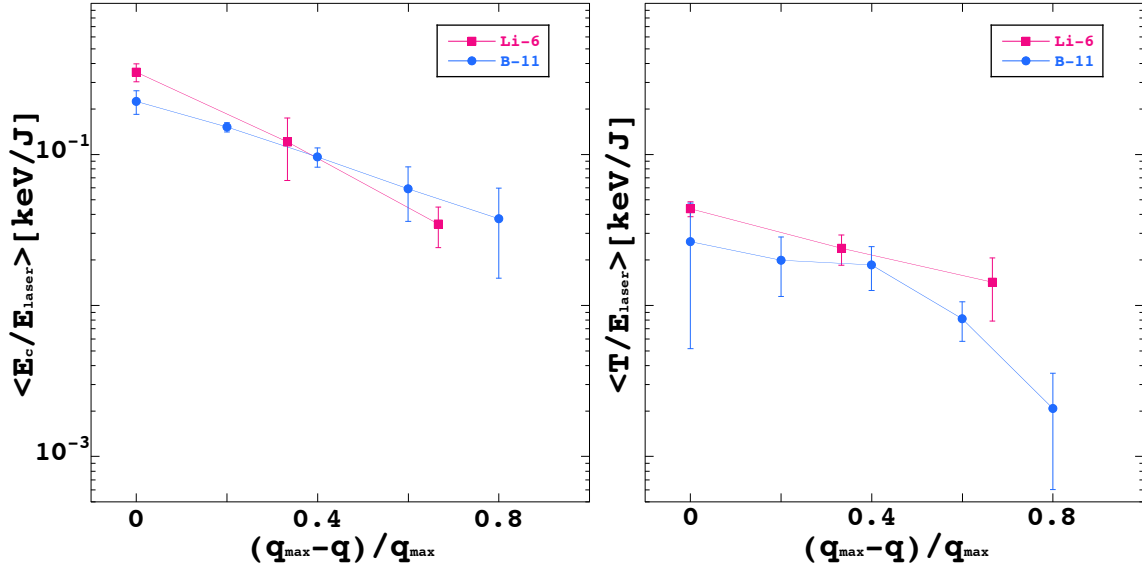
Figure 4.11: Average charge state collective energy E_C (left panel) and charge state temperature T (right panel) divided the total laser energy E_{LASER} measured vs $(q_{max}\text{-}q)/q$ for ^{6}Li and ^{11}B systems (i.e., q_{max}=3 for ^{6}Li and q_{max}=5 for ^{11}B). The extrapolation suggests that collective energy and temperature increase with higher charge states and that the collective energies estimates are higher than the temperatures.
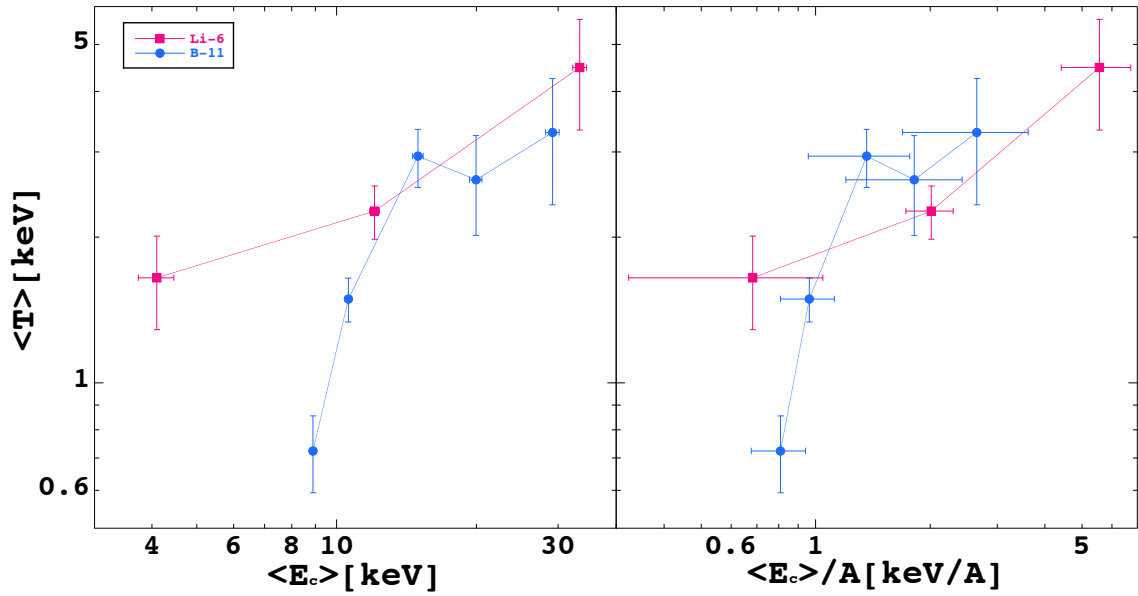
Figure 4.12: Average charge state temperature $\langle T \rangle$ vs $\langle E_C \rangle$ average charge state collective energy (left panel) and $\langle T \rangle$ vs $\langle E_C \rangle / A$ average charge state collective energy per mass number (right panel) for ^{6}Li and ^{11}B systems (i.e., A=6 for ^{6}Li and A=11 for ^{11}B).
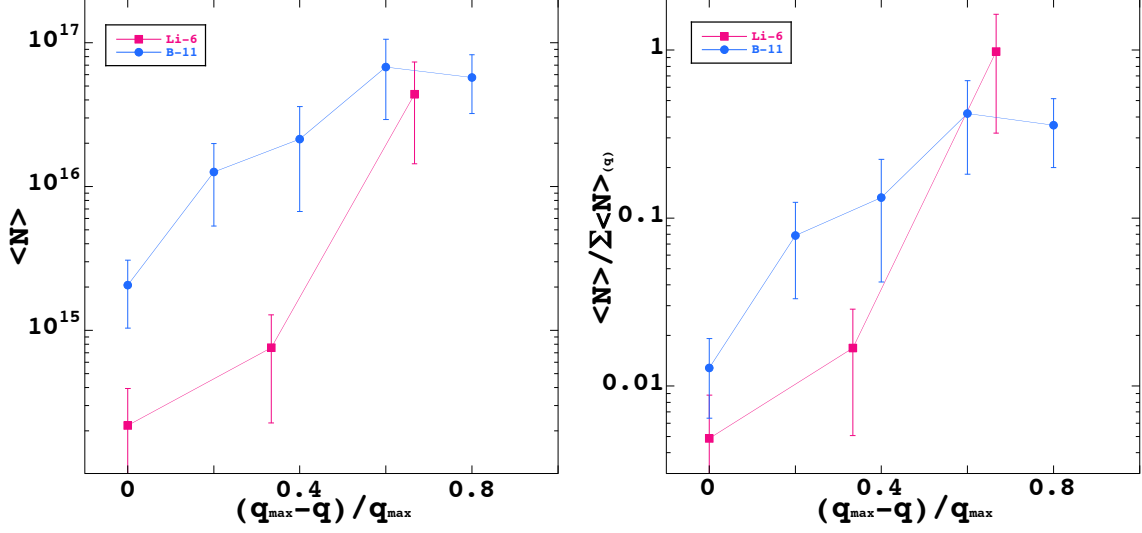
Figure 4.13: Average charge state number of ions $\langle N \rangle$ vs $(q_{max}\text{-}q)/q$ (left panel) and average number of ions per charge state divided by the total number of ions summing all charge states contributions $\langle N \rangle / \sum \langle N \rangle_{(q)}$ vs $(q_{max}\text{-}q)/q$ (right panel) for ^{6}Li and ^{11}B systems (i.e., $q_{max}=3$ for ^{6}Li and $q_{max}=5$ for ^{11}B). The extrapolation suggests that the number of ions per charge state increases with lower charge states.

4.4   Thomson Parabola

Although, we are unable to investigate the highest (non-equilibrium plasma) ion kinetic energies since the experimental signal overlaps with the (small) EMP, a Thomson parabola can reveal the existence of such high energy ions. We have shown that such high momenta are present when we used the new Faraday cup located further away from the target. The Thomson parabola ion spectrometer (TPIS) is a device used to measure the charge-to-mass ratio and the energy spectra of charged ions. This device has found applications in studying the acceleration of ions by ultra-intense lasers [60, 61, 62, 63, 64]. In a TPIS, parallel magnetic and electric fields are used

to deflect ions of a given charge-to-mass ratio onto unique parabolic curves at the detector plane. Two different types of Thomson parabolas prototypes [65] were built for the ABC facility [54, 55]. In Figure (4.14) the scheme related to the parabola, and the two defined configurations. The small available space within the experimental chamber required their size optimization. Magnetic B and electric fields E up to 2 kG and a few kV can be supplied, respectively, for detection of ions with energies up to some tens of keV. The parallel magnetostatic and electrostatic fields within the parabola lead each particle to intercept the detector at its x- and z-coordinates. From the knowledge of these positions at the detector plane it is therefore possible to determine the particle velocity and charge-to-mass ratio. Each discrete value of B/E present will produce a unique parabolic trace with the highest energies closest to the origin x = z = 0. These deflections are proportional to the charge to momentum and charge to energy ratios. The principle of operation of a Thomson parabola analyzer is also shown in Figure 4.14.

Assuming collinear homogeneous electric field E and magnetic field B, the coordinates for the deflection of a charged particle with a given mass number A, atomic number Z and velocity v on a screen at the distance L_d are given by

$$x = \frac{Ze}{Amv}BL(\frac{L}{2} + L_d). \tag{4.4}$$

$$z = \frac{Ze}{Amv^2}EL(\frac{L}{2} + L_d). \tag{4.5}$$

In the above, EL and BL are the products of the magnitude and length of electric and magnetic fields, respectively. Ions of equal charge-to-mass ratios thus trace a parabola in the detection plane, with the distance from the origin (defined by geometrical projection of the plasma through the pinhole onto the screen) corresponding

to a particular velocity, given by

$$v = \frac{z}{x}\frac{B}{E}. \tag{4.6}$$

Once calibrated, the position of the ions on the detector plane can be used to determine the ion energy. The number of ions detected at each position can be used to determine the ion energy spectrum.
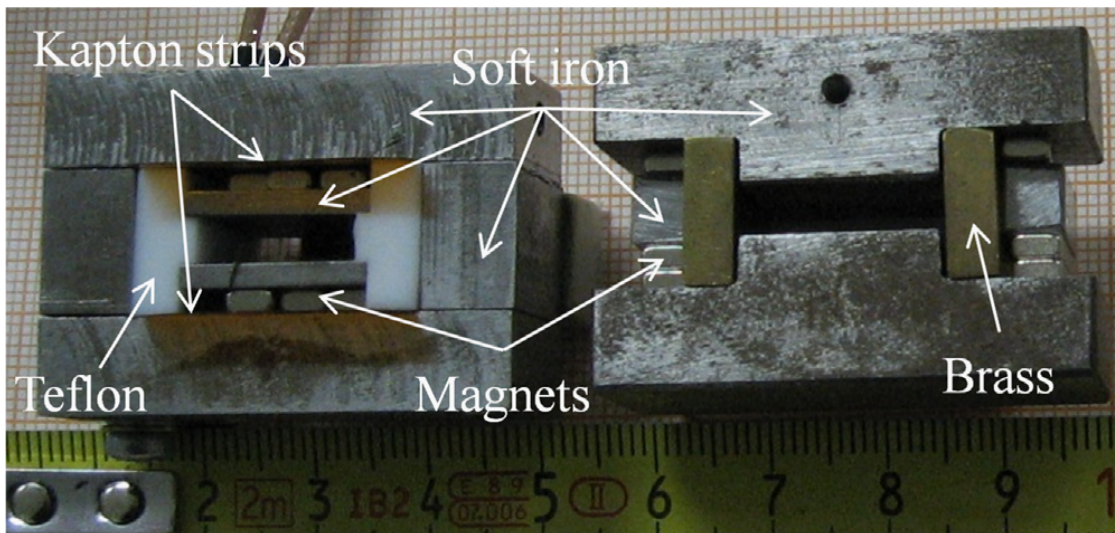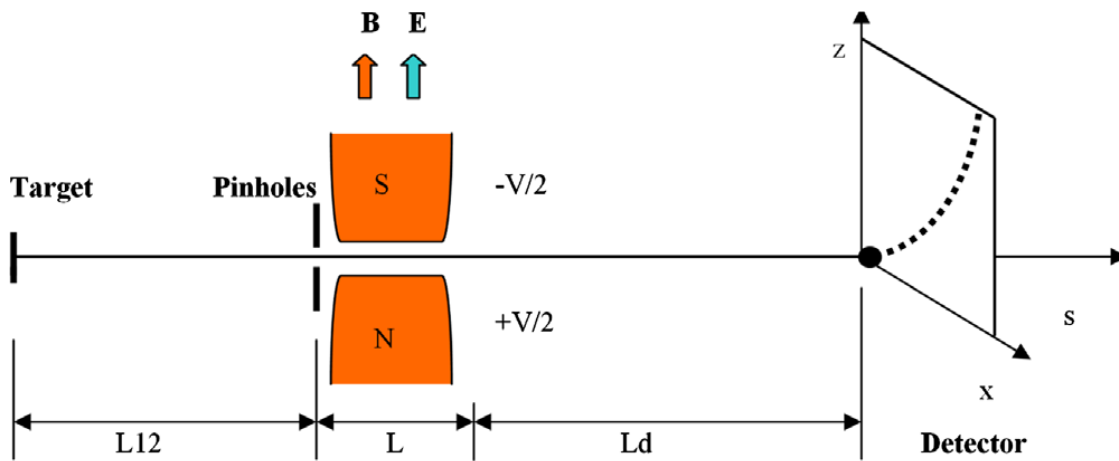
Figure 4.14: Thomson parabola scheme of detection and two different configurations [55].
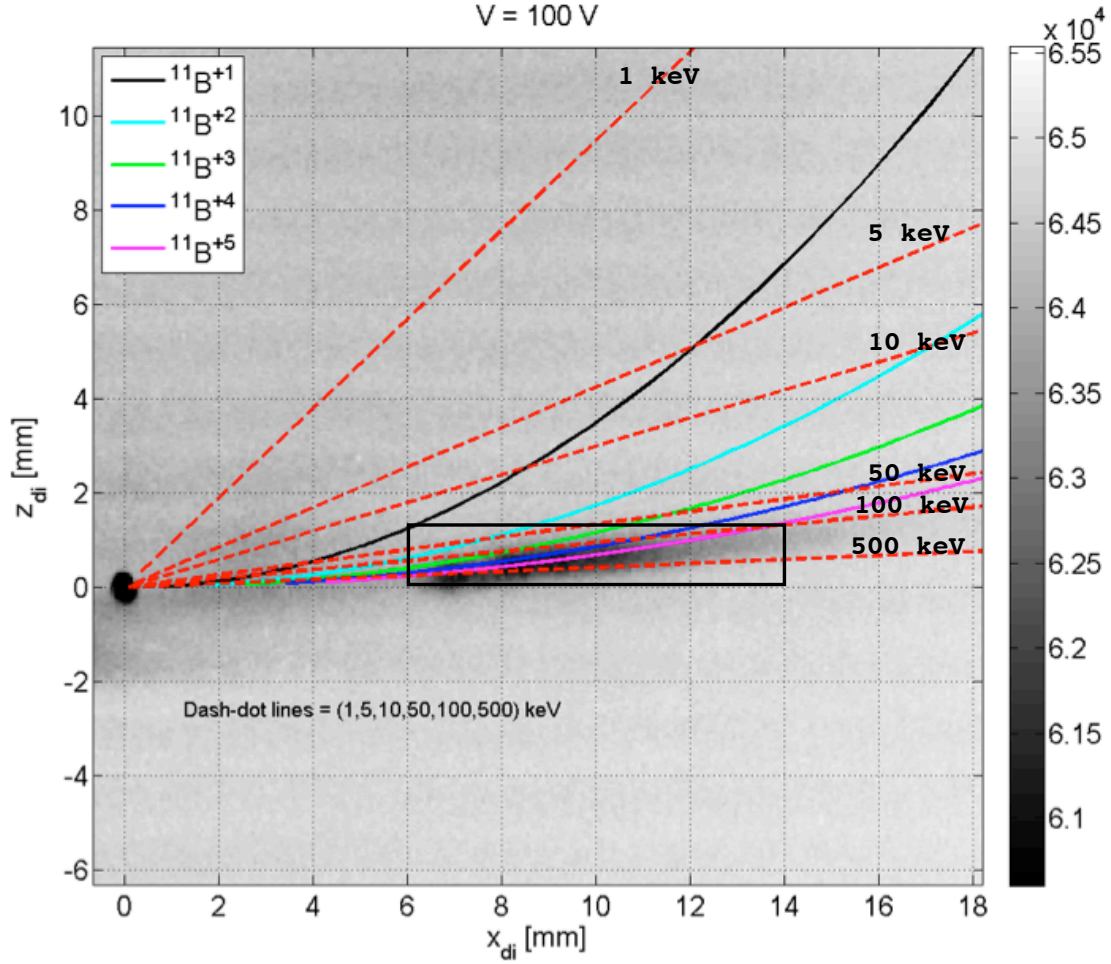
Figure 4.15: Ion tracks recorded with an image plate located on the focal plane of a Thomson parabola. The tracks referring to ^{11}B ions of kinetic energy larger than 100 keV are clearly visible.

During the experiments, the Thomson parabola revealed ^{11}B ions of charge states $q=4$ and $q=5$ between 100 and 500 keV, see Figure 4.15. Last in this section, we describe the CR-39 plastic detectors used for fusion yields measurements. These detectors are sensitive to the energetic fusion products, which in these experiments

consisted mainly of α particles.

4.5   CR-39

CR-39 (see Fig. 4.16) are used as neutron spectrometers at the OMEGA laser facility [66] as well at the NIF for diagnosing neutrons and charged particles from ICF implosions. The ABC experimental chamber is equipped with a structure of support for CR-39 plastic track detectors (see Figure 4.16) [67] to detect the α particles [68, 69, 70, 71] produced and measure the fusion reactions yields $Y_{\alpha(CR-39)}$ in Table 4.3. The latent tracks are made visible by etching the CR-39 in a 6 N NaOH at 80°C for 6 hours. During this procedure, conical pits are created along the particle tracks because the damaged plastic along the track has a higher etch rate than the undamaged plastic [72]. Etched CR-39 detectors are scanned under an optical microscope using the charged particle spectroscopy (CPS) program developed by Massimo Calamosca of the ENEA-Bologna. The CPS program uses the pit eccentricity, diameter and resulting contrast to calculate an energy spectrum of the particles ejected during the implosion as well as the areal density of the target to quantify the success of the reaction [73]. However, defects in the bulk of the plastic created during the CR-39 manufacturing process can compromise the data and the subsequent CPS analysis. In Figure 4.18, a typical situation where some flaws (background noise) in the CR-39 image under an optical microscope have diameters comparable to the pits created along particle tracks (detected track).

Figure 4.16: CR-39 plastic track detector.
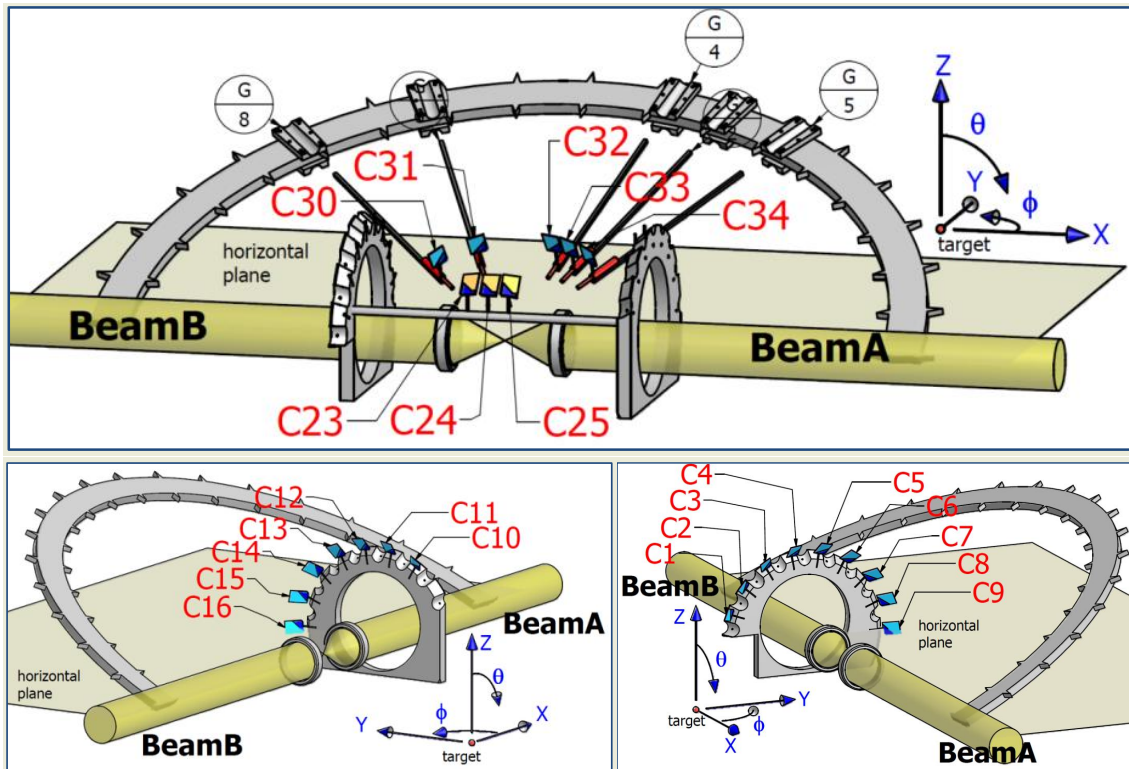
Figure 4.17: Scheme of the CR-39 diagnostic.
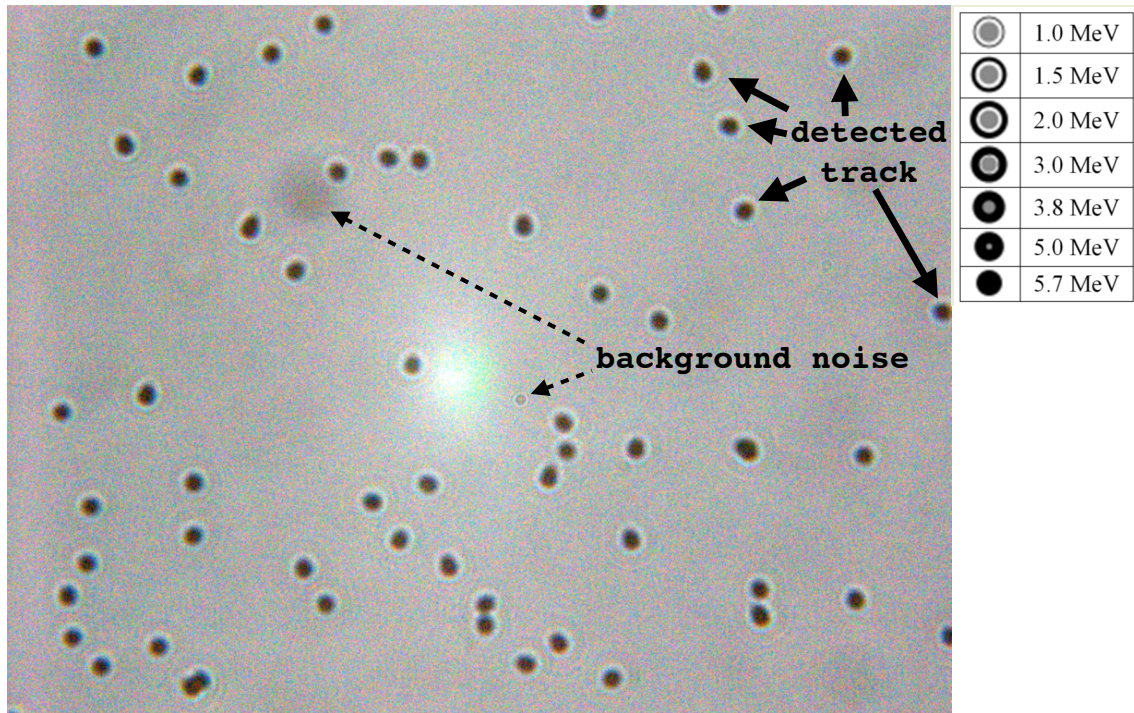
Figure 4.18: CR-39 image under an optical microscope after standard etching. The defect pit appears similar to the valid pit and would be identified as a valid one by the CPS program.

At the ABC facility, CR-39 detectors were etched after irradiation during 6-12 h in a solution of NaOH in H_2O at 70°. Having realized that standard pattern tools were unfit to reduce the background to the required very low level, a new score has been devised, by combining both Normalized Cross-Correlation and Zero-mean Normalized Cross-Correlation indexed [74, 75, 76]. More details on this analysis can be found in the appendix (see Appendix B).

The α energy distribution obtained in Table 4.3 from the p-[11]B and [6]Li-[6]Li nuclear reactions are quite different because of the large difference in Q-values. In fact, in the [6]Li-[6]Li nuclear reaction a large number of relatively small tracks indicating α

energies larger than 10 MeV are observed. These tracks are not observed in the p-^{11}B nuclear reaction, or in not irradiated targets (background). When the experiment was originally planned, we expected a small yield for the ^{6}Li-^{6}Li nuclear reaction. Thus we decided to use the same CR-39 detectors for consecutive shots, later on we repeated the experiment using a different set of CR-39 detectors. Because we kept CR-39 detectors for consecutive shots on ^{6}Li system, the ^{6}Li-^{6}Li yield is averaged over 3 shots. In an analogous manner, in order to calculate fusion reactions yield using Eq. (5.3), we will average the fusion yields for the same three shots. In the table below the detailed fusion yields $Y_{\alpha(CR-39)}$ measured from each fusion reaction system. Recall that for p-^{11}B and ^{6}Li-^{6}Li nuclear reactions, three alpha particles are produced in each fusion reaction. Therefore, the fusion reactions yields quantities $Y_{\alpha(CR-39)}$ refer to the number of fusion events and not the number of alphas produced.

Table 4.3: Measured fusion reactions yields $Y_{\alpha(CR-39)}$ at the ABC with Q-value of the nuclear reaction, target thickness d_t employed and total laser energy E_{LASER}. For ^{6}Li-^{6}Li nuclear reactions experiments, the laser energies and the fusion yields have been averaged over the three shots. The measured fusion yields $Y_{\alpha(CR-39)}$ error corresponds to the 26% of the value for p-^{11}B reaction, while for ^{6}Li-^{6}Li nuclear reaction the error has been calculated from the average over 3 shots.

Reaction	Q [MeV]	d_t [μm]	E_{LASER} [J]	$Y_{\alpha(CR-39)} \times 10^5$
p-^{11}B $\rightarrow 3\alpha$	8.59	170	108	3.3($\pm$0.9)
^{6}Li-^{6}Li $\rightarrow 3\alpha$	20.81	0.334	90	3.0(+5.2-2.6)

The importance of the high momentum tail of the measured ion signal is confirmed by the large fusion yields measured, especially, in the ^{6}Li-^{6}Li nuclear reaction. This

result and the Thomson parabola analysis are complementary to the Faraday cups measurements and confirm the production of relatively high-energy ions. In the following section, we will estimate the fusion reaction yields using the measured ion distributions signals rather than the parametrization, in order to be able to add high momenta which cannot be properly fitted and include the ion component (very small but substantial) with kinetic energies of the order of 500 keV.

5. FUSION REACTIONS

In this section we discuss several experimental results obtained with ICF systems. In sections 3.1 and 3.2 we measure the fusion reactions yields produced in the experiments performed with $CH_2+^{11}B$ and ^6LiF targets at the ABC, Frascati, Italy. We estimate the fusion cross sections and reaction rates produced in the nuclear reactions p-^{11}B and ^{6}Li-^{6}Li, including only the highest charge states (i.e., $q=5$ for ^{11}B and $q=3$ for ^{6}Li) in the analysis of the ion kinetic energy distributions. For the first time we measure ^{6}Li-^{6}Li fusion reaction rates at about 500 keV Gamow energy, and we confirm the experimental S-factor for the p-^{11}B system as well. We also estimate possible d-t reaction rates and compare the results obtained in different laboratories with different targets (i.e., NIF and Omega).

In our analysis, we assumed that the intense laser fields extracts the electrons from the targets causing the ions to follow the electrons along the laser beams in two opposite directions in a sort of beam-beam collision. We will estimate the probability of fusion via Eq. (1.8) in the limit where the plasma disassembly time can be approximated by the average target crossing time and estimated as

$$\tau_{ABC} = \frac{d_t}{v}. \tag{5.1}$$

In the equation above, d_t is the thickness of the target and v is the speed of the ions. This formula holds for the cases where the target thickness is very small, or when the target is completely destroyed by the laser. Alternatively one should consider the range of the ion plasma in the (thick) target.

5.1 $^{11}\mathrm{B}(\mathrm{p},\alpha)^8\mathrm{Be}$

The p-^{11}B nuclear reaction experiment was performed using as target a mixture of CH$_2$+^{11}B of thickness d_t=170 μm. The total laser energy measured was E_{LASER}=108 J. We estimated the fusion yield of the nuclear reaction $^{11}\mathrm{B}(\mathrm{p},\alpha)^8\mathrm{Be}$ as

$$Y_\alpha = c_p c_{11B} N_i \rho_{(CH_2+^{11}B)} \langle\sigma\rangle_{p^{11}B} \, d_t. \tag{5.2}$$

In the equation above, c_p=0.07 and c_{11B}=0.4 are the concentration of protons and ^{11}B ions in the target, respectively, N_i is the total number of energetic ions in the plasma, $\rho_{(CH_2+^{11}B)}$ is the average atomic number density of the target, $\langle\sigma\rangle_{p^{11}B}$ is the average fusion cross section between p and ^{11}B. Including carbon ions and taking into account the ion concentrations, the average charge $q^\star$ and the average mass $m^\star$ for the CH$_2$+^{11}B target case give $q^\star$=5.1 and $m^\star$=10.61 u. In our estimates, the average cross section is calculated numerically via Eq. (1.6) from the experimentally measured ion kinetic energy distributions (Eq. (2.6) for n=0, $q{\to}q^\star$, $m{\to}m^\star$) using the well known S-factor of the reaction p-^{11}B [9]. Alternatively assuming a constant S-factor, we can make an estimate of S using the measured ion kinetic energy distribution and the fusion yield Y$_{\alpha(CR-39)}$ for p-^{11}B nuclear reaction by inverting Eq. (5.2).

5.2 $^6\mathrm{Li}(^6\mathrm{Li},\alpha)^8\mathrm{Be}$

The ^{6}Li-^{6}Li nuclear reaction experiments were performed using ^{6}LiF targets of thickness d_t=334 nm. The total laser energies measured were 97 J, 95 J and 77.7 J for each shot respectively, see Table 5.1. We estimated the alphas fusion yield of the nuclear reaction $^6\mathrm{Li}(^6\mathrm{Li},\alpha)^8\mathrm{Be}$ as

$$Y^\alpha = \frac{N_{^6Li}\rho_{^6LiF} \langle\sigma\rangle_{^6Li^6Li} \, d_t}{2}. \tag{5.3}$$

In the equation above, $N_{^6Li}$ is the total number of energetic lithium ions in the plasma, $\rho_{^6LiF}$ is the average atomic number density of the target, $\langle \sigma \rangle_{^6Li^6Li}$ is the average fusion cross section between lithium ions. In our estimates, the average fusion cross section is calculated numerically via Eq. (1.6) from the experimentally measured ion kinetic energy distributions (Eq. (2.6) for $n=0$, $q=3$) assuming a constant $S=8.5$ GeV b extracted from [7, 8]. Also inverting Eq. (5.3) for a constant S, we can make our estimate of the S-factor from the measured ion kinetic energy distribution and the fusion yield $Y_{\alpha(CR-39)}$ for ^{6}Li-^{6}Li nuclear reaction.

Again, recall that for p-^{11}B and ^{6}Li-^{6}Li nuclear reactions, three alpha particles are produced in each fusion reaction. Therefore, the fusion reactions yields quantities Y_α and Y^α refer to the number of fusion events and not the number of alphas produced. In order to reproduce the measured fusion yield for ^{6}Li-^{6}Li nuclear reaction, we need to include the high momentum tails of the distribution which, as we have discussed before, overlaps with the initial noise due to the EMP. However, as we have pointed out in section IV, TP analysis shows the presence of ions at high energy, as well as preliminary results with the improved Faraday cup located at further distance from the target. Thus, we estimate the fusion yield via Eq. (5.3) including every component of the experimentally measured ion kinetic energy distributions and calculate the corresponding total energy $\langle E \rangle$ carried by the plasma ions. This quantity divided by the measured laser energy E_{LASER} represents the energy transfer efficiency from the lasers to the plasma ions and should be less than 1. When including the high momentum part of the distribution, we obtain a good reproduction of the fusion yields measured from the CR-39 detectors. In Figure 5.1, to reproduce the ^{6}Li-^{6}Li result we need to increase the S-factor to 155(+266-111) GeV b, which thus represents our estimate for this quantity at a Gamow energy $E_G=476\pm100$ keV. This is higher than the value $S=8.5$ GeV b obtained at center of mass beam energy

$E_{c.m.}$=1.05 MeV in accelerator experiments [7, 8]. This could indicate the presence of a resonance. The ^{12}C energy spectrum displays large width resonances at 28.2 MeV and 28.83 MeV excitation energies. Those resonances might increase the S-factor as reported in Figure 5.1. In the fusion yield for p-^{11}B nuclear reaction, the quoted experimental error is just statistical due to the CR-39 tracks counting. From our analysis and inverting Eq. (5.2) for a constant S, we derived the value of S=248±67 MeV b at the Gamow energy E_G=42±3 keV, below a strong and narrow resonance in ^{12}C located at 16.106 MeV excitation energy. Our S-factor value (full circle in Figure 5.1) is in good agreement within the error bars with literature [3, 4, 5, 6], see also Figure 1.2.

In Figure 5.2, we report the product of the fusion yields times the corresponding Q-value of the reaction in order to compare different cases. This is the total fusion energy obtained in the process and we have divided it by the corresponding total laser energy E_{LASER}. Thus in terms of energy gains, this is the first approximation of the efficiency of the process: energy might be produced when this ratio is larger than one. In addition, the ICF process has been studied intensively in many other laboratories, especially at Omega and NIF. Fusion data are available in the literature and we have reported them also in Figure 5.5. The goal of this figure is to compare reactions with high Q-value and no production of neutrons with more commonly studied reactions where neutrons are produced such as in d-d or d-t. As we see from the figure, the best result is obtained for the ^{6}Li-^{6}Li nuclear reaction case but it is eight orders or magnitude below efficiency 1. The reasons why we obtain a larger efficiency for ^{6}Li-^{6}Li and not for the p-^{11}B nuclear reaction case is the larger Q-value and the higher ^{6}Li concentration in the targets (i.e., higher reactions probability). The experimental result reported by Belyaev *et al.* [77] and corrected by Kimura *et al.* [78] using laser of picoseconds pulse duration which produces MeV plasma ions

is also included. Together with the results reported by Labaune *et al.* [79] using a two lasers, two targets geometry. Since in these cases [77, 79], the energy efficiency conversion from laser to ion kinetic energy is not known to us, the experimental results have been arbitrarily located along the X-axis in Figures 5.2-5.4. However, the situation becomes most favorable to long pulse lasers if we utilize low Z systems, such as d-d or d-t, which give high cross sections for low plasma kinetic energies, of the order of tens of keV. Even though we cannot perform such experiments at the ABC laser facility because of radioprotection requirements, we can estimate the fusion yields from our measured plasma ion velocity distributions. In fact, our targets made of $CH_2+^{11}B$ should give very similar results to solid targets made of CDT (i.e., a plastic containing deuterium and tritium ions instead of hydrogen). Then, using the measured ion velocity distributions with $CH_2+^{11}B$ target (i.e., correct concentrations, reduced mass and charge state) and the experimentally available *S*-factor for the d-t nuclear reaction, we can estimate fusion yield of the reaction. The result is plotted in the Figure 5.2 (open cross), and it is three orders of magnitude above the highest result obtained with laser-solid targets interaction reported in [79]. The TPW laser fusion reactions yields estimates for d-t system are calculated from the TPW experiments analyzed throughout this work assuming clusters concentration 50:50 of D and T. For NIF and Omega results, we assumed an average ion kinetic energy $E=\frac{3}{2}NT$, where T is the measured temperature, $N=\rho V$ is the number of particles, ρ the known target density and V its volume [80, 81, 82, 83, 84, 85, 86, 87, 88, 89]. NIF uses an indirect drive method [80, 81, 82, 83, 84, 85], while at Omega direct drive injection is used with spherical symmetry [86, 87, 88, 89]. However, the direct drive approach at Omega seems to give a better efficiency than NIF but the latter results are improving with time and experience. Our method is more similar to the Omega case, even though we assume cylindrical symmetry and describe a completely

out of equilibrium system in contrast with the attempts made at NIF and Omega to create compressed and nearly in equilibrium plasmas. We expect our approach to be competitive with those methods and an experimental verification at Omega, NIF or LMJ facility under construction in France would be very interesting and challenging. However, from these results, the idea of a power plant based on aneutronic nuclear reaction seems very unlikely. At the present time, we are very far indeed from reaching the efficiencies obtained via deuterium-tritium fusion reaction.

The same graph but as function of ρR_f, where ρ is the fuel density and R_f is the fuel radius, is given in Figure 5.3. This parameter is of critical important for ICF. Ignition and self-sustaining burn occur when plasma self-heating exceeds all energy loss mechanism [90]. Therefore the measurable burn-averaged ρR_f (in g/cm^2) and ion temperature T_i (in keV) necessary to achieve ignition is given by [90]

$$\rho R_f (\frac{T_i}{4.4})^{2.2} > 1. \tag{5.4}$$

As a matter of fact, high ρR_f and plasma temperature are basic requirements to achieve ignition. In the ABC experiments, ρ is the average target density and R_f corresponds to the target thickness d_t. Again, since in [77, 79], the relationship ρR_f is not known to us, the experimental results have been arbitrarily located along the X-axis. In the TPW experiments, ρ is the average density of the cluster plume and R_f=2.5 mm for d-^{3}He nuclear reaction, while R_f=l+0.5(R-l) on average for d-d nuclear reaction.
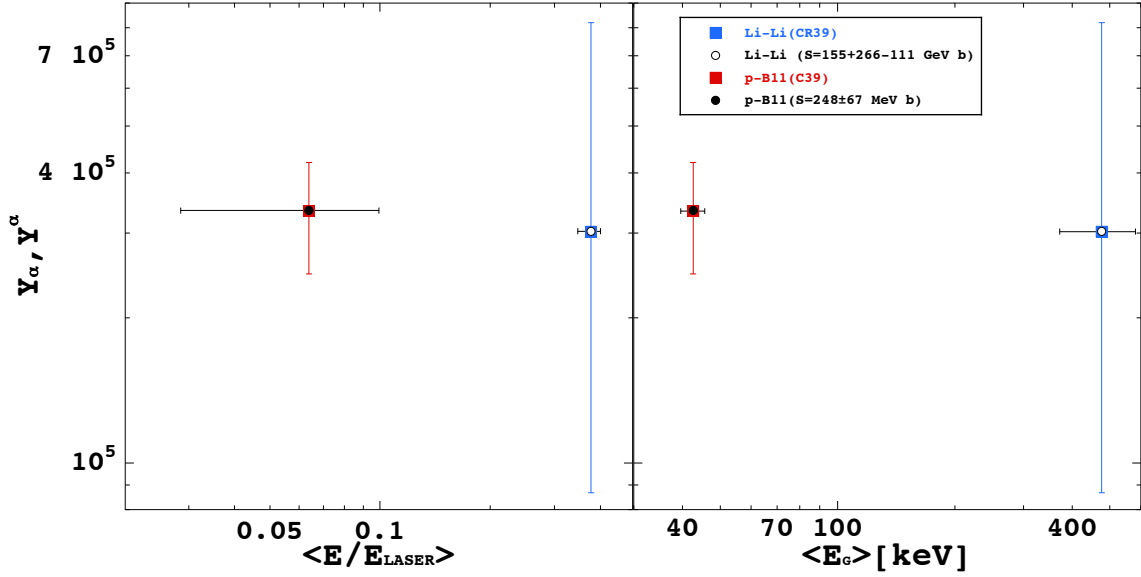
Figure 5.1: Estimated average fusion yields Y_α for p-^{11}B (full) and Y^α for ^{6}Li-^{6}Li (open) nuclear reactions as function of the average energy efficiency $\langle E/E_{LASER} \rangle$ (left panel) and average Gamow energy E_G (right panel). Experimentally measured fusion yields $Y_{\alpha(CR-39)}$ and errors for p-^{11}B nuclear reaction (red) and ^{6}Li-^{6}Li nuclear reaction (blue) are also plotted. The S-factor for ^{6}Li-^{6}Li has been estimated from [7, 8] and adjusted to reproduce the data. The errors on the X-axis quantities has been estimated as the difference between the total average and the averages values obtained from detectors on side A and B. For the experiment performed on CH$_2$+^{11}B, this difference was found to be the same as expected since the two laser beams had almost equal energies. The measured fusion yields $Y_{\alpha(CR-39)}$ error corresponds to the 26% of the value for p-^{11}B reaction, while for ^{6}Li-^{6}Li nuclear reaction the error has been calculated from the average over 3 shots.
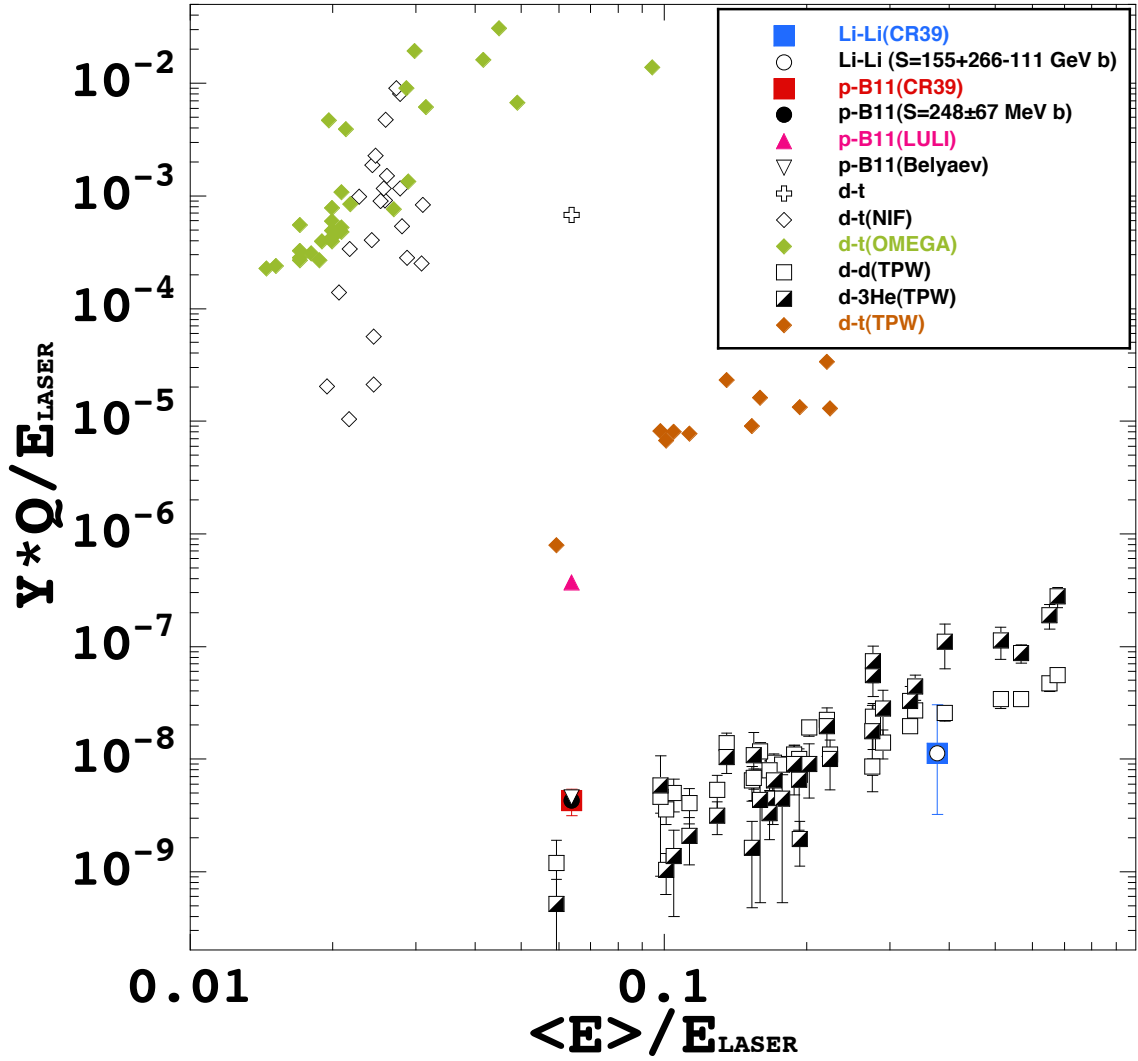
Figure 5.2: Fusion yield Y times Q-value of the nuclear reaction divided by total laser energy E_{LASER} vs the energy efficiency $\langle E/E_{LASER} \rangle$ obtained. NIF (open diamonds) and Omega (green diamonds) results are also reported. The d-t system (open cross) has been calculated assuming CDT target from the measured ion signal obtained with $CH_2+^{11}B$ target. The fusion reaction rates measured with TPW are plotted (squares) considering clusters concentration 50:50 of D and ^{3}He for d-^{3}He nuclear reaction. Our estimates for d-t system at the TPW are also reported (orange diamonds).
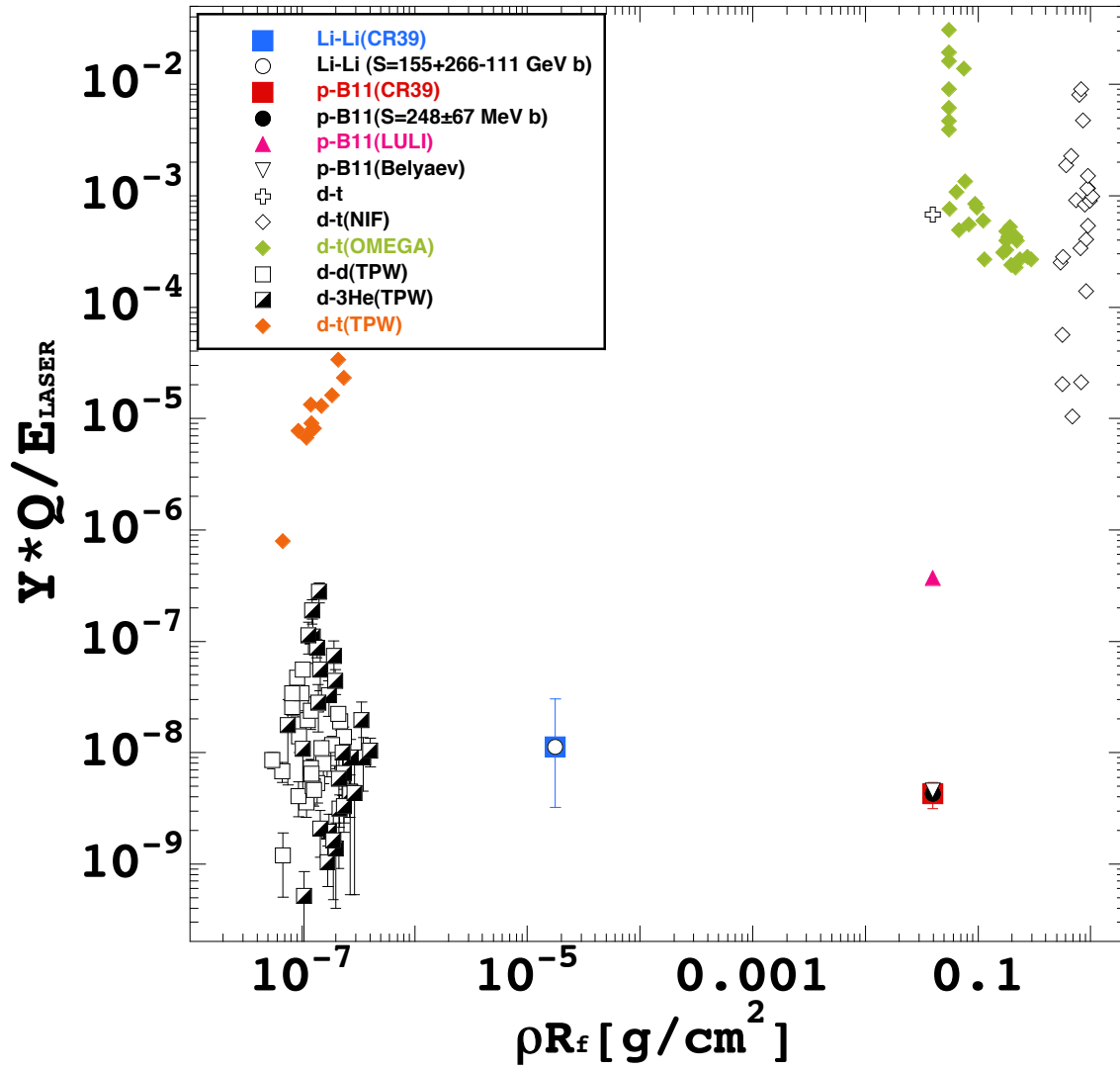
Figure 5.3: Same as Figure 5.2 vs ρR_f.

6. CONCLUSIONS

In sections II and III of this work we have explored the motion of ions emitted from Coulomb explosions in a laser-driven fusion reaction process. We analyzed the process of fusion reaction driven by laser-cluster interaction in experiments conducted at the Texas Petawatt laser facility using a mixture of D_2+^3He and CD_4+^3He cluster targets. In the framework of cluster Coulomb explosions, we analyzed the energy distributions of the ions using a Maxwell-Boltzmann (MB) distribution, a shifted MB distribution (sMB) and a log-normal (LN) distribution and calculated the fusion particles yields for each distribution from d-d and d-^{3}He fusion reactions. We have shown that the first two distributions reproduce well the experimentally measured ion kinetic energy distributions and both fusion yields of neutrons and protons produced, offering a situation in which the ion distribution can be considered as in thermal equilibrium with or without a negative collective energy. On the shots considered, we have observed an average deuterium ion kinetic energy of 12.9±2 keV, or kT=8.6±2 keV defined as two thirds of the average kinetic energy of deuterium ions, compared to an average deuterium ion kinetic energy of 14.3±2 keV, kT=9.5±2 keV and E_C=-10.9±0.3 keV using shifted MB distributions. In contrast, the LN distribution is not able to reproduce all the experimental data with the same set of parameters. In fact, we were able to derive the correct fusion yields, but in this case the log-normal distribution is not a very well correct representation of the high energy plasma ions. However, as pointed out in Ref. [39], the measured deuterium cluster sizes are far smaller than the average sizes calculated using the Hagena parameter [91, 92] which might have affected the cluster size distribution itself, and therefore made our description based on [20, 31, 35, 43, 47, 48, 49, 50] not ideal. In any case, at least for

the quantities considered here, we can conclude that thermal equilibrium is reached, perhaps because the Coulomb explosion of different cluster sizes is so chaotic to be practically not distinguishable from thermalization [45, 46].

In the experiments conducted at the ABC-ENEA laser facility in Rome-Italy, using two laser beams of total energy around 100 J, pulse duration 3 ns, we have produced colliding beams of about 100 keV collective kinetic energy E_C with a temperature spread $T<10$ keV. An anomalous increase of fusion reactions, as compared to a one-beam scenario, has been observed in p-^{11}B $\rightarrow 3\alpha$ (Q=8.6 MeV) and, for the first time, ^{6}Li+^{6}Li $\rightarrow 3\alpha$ (Q=20.8 MeV) nuclear reactions. The larger number of fusion reactions in the latter system, compared to the p+^{11}B $\rightarrow 3\alpha$ nuclear reaction case is due to different factors such as the higher Q-value of the ^{6}Li-^{6}Li reaction and the higher ^{6}Li concentration in the targets (i.e., higher reactions probability). An astrophysical S-factor=155(-111+266) GeVb has been estimated for the ^{6}Li-^{6}Li case at a Gamow energy $E_G \approx 476$ keV, higher than S=8.5 GeVb obtained in (conventional) beam-targets experiments at 1.05 MeV center of mass energy [7, 8]. This is an excitation energy region where ^{12}C displays many large widths resonances. Using suitable thin targets, we have observed cases where about 50% of the laser energy has been transformed into plasma ion kinetic energies and a low electromagnetic pulse and X-rays have been recorded when detectors were placed at a further distance from the target. This result opens up the possibility of a different route to energy production and to basic nuclear physics as fusion cross section measurement (e.g., ^{6}Li-^{6}Li) not known at such low energies.

Finally, we discussed some predictions if other clusters (i.e., d-t mixture) and target compositions are to be used (i.e. a plastic containing deuterium and tritium ions instead of hydrogen). This goes also in the direction to test if neutron-less fusion reactions are more convenient for producing energy than reactions producing

neutrons. If it is true that neutrons pose some problems in terms of activation, it is clear that hybrid reactors exploiting fusion-fission processes can give larger energy production efficiency [93, 94, 95]. Using our measured ion velocity distributions, we have obtained a very large fusion yield for d-t nuclear reaction, which can be compared to the results, opportunely scaled, obtained at the Omega facility using 40 kJ laser energy and at the National Ignition Facility (NIF) using about 1.6 MJ lasers energy. This also suggests a different path to energy production without attempts to compress and heat up the plasma: a non-equilibrium situation [46, 93, 96] where the plasma ion interacts at most once with other ions while crossing the target. A similar scenario has been reported in [79] for p-^{11}B nuclear reaction. In fact, the fusion cross section for p-^{11}B nuclear reaction increases exponentially with the plasma temperature or kinetic energies. This explains the dramatic increment respect to our result obtained for the same nuclear reaction (about two order of magnitudes larger). However, the measured plasma kinetic energies in [79] are very large and probably not needed to optimize the fusion reactions yield. We understand that increasing the average plasma ion kinetic energy decreases the number of ions available for a given laser energy. In our case we have a large number of ions and small kinetic energies, opposite to the ps-laser case in [79]. Thus an optimization of the average plasma kinetic energy (by changing the laser pulse duration) and an increase in its density, such as we propose here using one target, should maximize the fusion reactions yields of these systems. These could also be enhanced if the kinetic energy distribution of the system were localized in a region where resonances are present in the compound nucleus (i.e., higher fusion cross sections). A delicate balance between the available laser energy and the kinetic energy of the produced ions might be reached by a suitable choice of the target geometry (thickness, composition and so on), laser focalization, impulse duration etc. It is important that most of the laser

energy is transferred to the highest possible number of ions within an optimized kinetic energy distribution. If the efficiency of energy transferred from the lasers to the ions is large, we get a low electromagnetic pulse and X-ray, which are not only waste for our purposes, but also a great disturbance to the experimental devices.

REFERENCES

[1] J. D. Walecka (1932), *Theoretical Nuclear and Subnuclear Physics*, Oxford University Press, (New York, 1995).

[2] R. A. Dunlap (2003), *An introduction to the physics of nuclei and particles*, Brooks/Cole Publishing Company (Belmont, 2004).

[3] C. Angulo *et al.*, Nucl. Phys. A. **656**, 3 (1999).

[4] J. Yan *et al.*, Phys. Rev. C **55**, 1890 (1997).

[5] J. M. Davidson *et al.*, Nucl. Phys. A **315** (1979) 253.

[6] H. W. Becker, C. Rolfs and H. P. Trautvetter, Z. Phys. **327**, 341-355 (1987).

[7] M. N. Huberman, M. Kamegai, and G. C. Morrison, Phys. Rev. **129**, 791 (1963).

[8] M. Kamegai, Phys. Rev. **131**, 1701 (1963).

[9] http://t2.lanl.gov/nis/data/astro.

[10] A. Bonasera and V. N. Kondratyev, Phys. Lett. B**339**, 207 (1994).

[11] S. Kimura and A. Bonasera, Phys. Rev. C **76**, 031602 (2007).

[12] S. Kimura and A. Bonasera, Phys. Rev. C **87**, 058801 (2013).

[13] G. Gamow, Z. Phys. **51**, 204-212 (1928).

[14] A. Einstein, Ann. Phys. **18**, 639641 (1905).

[15] M. Kikuchi, K. lackner and M. Q. Tran, *Fusion Physics*, International Atomic Energy Agency, (Vienna, 2012).

[16] ITER: http://www.iter.org

[17] Nation Ignition Facility: https://lasers.llnl.gov/science/energy-for-the-future

[18] Laser MegaJoule: http://www-lmj.cea.fr/index.htm

[19] T. Ditmire *et al.*, Nature (London) 398 (1999) 489.

[20] W. Bang, M. Barbui, A. Bonasera, G. Dyer, H. J. Quevedo, K. Hagel, K. Schmidt, F. Consoli, R. De Angelis, P. Andreoli, E. Gaul, A. C. Bernstein, M. Donovan, M. Barbarino, S. Kimura, M. Mazzocco, J. Sura, J. B. Natowitz, and T. Ditmire, Phys. Rev. Lett. **111**, 055002 (2013).

[21] M. Barbui, W. Bang, A. Bonasera, K. Hagel, K. Schmidt, J. B. Natowitz, R. Burch, G. Giuliani, M. Barbarino, H. Zheng, G. Dyer, H. J. Quevedo, E. Gaul, A. C. Bernstein, M. Donovan, S. Kimura, M. Mazzocco, F. Consoli, R. De Angelis, P. Andreoli and T. Ditmire, Phys. Rev. Lett. **111**, 082502 (2013).

[22] M. Barbarino *et al.*, arXiv:1510.05971.

[23] D. Lattuada *et al.*, in preparation.

[24] S. Kimura and A. Bonasera, Phys. Rev. Lett. **93**, 262502 (2004).

[25] A. Bonasera *et al.* (LAPLAFUS Collaboration), *Proceedings of the 4th International Conference on Fission Properties of Neutron Rich Nuclei, Sanibel Island, 2007*, edited by J. H. Hamilton and A. V. Ramayya (World Scientific, Singapore, 2008), p. 503.

[26] K. W. Madison *et al.*, Phys. Rev. A **70**, 053201 (2004).

[27] H. Li *et al.*, Phys. Rev. A **74**, 023201 (2006).

[28] I. Last and J. Jortner, Phys. Rev. Lett. **87**, 033401 (2001).

[29] F. Peano, R. A. Fonseca, and L. O. Silva, Phys. Rev. Lett. **94**, 033401 (2005).

[30] W. Bang, M. Barbui, A. Bonasera, H. J. Quevedo, G. Dyer, A. C. Bernstein, K. Hagel, K. Schmidt, E. Gaul, M. E. Donovan, F. Consoli, R. De Angelis, P. Andreoli, M. Barbarino, S. Kimura, M. Mazzocco, J. B. Natowitz, and T. Ditmire, Phys. Rev. E **88**, 033108 (2013).

[31] K. W. Madison *et al.*, Phys. Plasmas **11**, 270 (2004).

[32] T. Fennel *et al.*, Rev. Mod. Phys. **82**,1793 (2010).

[33] Y. Kishimoto, T. Masaki, and T. Tajima, Phys. Plasmas **9**, 589 (2002).

[34] V. P. Krainov and M. B. Smirnov, Phys. Rep. **370**, 237 (2002).

[35] J. Zweiback *et al.*, Phys. Rev. Lett. **84**, 2634 (2000)

[36] J. Zweiback *et al.*, Phys. Plasmas **9**, 3108 (2002).

[37] H. S. Bosch and G. M. Hale, Nucl. Fusion **32**, 611 (1992).

[38] E. W. Gaul *et al.*, Appl. Opt. **49**, 1676 (2010).

[39] W. Bang *et al.*, Phys. Rev. E **90**, 063109 (2014).

[40] W. Bang *et al.*, Rev. Sci. Instrum. **83**, 063504 (2012).

[41] M. J. Mead *et al.*, Review of Scientific Instruments **75** (2004) 4225.

[42] C. G. Brown Jr. *et al.*, Journal of Physics: Conference Series **244** (2010) 032001.

[43] W. Bang *et al.*, Phys. Rev. E **87**, 023106 (2013).

[44] T. C. Awes *et al.*, Phys. Rev. C **24**, 89 (1981).

[45] E. Ott, *Chaos in Dynamical Systems*, Cambridge University Press (1993).

[46] A. Bonasera, Fusion 2003, Progr. Theor. Phys. **154**, 261 (2004).

[47] K. J. Mendham *et al.*, Phys. Rev. A **64**, 055201 (2001).

[48] F. Dorchies *et al.*, Phys. Rev. A **68**, 023201 (2003).

[49] M. Lewerenz, B. Schilling, and J. P. Toennies, Chem. Phys. Rev. Lett. **206**, 381 (1993).

[50] B. J. C. Wu *et al.* J. Chem. Soc. **69**,1776 (1998).

[51] D. G. Jang *et al.*, Applied Phys. Rev. Lett. **105**, 021906 (2014).

[52] W. Bang, Phys. Rev. E **92**, 013102 (2015).

[53] Inertial Fusion Progress Report (19921993), RT/ERG/FUS/93/67, ISSN/1120-5598, ENEA, 1994.

[54] C. Strangio and A. Caruso, Laser and Particle Beams, 16 (1998) 45.

[55] F. Consoli, R. De Angelis, P. Andreoli, G. Cristofari, G. Di Giorgio, A. Bonasera, M. Barbui, M. Mazzocco, W. Bang, G. Dyer, H. Quevedo, K. Hagel, K. Schmidt, E. Gaul, T. Borger, A. Bernstein, M. Martinez, M. Donovan, M. Barbarino, S. Kimura, J. Sura, J. B. Natowitz, and T. Ditmire, Nuclear Instruments and Methods in Physics Research A **720** (2013) 149152.

[56] E. Woryna, P. Parys, J. Wolowski, and M. Mroz, Laser and Particle Beams **14** (1996) 293.

[57] M. Farnikova *et al.*, Proceedings of the SPIE: The International Society for Optical Engineering **2767** (1996) 113.

[58] L. Torrisi *et al.*, Journal of Applied Physics **105** (2009) 123304.

[59] L. Torrisi *et al.*, Journal of Applied Physics **103** (2008) 083106.

[60] C. G. Freeman *et al.*, Review of Scientific Intstruments **82**, 073301 (2011).

[61] E. L. Clark *et al.*, Phys. Rev. Lett. **85**, 1654 (2000).

[62] M. Hegelich *et al.*, Phys. Rev. Lett. **89**, 085002 (2002).

[63] M. Mori *et al.*, Plasma Fusion Res. **1**, 042 (2006).

[64] W. Mroz *et al.*, Rev. Sci. Instrum. **67**, 1272 (1996).

[65] A.Bonasera and C.Strangio, *Realizzazione di spettrometri di ioni (parabola di Thomson) per la determinazione della funzione di distribuzione della velocita degli ioni di varie specie presenti in plasma prodotti mediante laser*, ENEA-Kore university contract, 2005.

[66] J. A. Frenje *et al.*, Phys. Plasmas **17**, 056311 (2010).

[67] M. Giorgini, Nuclear Physics B: Proceedings Supplements **197** (2009) 66.

[68] C.G. Freeman *et al.*, Rev. Sci. Instrum. **82** (2011) 073301.

[69] K. F. Chan *et al.*, Nucl. Instr. B **263**, 290 (2007).

[70] A. P. Fews and D. L. Henshaw, Nuclear Instruments and Methods in Physics Research **197**, 517 (1982).

[71] A. P Fews and D. L. Henshaw, Nuclear Instruments and Methods in Physics Research **223**, 609 (1984).

[72] J. A. Frenje *et al.*, Rev. Sci. Instrum. **79**, 10E502 (2008).

[73] F. H. Seguin *et al.*, Rev. Sci. Instrum. **77**, 975 (2003).

[74] D. Nikezic and K.N. Yu, Comput. Phys. Comm. **174**, 160-165, 2006.

[75] D. Nikezic and K.N. Yu., Radiat. Meas. **37**, 595-601, 2003.

[76] D. Nikezic and K.N. Yu., Comput. Phys. Comm. **178**, 591-595, 2008.

[77] V. S. Belyaev *et al.*, Phys. Rev. E **72**, 026406 (2005).

[78] S. Kimura *et al.*, Phys. Rev. E **79**, 038401 (2009).

[79] C. Labaune *et al.*, Nat. Commun. 4:2506doi: 10.1038/ncomms3506 (2013).

[80] D. S. Clark, S. W. Haan, and J. D. Salmonson, Physics of Plasmas **15**, 056305 (2008).

[81] H. S. Park *et al.*, Phys. Rev. Lett. **112**, 055001 (2014).

[82] O. A. Hurricane *et al.*, Nature 506, 343348 (2014).

[83] S. H. Glenzer *et al.*, Phys. Plasmas **19**, 056318 (2012).

[84] S. H. Glenzer *et al.*, Plasma Phys. Control. Fusion **54**, 045013 (2012).

[85] S. W. Haan *et al.*, Phys. Plasmas **18**, 051001 (2011).

[86] J. M. Soures *et al.*, Phys. Plasmas **3**, 2108 (1996).

[87] J. R. Rygg *et al.*, Phys. Plasmas **13**, 052702 (2006).

[88] T. C. Sangster *et al.*, Phys. Plasmas **17**, 056312 (2010).

[89] R. McCrory *et al.*, Nucl. Fusion **41**, 1413 (2001).

[90] R. Betti *et al.*, Phys. Plasmas **17** (5), 058102 (2010).

[91] O. F. Hagena and W. Obert, J. Chem. Phys. **56**, 1793 (1972).

[92] O. F. Hagena, Rev. Sci. Instrum. **63**, 2374 (1992).

[93] A. Bonasera, *Produzione di energia controllata (Laser driven energy production)*, INFN patent pending, patent application N. TO2014A000408.

[94] H. Bethe, Phys. Today **32**, 44 (1979).

[95] E. Gerstner, Nature 460 (2009) 25.

[96] N. Rostoker, M. W. Binderbauer, and H. J. Monkhorst, Science 278, 14191422 (1997).

[97] T. Yamauchi, Radiation Measurements 36 (2003) 7381.

[98] S. A. Durrani and R. K. Bull, *Solid State Nuclear Track Detection, Principles, Methods and Applications*, Pergamum Press, Oxford (1987).

[99] R. L. Fleischer, P. B. Price and R. M. Walker, *Nuclear Tracks in Solids, and Application*, University of California Press, Berkley, England (1975).

[100] G. Somogyi and A. S. Szalay, Nuclear Instruments and Methods **109**, pp. 211-232, (1973).

[101] D. Nikezic and K. N. Yu, Computer Physics Communications, 174, pp. 160-165, (2006).

APPENDIX A

AVERAGE CROSS SECTION

A detailed calculation of Eq.(1.7) follows. Let the average cross section $\langle \sigma \rangle$ in velocity space to be given by

$$
\begin{aligned}
\langle \sigma \rangle &= 4\pi (\frac{m}{2\pi T})^{3/2} \int_0^\infty \sigma(v) v^2 e^{-\frac{mv^2}{2T}} \, dv \\
&= \sqrt{\frac{8m}{\pi T^3}} \int_0^\infty S(E) e^{-(\sqrt{\frac{2b}{mv^2}} + \frac{mv^2}{2T})} \, dv,
\end{aligned}
\tag{A.1}
$$

and with S constant

$$
\langle \sigma \rangle = \sqrt{\frac{8m}{\pi T^3}} S \int_0^\infty e^{-(\sqrt{\frac{2b}{mv^2}} + \frac{mv^2}{2T})} \, dv.
\tag{A.2}
$$

In order to evaluate the integral, we proceed with the steepest descent method. Let us expand the argument of the exponential

$$
g(v) = \sqrt{\frac{2b}{mv^2}} + \frac{mv^2}{2T},
\tag{A.3}
$$

in a Taylor series about v_0 *i.e.* as

$$
g(v) = g(v_0) + g'(v_0)(v - v_0) + \frac{g''(v_0)}{2!}(v - v_0)^2 + O(v^3).
\tag{A.4}
$$

The minimum of this function occurs at

$$
v_0 = (\frac{2bT^2}{m^3})^{\frac{1}{6}}.
\tag{A.5}
$$

100

Then

$$g(v_0) = \frac{3}{2}\left(\frac{2b}{T}\right)^{\frac{1}{3}} = \frac{3}{2}\frac{mv_0^2}{T}, \tag{A.6}$$

$$g'(v_0) = 0, \tag{A.7}$$

and

$$g''(v_0) = \frac{3m}{T}. \tag{A.8}$$

Therefore

$$
\begin{aligned}
\langle\sigma\rangle &= \sqrt{\frac{8m}{\pi T^3}}S\int_0^\infty e^{-\left(\sqrt{\frac{2b}{mv^2}} + \frac{mv^2}{2T}\right)}dv \\
&= \sqrt{\frac{8m}{\pi T^3}}Se^{-g(v_0)}\int_0^\infty e^{-\frac{f''(v_0)}{2!}(v-v_0)^2}dv \\
&= \sqrt{\frac{8m}{\pi T^3}}Se^{-\frac{3}{2}\frac{mv_0^2}{T}}\int_0^\infty e^{-\frac{3m}{2T}(v-v_0)^2}dv. \tag{A.9}
\end{aligned}
$$

Now, let

$$\nu = \sqrt{\frac{2T}{3m}}. \tag{A.10}$$

The average cross section becomes

$$\langle\sigma\rangle = \sqrt{\frac{8m}{\pi T^3}}Se^{-\frac{3}{2}\frac{mv_0^2}{T}}\int_0^\infty e^{-\left(\frac{v-v_0}{\nu}\right)^2}dv. \tag{A.11}$$

For T small, one can show that $v_0 \gg \nu$, and therefore we can perform analytical integration over the entire energy as

$$
\begin{aligned}
\langle\sigma\rangle &= \sqrt{\frac{8m}{\pi T^3}}Se^{-\frac{3}{2}\frac{mv_0^2}{T}}\int_{-\infty}^\infty e^{-\left(\frac{v-v_0}{\nu}\right)^2}dv \\
&= \sqrt{\frac{8m}{\pi T^3}}Se^{-\frac{3}{2}\frac{mv_0^2}{T}}\sqrt{\frac{2\pi T}{3m}}. \tag{A.12}
\end{aligned}
$$

Let E_G be the most effective energy (i.e., Gamow energy peak) as

$$E_G = \frac{1}{2}mv_0^2 = (\frac{T\sqrt{b}}{2})^{\frac{2}{3}},$$

(A.13)

then

$$\langle \sigma \rangle = \frac{4}{\sqrt{3}}\frac{S}{T}e^{-\frac{3E_G}{T}}.$$

(A.14)

APPENDIX B

CR-39

Latent tracks in CR-39 nuclear track detector result from the slowing down of heavy charged particles (i.e., ion and the secondary electrons ejected around the trajectory) which breaks the polymer bonds, leaving free radicals that either react with dissolved oxygen in CR-39 to form a permanent latent track or recombine, failing to form a latent track, depending on the concentration of oxygen near the ions path [97]. To discuss the property of the latent tracks in terms of the dose distribution, CR-39 plastics can be etched by a suitable etchant to enlarge the tracks sufficiently so that they become visible under an optical microscope. After chemical etching, two different diameters are observed depending on the angle of the incident particles. In particular, circular tracks will appear for perpendicularly incident particles while more elliptical tracks will be generated from oblique incidence [98]. Track core size depends on the incidence angles and alpha particle energies.

The traditional method for determining the bulk etch rate V_B is based on [98]

$$V_B = \frac{1}{2}\frac{1}{\rho A}\frac{\Delta m}{\Delta t}.$$ (B.1)

In the above, Δm is the mass defect, Δt is the etching time interval, A is the detector surface area and, ρ, is the density of the detector material. The track etch rate, V_T, is given as [99]

$$V_T(t) = V_B \frac{4e_T^2 + V_D^2(t)}{4e_T^2 - V_D^2(t)},$$ (B.2)

where $V_D(t){=}D'(t)$ is the diameter growth rate of the mean track diameter, $D(t)$, and e_T is the thickness of the removed surface layer. The track diameter increases

with the increasing etching time for incident alpha energy from 1 to 5 MeV. The maximum track diameter is achieved for the etching time corresponding to the end of the particle's range at each energy ion (obtainable via SRIM code simulation). The variation of the track diameters as a function of the alpha particle energies at selected values of the etching time shows a noticeable energy and time dependence of track diameters for alpha particles. It has been also noticed that the track diameters increase as the etching time increases [99]. However, the tracks diameters for large incident angles between 80° and 90° depend only on the energy, hence the diameter of the circular track is a good measure of the incident energy. Then, the circular shape exhibited by the majority of the observed tracks facilitated the analysis of the relation between the geometric parameters and the characteristics of the incident charged particles during the whole etching process. The electronic energy loss and the track diameter present the same evolutions versus the incident particle energy, in fact the maximum in track diameter is observed when the total energy is deposited by the charged particle in the detector and the damaged region is fully etched [98].

The track etch rate V_T reflects the radial dose distribution and it is used to evaluate the track core size and also examine the damage distribution around the ion trajectory. Previous studies show that UV spectral measurements combined to the model of track overlapping can be used to determine the track core radius r_t as [97]

$$r_t = 0.150(\frac{dE}{dx})^{0.39} \quad \text{in nm.} \tag{B.3}$$

In the above, dE/dx is the stopping power in the unit of keV/μm.

During measurements, the digital camera installed directly to an optical microscope scans the studied surface many times, typically with a 256×256 resolution for a scanning area of 25×25 μm^2. Three-dimensional track geometry is based on

the Track-Test code developed for calculating the formation of alpha tracks in three dimensions [100, 101]. The typical distance between neighboring paths is about 0.1 μm. The track diameter for a short etching time used is less than 1 μm. For example, the diameter of the alpha-particle track with 5 MeV incident energy in the CR-39 detector etched for 15 min is about 0.3 μm. In general, the probability to find tracks in a smaller scanned area is smaller. After etching procedure, the method of discrimination and counting used by ENEA-Bologna for the tracks on the etched CR-39 detectors is based on software generation of simulated images of the tracks produced by particles hitting the detector with a given energy and under a given angular range. As well on the procedure of pattern recognition performed on the CR-39 experimental images acquired by a proper microscope with respect to the simulated tracks. This method has been applied to the CR-39 so that only tracks produced by alpha particles have been produced by the simulations. During the experiments, track detectors CR-39 covered by aluminum foil were used for detecting the alpha particles produced in the nuclear reactions

$$p +^{11} B \rightarrow 3\alpha + 8.6 \quad \text{MeV}$$
$$^{6}Li +^{6} Li \rightarrow 3\alpha + 20.8 \quad \text{MeV}$$

Detectors were placed in a vacuum chamber at various angles to the normal of the target (between 43° and 95°) to estimate their angular distribution, and at various distances from the target (from 1.28 to 2.4 cm). The calibration of detectors CR-39 has been made using standard alpha sources (E_α= 0.4-7.7 MeV) and cyclotron alpha sources (E_α= 8-30 MeV). Four energy ranges have been considered for the alpha particles produced in the ^{6}Li-^{6}Li nuclear reaction (E_α=0.5 MeV, E_α=2.5 MeV, 3.5< E_α <4.5 MeV, E_α >10 MeV). A summary of the alpha particle density measured on

shot #1410 is given in Figure 8.1. The method for discrimination of alpha radiation was performed by the ENEA-Bologna group under the usual working conditions. An increase of the CR-39 etching rate has been experimentally determined with respect to usual conditions for the ENEA-Bologna group and it has been considered in the pattern recognition procedure.
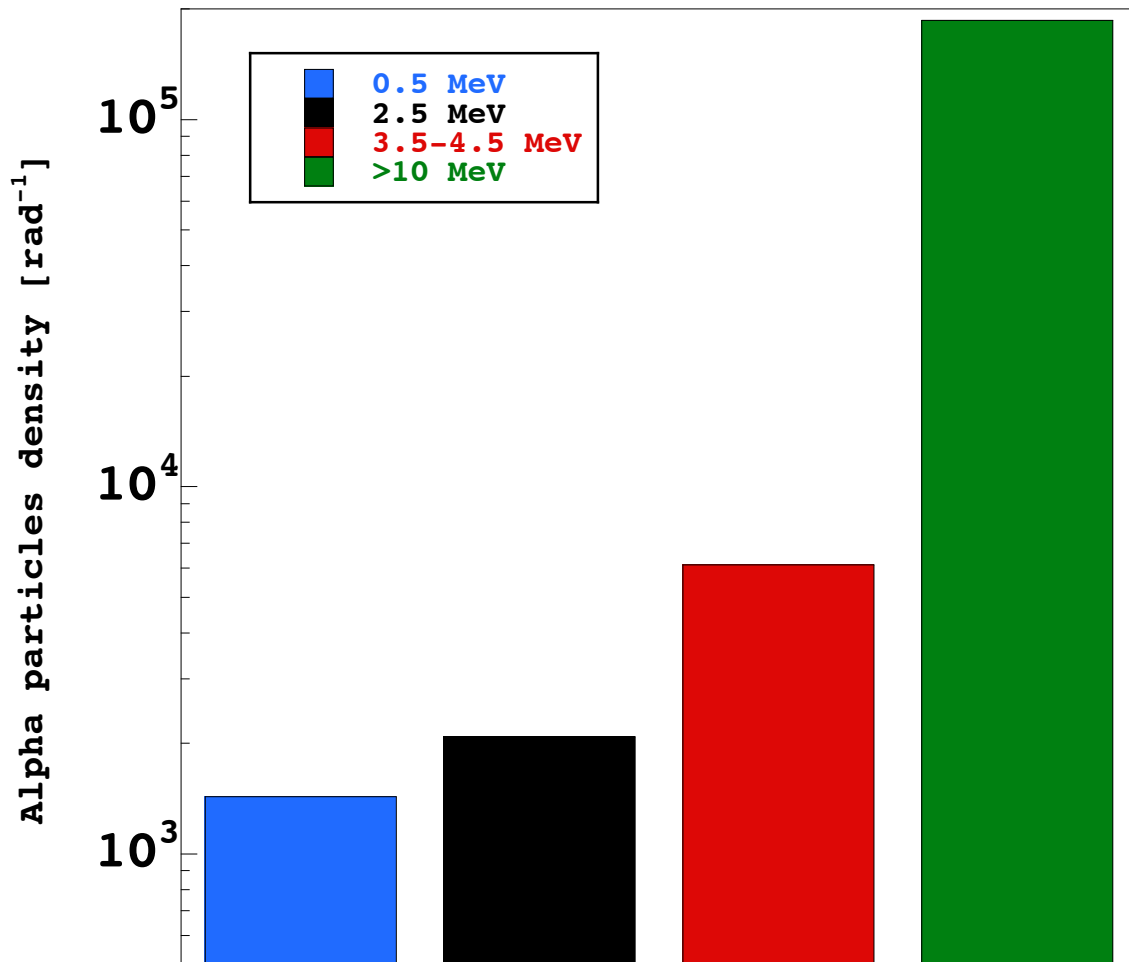

Figure B.1: Alpha particles density measured per solid angle on shot #1410 from ^{6}Li-^{6}Li nuclear reactions.